POLITECNICO DI MILANO
DIPARTIMENTO DI FISICA
DOCTORAL PROGRAMME IN PHYSICS

PHOTOPHYSICS OF 3D LEAD HALIDE PEROVSKITE SEMICONDUCTORS: LIGHT ABSORPTION AND LUMINESCENCE

Doctoral Dissertation of:
Valerio D'Innocenzo

Supervisor:
Dr. Annamaria Petrozza

Tutor:
Prof. Guglielmo Lanzani

The Chair of the Doctoral Program:
Prof. Paola Taroni

2015 - XXVIII Cycle

Photophysics of 3D lead halide perovskite semiconductors: Light absorption and Luminescence

Valerio D'Innocenzo

Supervisor: Dr. Annamaria Petrozza

THIS thesis deals with the optical characterization of various 3D lead-halide perovskites, via experimental investigation and modeling, with the aim to describe the photophysics underlying the photon absorption and emission in these materials. It describes the work performed predominantly by Valerio D'Innocenzo in the period 2013-2015 for attainment of his Ph.D. The experiments were carried out at the Center for Nano Science & Technology in Milan, under the supervision of Dr. Annamaria Petrozza.

Chapter 1 provides a brief introduction to the contextual background with particular attention given to the state of the art of lead-halide perovskites research. Moreover it furnishes a brief review of the fundamental semiconductor optoelectronic properties, highlighting the theoretical model that will be employed in the subsequent chapters.

Chapter 2 describes the sample fabrication procedures and all the experimental tools and techniques used in order to carry out the research presented in this thesis.

Chapter 3 includes an extensive analysis of the linear absorption spectra of lead-halide perovskites using established theoretical models. Based on these experimental results we give an estimation for the exciton binding energy in these systems. Moreover, studying the thermodynamic equilibrium that is established between the bound and ionized photo-excited states, we conclude that within a photovoltaic operation regime the excitonic contribution to the charge carrier formation is negligible. Eventually, we report the experimental evidence testifying the link between the morphological properties of the material and the exciton binding energy value.

Chapter 4 describes the photoluminescence properties of $CH_3NH_3PbI_3$ perovskite. We show that, despite the marked excitonic feature characterizing the absorption spectrum, the emission is governed by a trap-limited electron-hole bimolecular radiative recombination. Moreover we report the possibility of tuning the the spectral emission and radiative rate via tuning of the lead-halide bonding angle within the crystalline lattice.

Chapter 5 contains the results of time-resolved photoluminescence and excitation cross-correlation experiments performed on both $CH_3NH_3PbBr_3$ and $CsPbBr_3$. According to the experimental results we claim that, despite the high exciton binding energy, as estimated from the absorption spectra, the exciton is not stabilized in neither the case, resulting again in a trap-limited electron-hole plasma luminescence. Eventually we investigate with the same techniques a $CsPbBr_3$ colloidal nano-crystals solution. In this case, thanks to both the reduced trap-induced morphological disorder and a quantum confinement effect, we observe that the excitonic state is stabilized and acts as the dominant emitting specie.

For a successful technology, reality must take precedence over public relations, for nature cannot be fooled.

– **Richard P. Feynman**, (on the Space Shuttle Challenger Accident)

In memory of L.V.L.

Contents

List of Figures

List of Tables

Preface

''"The Stone Age did not end for lack of stone, and the Oil Age will end long before the world runs out of oil".[1] This statement, pronounced in 1973 by the then Saudi Arabia ministry of oil Sheikh Zaki Yamani, was placed in the historic context of the first oil crisis which, for the first time, drew the attention to the research of possible alternatives to the main global energy resource. Weather this prophecy will revel itself true or not, there is no denying the fact that the search for innovative solutions in the field of energy is a fundamental issue which the scientific community has been addressing for several decades.

Lead-halie perovskites constitute a class of materials that today set itself as a viable option in order to address the global energy issue. Presented for the first time in a publication dating back to 1978 only more recently they were embedded as active materials in photovoltaic devices. As these early applications stemmed from the *dye sensitized solar cells (DSSC)* community, the description of lead-halide perovskite photophysics was often reminiscent of the organic dyes experience characterizing the DSSC research activity since 1990s. The lack of a clear understanding of the photophysical processes governing the photon to electron conversion in these materials may severely hamper the full realization of their potential as a new photovoltaic technology.

In this thesis we present a thorough spectroscopic investigation of both hybrid and fully inorganic lead-iodide and lead-bromide perovskite. Via the analysis of the absorption and luminescence properties we give a major insight into the physics of light-matter interaction, thus enabling the reader to place back the lead-halide perovskite into the more appropriate stream of research of the bulk crystalline semiconductors.

CHAPTER *1*

Introduction

1.1 Material perspective

In 1839 Gustave Rose, a German mineralogist, discovered and reported the mineral structure of calcium titanium oxide ($CaTiO_3$). This mineral was later on characterized by the Russian mineralogist Lev A. Perovski who was the first to report its crystalline structure which, therefore, derived the name of *Perovskite*.

This family of material adopt the chemical formula ABX_3 where A and B stand for cation of different size and/or nature, while X are anions. Starting from their first appearance the most broadly studied among perovskites are the metal-oxide ones (i.e. X = O) mainly thanks to their interesting ferroelectric and magnetic properties, and to the possible application as superconductive materials.[2] The interest in hybrid meatal-halide perovskite date back to 1884 when the first hybrid metal-halide perovskite structure, based on gold and chloride, was published.[3] In 1958 Møller reported the first lead-halide based perovskite with a paper investigating the photoconductive properties of $CsPbX_3$ perovskite,[4] while the first hybrid organic-inorganic lead-halide perovskite structure was published in 1978 by Weber and Naturforsch.[5]

It was not until the end of the 20th century that the perovskite were employed in electronic devices as semiconductors. Kagan and Mitzi contributed with pioneering works demonstrating the possibility to employ layered organic-inorganic halide perovskites as the active phase in thin film transistors (TFTs) and light emitting diodes (LEDs).[6–8]

Early photovoltaic (PV) application of hybrid perovskites date back to 2006 when Miyasaka and coworkers employed methylammonium lead bromide ($A = CH_3NH_3$, $B = Pb$ $X = Br$) as sensitizer on nanoporous TiO_2 scaffold within a liquid electrolyte based dye-sensitized solar cell (DSSC) architecture, achieving a

power conversion efficiency (PCE) of 2.2%.[9] From this starting point in few years the perovskite based solar cells (PSC) followed a stunning device improvement going hand in hand with an increasing conversion efficiency. In 2009 the aforementioned research group obtained a PCE of 3.8% replacing the Br with the I,[10] while in 2011 Park and co-workers used a combination of conventional dyes and perovskite nanoparticle improving the device efficiency to 6.5%.[11] Further works focused on the improvement of the device stability through the substitution of the liquid electrolyte with a solid state hole transporting material (HTM).[12] A turning point was represented by the works of Etgar et al.[13] and Lee et al.,[14] in which they reported the possibility either of removing the HTM material or to substitute the n-type mesoporous TiO_2 electron transporting layer with an inert Al_2O_3 scaffold obtaining a 9.7% and 10.9% PEC devices respectively. These reports drew the attention of the scientific community on the working mechanism of the PSCs, i.e. on the role of the electron and hole extractin layer, encouraging the investigation of planar architecture.[15–17] Notably in the work by Lee et al. was also reported for the first time a mixed halide perovskite, thus paving the way to the material composition tuning enabling tuning of the optical band-gap, eventually leading to a record PCE exceeding 20%.[18]

The multitude of optoelectronic properties ideal for PV applications, such as the high charge carrier mobility and the large spectraly tunable absorption coefficient, together with the low cost solution-process based deposition and the strong defect tolerance make hybrid lead-halide perovskite successful candidate for a new affordable PV technology and a promising material for for applications beyond photovolatics.

1.1.1 Crystalline structure and phase

In this section we briefly present the structural properties of the hybrid lead-halide perovskite crystal. Without the aim of reporting a thorough description of the crystalline structure, we will discuss only the concepts which are necessary for the comprehension of the subsequent discussion.

In the case of hybrid perovskite the A site is occupied by an *organic* cation. The most widely used in PV field is the methylammonium ion $CH_3NH_3^+$ which will be indicated in the following as MA, however most recently also formamidinium $(CH(NH_2)_2^+$, FA) has been successfully employed. Moreover a mix of this two cations was proposed in different ratio in order to tune the bandgap granting an increased absorption of the low energy region of the solar spectrum.[19–21] Cs is by far the most commonly employed inorganic cation. The smaller size of Cs with respect to MA ans FA, together with the absence of an intrinsic dipole moment, make this cation very interesting for the investigation of the influence of the A cation on the overall material optoelectronic properties.[18] Very recent trends are also exploring the possibility of mixing Cs and FA.

The B is a metal cation from the IVA group in a divalent oxidation (Pb^{2+}, Sn^{2+}, Ge^{2+}). In this thesis we will consider only the case of lead-based hybrid perovskite. This choice is dictated by the fact that lead has proven to be superior with respect to tin and germanium both in terms of performance and stability. It's anyway worth noticing that a entire field of research is devoting much effort

in order to replace lead with tin in virtue of its reduced toxicity, as testified by some preliminary results from Noel et al.[22] and Hao et al.[23]

The X site is occupied by an halide anion which has shown to be the most effective component in terms of material's properties tuning. The effect of the halide anion substitution and mixing will be briefly discussed in the following.
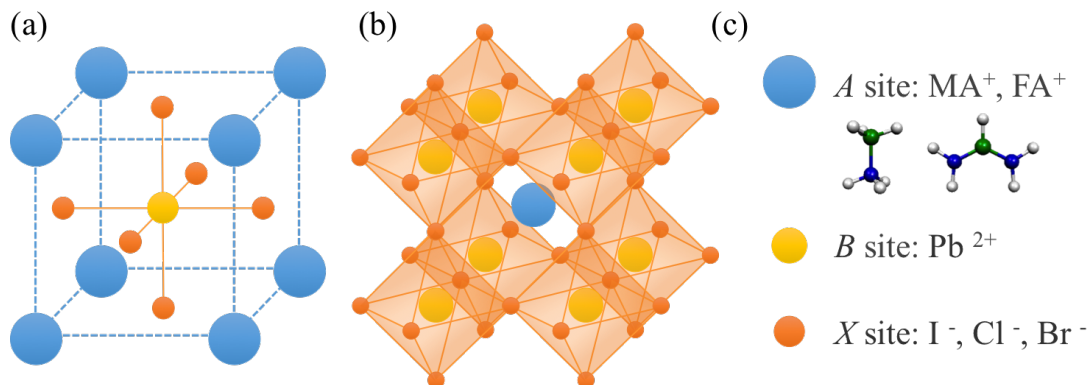
Figure 1.1: *The perovskite unit cell. (a) A cations (blue) occupy the lattice corners, B cations (yellow) occupy the interstitial site, and X anions (orange) occupy lattice faces. (b) An alternative view of the structure comprehending more than one unit cell depicting B cations assembled around X anions to form BX_6 octahedra. (c) Possible occupants of A, B and X sites.*

Similarly to their inorganic parent, hybrid perovskite components obey some allowable tolerance factors in order to achieve the desired crystalline structure. The most striking consequence is that the dimensionality of the perovskite crystalline system can be tuned simply changing the organic-inorganic molar ratios. In the case of lead one can go from *dot structures* (0D) in the case of $(CH_3NH_3)_4PbX_6 2H_2O$, to *perovskite wires* (1D) for $CH_{10}NH_2PbX_3$, *layered perovskite* (2D) $C_nH_{2n+1}NH_3PbX_4$ and *bulk crystals* (3D) of $CH_3NH_3PbI_3$.[18]

The ideal symmetry of the 3D crystalline structure is a face centered cubic cell in which the organic cation A occupy the lattice corners, the B cations (lead in our case) occupy the center of the cell, while the halide X are arranged on the lattice faces coordinating in a BX_6 octahedra (figure 1.1.(a)). Notice that both the symmetry and the electronic structure of the system is entirely defined by the $B - X$ bond, however the steric hindrance from A cation can cause a distortion of the inorganic cage, thus affecting the symmetry and the optoelectronic properties of the perovskite. This case will be discussed in more detail in section 4.3. In the ideal case (no distortion considered) the cubic perovskite structure belong to the Pm3m space group with a 12-fold coordination of the A cation and a 6-fold coordination of the B cation. Deviations from the ideal symmetry can be due from several factors, among which the most relevant is the relative radii size of the A, B and X elements. The tolerance t[24] and octahedral factor μ[25] together represent a guideline for determining halide perovksite formability and, despite not being entirely sufficient to predict all the possible , they can furnish a good first approximation in the prediction of the crystalline symmetry, as shown in figure 1.2.

$$t = \frac{(R_A + R_X)}{\sqrt{2}(R_B + R_X)} \qquad \mu = \frac{R_B}{R_X} \qquad (1.1)$$

The octahedral factor provides a direct information on the stability of the BX_6 octahedron, which define the possibility of a perovskite structure formation. In particular in the case of halide perovskite formation occurs when the B and X atoms are chosen in order to have $\mu > 0.442$, over this value the octahedron will be unstable preventing the perovskite formation. The tolerance factor describes the possible deviation from the ideal cubic symmetry as a fanction of the relative radii size. In general for halide perovskite one has that $0.85 < t < 1.11$ corresponds to the cubic structure formation, however a more detailed prediction can be made following some simple observations:

(a) for $t < 1$ a tilting of the octahedra, and consequent symmetry reduction, is expected due to a compression of the B-X bond;

(b) for $t > 1$ one can observe an higher stability of the hexagonal structure usually due to a large A cation radius;

eventually in the case of an excessively large cation A one will have $t \gg 1$ and the consequent formation of a reduced dimensionality perovskite system.
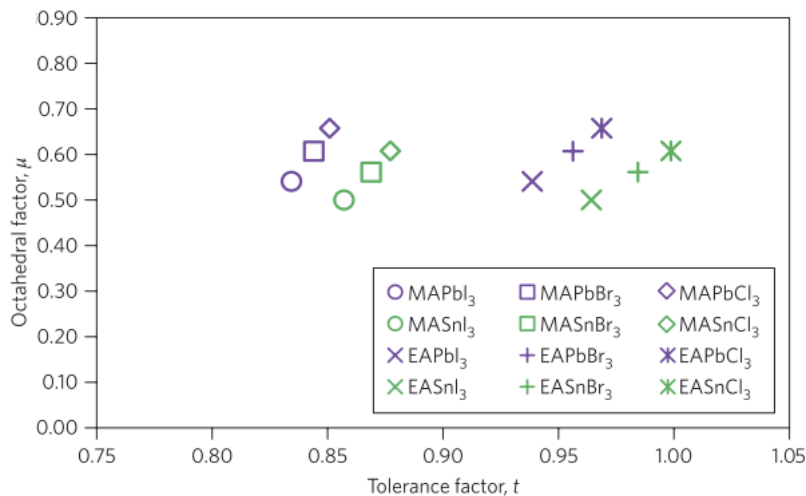
Figure 1.2: *Calculated t and μ factors for 12 halide perovskites based on either methylammonium (MA) and ethylammoniu (EA). The corresponding formamidinium (FA) based halides are expected to have intermediate values between those of the compounds shown. Figure adapted from reference,[26] with permission.*

As already mentioned, in general perovskite crystals reveal a cubic symmetry (Pm3m) at room temperature. However depending on the constituent they can assume either a tetragonal (I4/mcm) or an orthoromobic (Pnam) phase. Moreover upon temperature cooling these crystals can undergo phase transitions from cubic to tetragonal to orthorombic. For example, considering the two perovksite crystals considered in this thesis, while the $MAPbI_3$ pervoskite undergoes a

cubic to tetragonal phase transition at 327 K and a tetragonal to orthorombing at 167 K,[27,28] $MAPbBr_3$ forms in cubic phase at room temperature[18] and no phase transition occurs in the explored temperature range (77 K - 400 K). As the symmetry of the crystalline structure defines the electronic band structure the aforementioned phase transitions can directly affect the absorption and emission properties of the material. We will discuss in more detail this possibility in section 3.2.

1.1.2 Role of the halide substitution

As already mentioned the halide anion has shown to be the most effective component to tune the optical and electronic properties of this material. While in the following chapters we will broadly discuss how the exchange from I to Br halide deeply affects the absorption and emission properties of the perovskite, in this section we report a brief summary of the state of the art concerning the electro-optical devices based either on iodine or bromide base perovkside.

Iodide (I). Moving down in the VIIA group of the periodic table the halogen ionic radius increases and, once incorporated in a perovskite structure, this will affect the electronic structure inducing a red-shift of the absorption onset, i.e. a reduction of the semiconductor band-gap.[18] This is probably the main reason behind the unrivaled superiority of the iodine based hybrid lead-halide perovskite with respect to the Cl and Br based counterparts in PV application. Moreover it's worth noticing that the very little mismatch of the between Pb an I ionic radius guarantees the formation of a crystalline structure with little lattice strain, thus demonstrating a good chemical stability. Nevertheless lead-iodide perovskite turned out to be highly moisture sensitive, thus heavily affecting the long term stability of the device.[29–35] For this reason the community of material scientists is now putting great effort in the investigation of mixed halide perovskite in order to improve the stability of the devices without loss in performance.

Mixed Iodide-Chloride ($I_{3-x}Cl_x$). While the employment of pure Cl-based perovskite is of very little interest to the photovoltaic community, mainly due to the high energy bandgap of this material, starting from the pioneering work by Lee et al.[14] the Cl incorporation within $MAPbI_3$ is regarded as one of the main route towards high efficiency PSCs. Recent works showed that using a mix of lead Chloride ($PbCl_2$) and methilammonium iodide salt (MAI) as precursors one can obtain a Cl doped $MAPbI_3$ perovskite showing an improved carrier diffusion length and photoluminescence lifetime with respect to the pure Iodide material, despite showing identical bandgap.[36,37] More recently Docampo et al. investigated the effect of an increasing Cl doping (from 0 wt% to 20 wt%), showing that while the PL lifetime monotonically increase with the Cl content, the device performances are optimized with a very little content (5 wt%).[38] At the same time Grancini et al.,[39] through Raman and XRD measurements, highlighted the absence of the Cl ion within the unit cell. However they pointed out that, in the planar structure, the presence of Cl source drives the crystallization process inducing a preferential order of the organic moiety thus leading to the formation of larger and oriented perovksite grians. As we will discuss in more detail in section 4.3, this doping induced change in the film morphology is intertwined with the

optoelectronic properties.

Bromide (Br) Thanks to its high miscibility, the Bromide-Iodide halide exchange has been shown both in perovskite nano-crystals and thin films.[40,41] Notably the Br inclusions provoke a compressive stress of the Pb-I cage causing a structural distortion that in turn lead to a continuous shift of the band-gap,[42] thus enabling a precise tunign of the material absorption onset via chemical control of the reactants ratio. Recent works reported mixed Br-I based solar cells showing both a tunable bandgap ranging within 1.48 and 2.23 eV, with a champion device showing a PCE of 14.2%,[20] and an improved long-term stability,[43] mainly ascribed to the reduced moisture sensitivity.

Beside the mixed halide, the pure halide $MAPbBr_3$ has been widely investigated semiconducting material for light-emitting devices. The long carrier lifetime and high charge mobility,[44] together with the low non-radiative recombination rates make $MAPbBr_3$ an ideal material for semiconductor lasers and light emitting-diodes. Notably some preliminary works both in lasing[45,46] and electro-luminescent[47] devices have been recently reported.

As a consequence of the brief material perspective reported above we believe that a thorough understanding of the photophysics underlying the optical properties of the pure halides materials is, at this stage, mandatory. In the following we will focus our attention on both the experimental observation and modeling of steady-state and time-resolved photon-absorption (chapter 3) and photo-luminescence (chapters 4 and 5) properties of $MAPbI_3$ and $MAPbBr_3$.

1.2 Review of the fundamental opto-electronic properties of semiconductors

UV-Vis optical absorption measurements,[18,26,32] presenting a steep absorption edge, and DFT calculations reported in literature[48,49] show that hybrid perovskite are characterized by a direct-bandgap semiconductor like optical behavior. The electronic structure of hybrid lead-halide perovskite is mainly defined by the B-X bond angle in the inorganic cage structure. In particular recent studies on the electronic structure of 2D and 3D perovskite showed that the valence band maximum and conduction band minimum are determined respectively by an antibonding hybrid orbital between the *B-s* orbital and *X-p* orbital and a non-bonding hybrid state between the *B-p* and the *X-p*.[48,50,51] Notably the reverse ordering of the band-edge states (a p-like conduction band) with respect to the broadly studies III-V semiconductors, result in some peculiar optical properties such as thy splitting of the conduction band, rather then the valence band,[52] and an anomalous Varshni-shift[53] as explained in the following.

As already mentioned, while not directly contributing to the electronic structure, the cation A steric hindrance can cause a distortion of the B-X bond[54,55] affecting the symmetry, thus influencing electronic and optical properties, as we will discuss more deeply in the section 3.4

For the sake of the clarity in this section we report a brief summary of the semi-classical light-matter interaction for direct band-gap semiconductor.

1.2.1 Band structure

On first approximation a 3D semiconductor can be effectively described as N interacting one electron system organized into a crystal lattice. Despite the apparent simplicity of this model this is, in principle, a multi-particle problem since each electron is interacting both with the lattice nuclei and with all other electrons. However within the *independent electron approximation* one can discard the electron-electron interaction potential $V_{e-e}(\mathbf{r})$ and represent the electron-lattice interaction with a *single electron effective potential* $V_{eff}(\mathbf{r})$ with the periodicity of the underlying lattice. However complex the V_{eff} expression can be, qualitatively it can be expected to have the shape displayed in figure 1.3a, where the effective potential (solid line) matches the individual atomic potential (dashed lines) close to the lattice sites while it gets flat between them.

Thanks to the definition of this single particle potential the problem reduces to the solution of a single electron Schröedinger equation:

$$H_0\psi(\mathbf{r}) = \left[-\frac{\hbar^2}{2m}\nabla^2 + V_{eff}(\mathbf{r})) \right]\psi(\mathbf{r}) = E\psi(\mathbf{r}). \tag{1.2}$$

where ψ have a known form and take then name of *Bloch states*. In fact, according to the Bloch theorem,[53] as a consequence of the periodicity of V_{eff} these state have the form of a plane wave times a function with the lattice periodicity:

$$\psi(\mathbf{r}) = u_k(\mathbf{r})e^{i\mathbf{k}\cdot\mathbf{r}} \tag{1.3}$$

where u_k is the periodicity function of the crystal lattice. Solving equation 1.2 for a wavefunction of the form 1.3 it can be shown that the problem eigenvalues lie within two allowed energetic bands that are defined as *valence* (E_v) and *conduction* (E_c) band respectively.

(a)   (b)
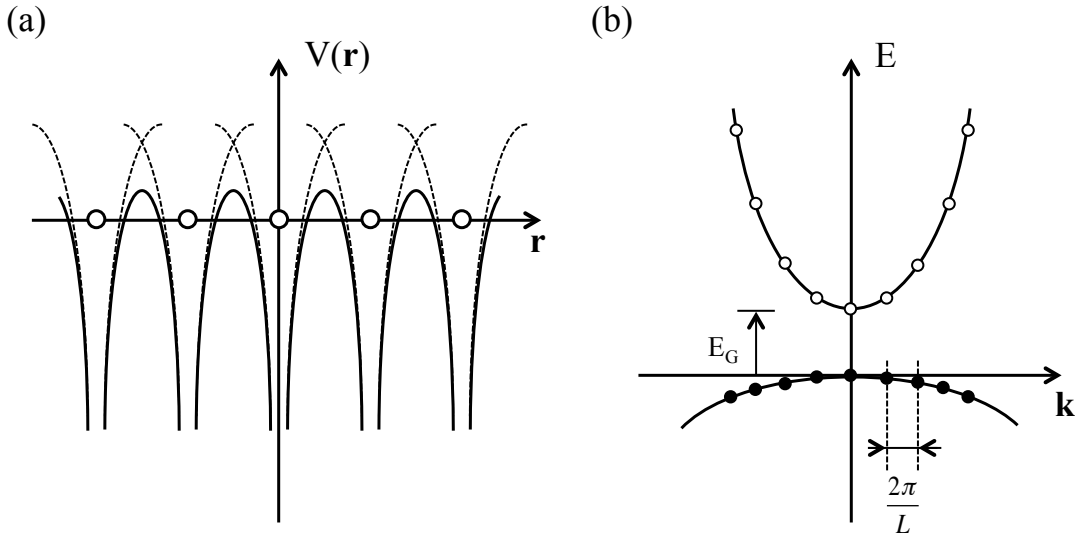
Figure 1.3: *(a) Periodic potential for a 1-D lattice (solid lines) superimpose to the isolated ions potentials (dashed lines). (b) Dispersion relation for a finite semiconducting crystal.*

The relation between the energy of each allowed state and its wave-vector $\mathbf{k}$ is defined as *dispersion reletaion* $E(\mathbf{k})$. When the wave-vector $\mathbf{k}$ is little enough one can approximate the *dispersion relation* $E_{v,c}(\mathbf{k})$ with a parabola, which in the reference system of figure 1.3b can be written as:

$$
\begin{aligned}
E_v &= -\frac{\hbar^2 k^2}{2m_v}, \quad with \quad m_v = \frac{\hbar^2}{\frac{\partial^2 E_v}{\partial k^2}} \\
E_c &= E_G + \frac{\hbar^2 k^2}{2m_c}, \quad with \quad m_c = \frac{\hbar^2}{\frac{\partial^2 E_c}{\partial k^2}}
\end{aligned}
\tag{1.4}
$$

where $m_{v,c}$ is the *effective mass* of the electron at the top/bottom of the valence/conduction band. This is know as the *parabolic band approximation.*

In the case of a spatially finite semiconducting crystal the boundary conditions, i.e. the periodicity of the structure, impose that the total phase shift of the Bloch state $\mathbf{k} \cdot \mathbf{r}$ is a multiple of 2π. Thus, given a certain crystal dimensions $(L_x \cdot L_y \cdot L_z)$, k will only assume the discrete values $k_i = \frac{2\pi l}{L_i}$, $i = x, y, z$ and each state will occupy a definite volume $\Delta\mathbf{k}$ in the k-space:

$$
\Delta\mathbf{k} = \frac{(2\pi)^3}{L_x L_y L_z}
\tag{1.5}
$$

Note that in this approximations the electrons are treated as free particle within the conduction band , thus their crystal momentum will be $\mathbf{p} = \hbar\mathbf{k}$.[53]

1.2.2 Density of states

In the following we will limit our discussion to the case of an *intrinsic 3D* semiconductor (i.e. L_i much larger than the electrons de Broglie wavelength), with a *direct band-gap*, being these approximations suitable for the scope of our discussion.

Considering again the $\mathbf{k}$-space we can evaluate the number of allowed electronic states, with wavevector ranging from 0 to k, as the ratio between the volume of the sphere of radius k and the unit cell volume $\Delta\mathbf{k}$, time a factor 2 accounting for the electron spin.

$$
N(k) = 2\frac{4/3\pi k^3}{(2\pi)^3/(L_x L_y L_z)} = \frac{k^3 V}{3\pi^2}
\tag{1.6}
$$

The density of state per unit volume is then readily evaluated as:

$$
\rho_{c,v}(k) = \frac{dN}{V\,dk} = \frac{k^2}{\pi^2}
\tag{1.7}
$$

or, as a function of energy $(\rho_{c,v}(E)dE = \rho_{c,v}(k)dk)$:

$$
\rho_{c,v}(E_{c,v}) = \frac{1}{2\pi^2}\left(\frac{2m_{c,v}}{\hbar^2}\right)^{3/2}\sqrt{E_{c,v}}
\tag{1.8}
$$

where E_c and E_v are measured from the bottom of the conduction band ($E_c = E - E_G$) and top of the valence band ($E_c = -E$) respectively. Note that the density of states reported here was evaluated considering a 3D k-space, thus its form will vary in the case of *quantum confined* systems.[56]

Electrons, being fermion, follow Fermi-Dirac statistics, thus if we consider the semiconductor in thermal equilibrium the occupation probability of a given level of energy E will be:

$$f(E) = \frac{1}{1 + e^{(E - E_F)/kT}} \tag{1.9}$$

where k now stands for the Boltzman constant and E_F the Fermi level. In the case of an intrinsic semiconductor E_F will lie in the middle of the bandgap thus giving a fully occupied valence band and an empty conduction band (figure 1.4a).
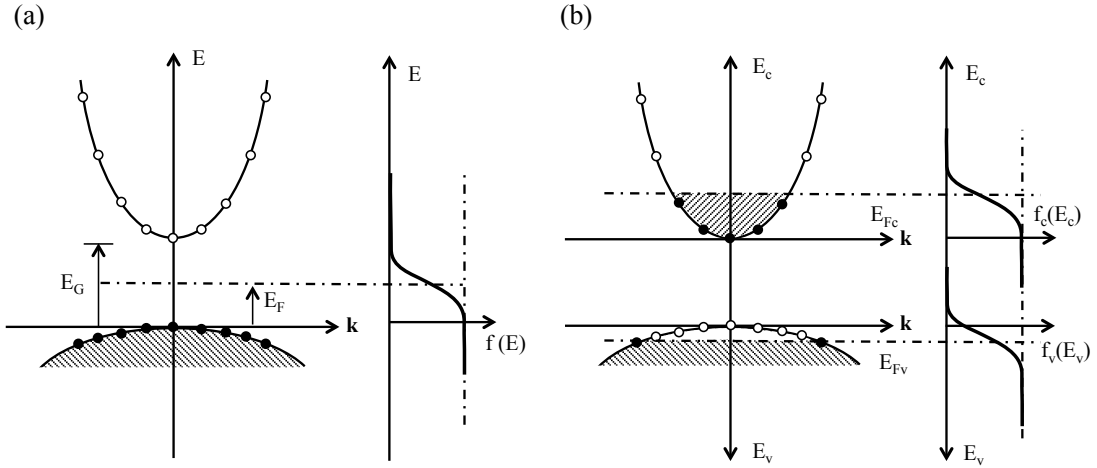
Figure 1.4: *Dispersion relations and occupation probability function in thermal equilibrium (a) and quasi-thermal equilibrium (b) condition.*

Upon light absorption some electrons will be raised from the valence to the conduction band leaving behind an equivalent hole (electron vacancies) density. Since the intraband relaxation time ($\approx 1ps$[52,57]) of electron/holes within the conduction/valence band is much faster with respect to the interband relaxation, i.e. electron hole recombination, being between 1-100 ns[32,36,37] we can safely assume that a thermal equilibrium is established within each of the band allowing the definition of an occupation probability f_c and f_v for the conduction and valence band respectively. In this so called *quasi-equilibrium approximation* E_{Fc} and E_{Fv} represents the *quasi*-Fermi level for each band, which indicate the energy level up to which each band is fully occupied at T = 0K, as shown in figure 1.4b where the shaded areas indicate the filled states.

Note that one can define the hole occupation probability for holes in the valence band simply as $\bar{f}_v = 1 - f_v$. We can, thus, calculate the density of electrons in the conduction and holes in the valence band just integrating over the energy the product of the density of states and the occupation probability functions. Notice

that in this case we defined two separate energy scales for the conduction and valence band (refer to figure 1.4) in order to make the integral evaluation simpler.

$$
\begin{aligned}
N_e &= \int_0^\infty \rho_c(E_c) f_c(E_c) dE_c \\
N_h &= \int_0^\infty \rho_v(E_v) \bar{f}_v(E_v) dE_v
\end{aligned}
\tag{1.10}
$$

Eventually it's interesting to notice that the quasi-Fermi level of each band is univocally define by the injected carrier density of electron (holes) according to the following expression:

$$
N = N_c \frac{2}{\sqrt{\pi}} \int_0^\infty \frac{\sqrt{\epsilon}}{1 + e^{\epsilon - \epsilon_F}} d\epsilon
\tag{1.11}
$$

where $N_c = 2\left(2\pi m_c kT/h^2\right)^{3/2}$, $\epsilon = E_c/kT$ and $\epsilon_F = E_F/kT$.

1.2.3 Optical transitions

Absorption coefficient

Let's now consider the interaction between the semiconductor and an electromagnetic wave. In the case of a simple plane wave we can write the electric field as:

$$
\mathbf{E}(\mathbf{r}, t) = \mathbf{E}_0 e^{i(\mathbf{k}_{opt} \cdot \mathbf{r} - 2\pi\nu t)}
\tag{1.12}
$$

where $\mathbf{k}_{opt}$ is the optical wave vector. Ia a **_dipole approximation_** framework we can write the perturbation Hamiltonian H' as:

$$
H' = -e\mathbf{E} \cdot \mathbf{r}
\tag{1.13}
$$

Within the _perturbation theory_ approximation the transition rate W between two Bloch state ψ_1 and ψ_2 of energy E_1 and E_2 is given by the Fermi Golden Rule:

$$
W = \frac{\pi^2}{\hbar^2} |H_{12}'^{(0)}|^2 \delta(\nu - \nu_0)
\tag{1.14}
$$

where $\nu_0 = (E_2 - E_1)/h$ and

$$
|H_{12}'^{(0)}|^2 = \left| \int \psi_2^*(-e\mathbf{r} \cdot \mathbf{E}_0 e^{i(\mathbf{k}_{opt} \cdot \mathbf{r})}) \psi_1 dV \right|^2
\tag{1.15}
$$

are respectively the energy and the transition matrix element of the optical transition of interest.

In this approximation the transition rate is non-null only when:

(a) the optical photon energy matches the transition energy: $E = h\nu$ (energy conservation),

(b) the wave-vectors satisfy the relation $\mathbf{k}_2 = \mathbf{k}_{opt} + \mathbf{k}_1$ (k-conservation).

In fact $|H_{12}'^{(0)}|$ is the integral over the entire space of a function oscillating as $i(\mathbf{k}_1 + \mathbf{k}_{opt} - \mathbf{k}_2) \cdot \mathbf{r}$, thus this will be non vanishing only when the oscillating term is null.

Notice that since $\mathbf{k}_{1,2} = p/\hbar \simeq m_{1,2}v_{th}/\hbar \approx 10^{6-7}cm^{-1}$ while $\mathbf{k}_{opt} = 2\pi n/\lambda \approx 10^5 cm^{-1}$, then the k-conservation result in:

$$k_2 = k_1 \tag{1.16}$$

which is referred to as *dipole selection rule*, indicating that the optical transition must be vertical in the energy dispersion diagram.

Given a certain impinging electromagnetic wave intensity I we define the optical transition cross section σ as the ration between the rate W of the transition and the corresponding photon flux $F = I/h\nu$:

$$\sigma = \frac{W}{F} \tag{1.17}$$

Being $I = \frac{1}{2}\varepsilon_0 n|\mathbf{E}_0|^2$ we obtain:

$$\sigma = h\nu \frac{2W}{\varepsilon_0 n|\mathbf{E}_0|^2} = \frac{2\pi^2\nu}{n\varepsilon_0 ch}\frac{\mu^2}{3}g(\nu - \nu_0) \tag{1.18}$$

where $g(\nu - \nu_0)$ is a function accounting for the electron-phonon interaction induced broadening, and $\mu = \int u_1 e\mathbf{r}u_2 dV$ is the matrix element upon satisfaction of the selection rule. Notice that the 1/3 term arises from the average along the three possible $\mathbf{k}$ directions.

In order to evaluate the absorption coefficient it is now necessary to evaluate the elemental number of transitions $dN(E_0)$ which energy lie between E_0 and $E_0 + dE_0$. This number can be evaluated as $dN = \rho_j(E_0)dE_0)$ where ρ_j is the density of possible transition from the valence to the conduction band satisfying the energy and $\mathbf{k}$ conservation, referred as the *joint density of state*. In order to satisfy the energy conservation we will have that:

$$E_0 = \left(E_c + \frac{\hbar^2 k_2^2}{2m_c}\right) - \left(E_v + \frac{\hbar^2 k_1^2}{2m_v}\right) \tag{1.19}$$

where, given that $E_{c,v}$ represent the top (bottom) of the conduction (valence) band, we have defined the energy level involved in the transition as $E_{2,1} = E_{c,v} + \hbar^2 k_{1,2}^2/(2m_{c,v})$. Considering the momentum conservation ($k_1 \simeq k_2 \simeq k$) and defining the electron-hole reduced mass $\frac{1}{m_r} = \frac{1}{m_v} + \frac{1}{m_c}$:

$$E_0 = (E_c - E_v) + \frac{\hbar^2 k^2}{2\mu} = E_G + \frac{\hbar^2 k^2}{2m_r} \tag{1.20}$$

Under the above mentioned selection rules we know that for each state in the valence band there is only one corresponding state in the conduction band, thus

the number of transition will be equal to the number of state (either in conduction or valence band), i.e. $\rho_j dE_0 = \rho(k)dk$. Thus using equation 1.7 and the relation $\nu_0 = E_0/h$ we retrieve:

$$\rho_j(\nu_0) = \frac{4\pi}{h^2}\,(2m_r)^{3/2}\sqrt{h\nu_0 - E_G} \tag{1.21}$$

i.e. the density of transitions with frequency lying between ν_0 and $\nu_0 + d\nu_0$. The number of net absorption transitions dN at frequency ν_0 will be given by the difference between the number of absorption transitions dN_a, determined by the probability of having an electron in the valence band $f_v(E_1)$ and an empty state in the conduction band $1 - f_c(E_2)$, and the number of stimulated emission transitions dN_{se} which are defined, conversely, by the probability of having a free state in valence band $1 - f_v(E_1)$ and an occupied state in conduction band $f_c(E_2)$:

$$dN(\nu_0) = dN_a - dN_{se} = \rho_j(\nu_0)d\nu_0[f_v(E_1) - f_c(E_2)] \tag{1.22}$$

Ultimately the *absorption coefficient* at frequency ν is obtained as $d\alpha = \sigma(\nu - \nu_0)dN(\nu_0)$ where the homogeneously broadened transition cross section σ is given by equation 1.18.

$$d\alpha(\nu_0) = \left(\frac{2\pi^2\nu}{n\varepsilon_0 ch}\right)\frac{\mu^2}{3}g(\nu - \nu_0)\rho_j(\nu_0)[f_v(E_1) - f_c(E_2)]d\nu_0 \tag{1.23}$$

assuming that each transition's broadening $g(\nu - \nu_0)$ is much narrower than the join density of state function and the occupation probability we can treat $g(\nu - \nu_0)$ as a delta function and thus retrieve the absorption coefficient $\alpha(\nu) = \int_0^\infty d\alpha(\nu_0)$:

$$\alpha(\nu) = \left(\frac{2\pi^2\nu}{n\varepsilon_0 ch}\right)\frac{\mu^2}{3}\rho_j(\nu)[f_v(E_1) - f_c(E_2)] \tag{1.24}$$

For a visible-band gap semiconductor $E_G \gg kT$, thus $f_v(E_1) \approx 1$ and $f_c(E_2) \approx 0$ giving:

$$\alpha(\nu) \simeq \alpha_0 = \frac{\pi^3\nu}{n\varepsilon_0 ch^3}\frac{\mu^2}{3}(2m_r)^{3/2}\sqrt{h\nu - E_G} \tag{1.25}$$

Optical gain

If we now reconsider equation 1.22 in the case in which the stimulated emission events exceed the absorption events we can define the *optical gain* as $g = \alpha_0[f_c(E_2) - f_v(E_1)]$. In order to have a net optical gain we have to impose that $f_c(E_2) - f_v(E_1) > 0$ thus retrieving a condition for the quasi-Fermi level of the conduction and valence band:

$$E_G \leq h\nu \leq E_{Fc} - E_{Fv} \tag{1.26}$$

known as the Bernard-Douraffourg condition. The equal case gives a null gain g = 0 and the corresponding injected carrier density is defined *transparency density*

N_{tr}. When the injected carrier density exceed N_{tr} there will be a positive optical gain:

$$g = \sigma(N - N_{tr}) \tag{1.27}$$

where σ is referred to as the differential gain $\sigma = dg/dN$.

1.2.4 Excitonic semiconductor absorption

The results reported in the previous section are based on the assumption of a full delocalization of the electron wavefunction over the entire lattice. In other words the Bloch state picture is taking into account the electron-lattice interaction though leaving aside the electron-electron interaction, i.e. the fact that once one electron is promoted from the valence to the conduction band its presence will affect all the other states available in the crystal. While that works as a good approximation for most commonly used semiconductors characterized by a good local screening of the free-carrier interaction, that is not always the case for hybrid organic-inorganic perovskite semiconductors which in some cases can show excitonic behaviour.[57–60]

In order to tackle this problem we should reconsider the Schröendinger equation with a semi-classical many-body Hamiltonian:

$$i\hbar\frac{\partial}{\partial t}\psi = [\psi, H] \tag{1.28}$$

where $H = H_0 + H_c + H'$ with H_0 being the single particle part, H_C the Coulombian interaction Hamilatonian and H' the electromagnetic field interaction already introduced in equation 1.13. It's interesting to notice that at 1st order approximation the homogeneous part of the linearized problem results to be[61] :

$$\left[\frac{\hbar^2\nabla_{\mathbf{r}}^2}{2m_r} - V(\mathbf{r})\right]\phi_\nu(\mathbf{r}) = E_\nu\phi_\nu(\mathbf{r}) \tag{1.29}$$

which is called the *Wannier equation*, a problem mathematically identical to the Schröedinger equation of the hydrogen atom. The bound solutions of equations 1.29 are defined as Wannier-Mott excitons which can be depicted as particles constituted of a tightly bound electron-hole pair moving together with a reduces mass $m_r = (\frac{1}{m_e} + \frac{1}{m_h})^{-1}$, while the unbound ones represent the Coulomb interacting free carriers states.

In order to get the adsorption coefficient it possible to compute the electron-hole susceptibility $\chi(\nu)$ (refer to Koch[62] for a detailed discussion) and then retrieve the absorption coefficient as $\alpha(\nu) = (\frac{2\pi\nu}{cn})\Im[\chi(\nu)]$:[63]

$$\alpha(\nu) = \alpha_0^{3D}\left[\sum_{n=1}^{\infty}\frac{4\pi E_b^{3/2}}{n^3}\delta\left(h\nu - E_G - \frac{E_b}{n^2}\right)+\right.$$

$$\left.\frac{2\pi\sqrt{E_b}}{1 - e^{-2\pi\sqrt{\frac{E_b}{h\nu - E_G}}}}\quad \theta(h\nu - E_G)\right] \tag{1.30}$$

where $\alpha_0^{3D} = \frac{\pi^3 \nu}{n\varepsilon_0 ch^3}\frac{\mu^2}{3}(2m_r)^{3/2}$ is the prefactor related to the 3D joint density of states and n is a positive integer.

Equation 1.30 was first elaborated by Elliott[64] and it shows that 3D exciton absorption consist of two contribiutions:

(a) a series of resonance line at frequency $\frac{E_b}{h}\frac{1}{n^2}$ with a rapidly decreasing oscillator strength $(\propto n^{-3})$,

(b) a ionized states absorption α_{cont} contribution

The energy of the exciton ground state E_b is referred to as **_binding energy_**, in fact this is the energy difference between the first bound state $(n = 1)$ and the bottom of the conduction band, i.e. the exciton ionization energy.

Notably comparing this continuum contribution and equation 1.25, we can write a relation between the free-carrier absorption α_{free} and the ionized states one:

$$\alpha_{cont} = \alpha_{free}C(\nu) \tag{1.31}$$

where

$$C(\nu) = \frac{2\pi}{1 - e^{-2\pi\sqrt{\frac{E_b}{h\nu - E_G}}}}\sqrt{\frac{h\nu - E_G}{E_b}} \tag{1.32}$$

is the _Sommerfeld correction_ factor. Notice that for $h\nu \rightarrow E_G$ then $C(\nu) \rightarrow 2\pi\sqrt{\frac{E_b}{(h\nu - E_G)}}$, showing a striking difference with the square root behavior displayed by eq. 1.25.
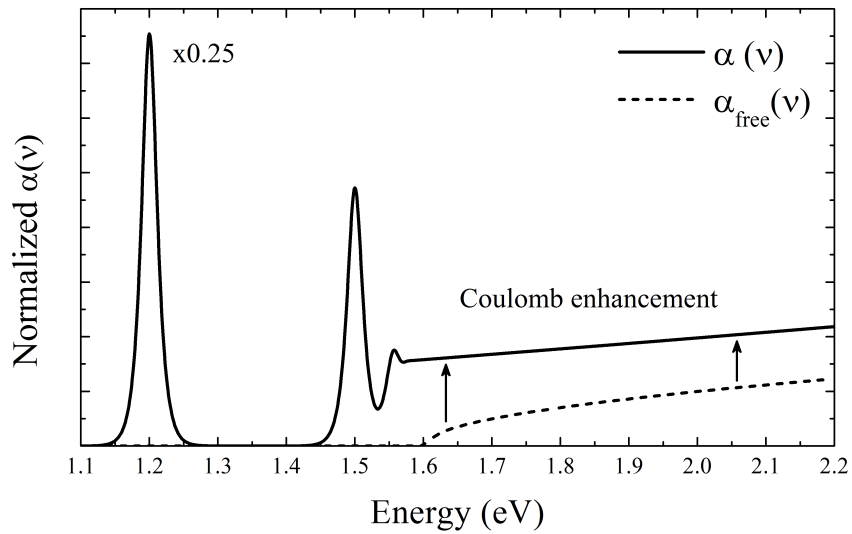
Figure 1.5: _Calculated band edge absorption for a 3D semiconductor with (solid line) and without (dashed line) accounting for electron-electron interaction._

In figure 1.5 we reported the simulated absorption coefficient for a 3D semiconductor according to equation 1.30 (solid line) and equation 1.25 (dashed line), in both cases we took into account a thermal broadening through the convolution of $\alpha(h\nu)$ with an hyperbolic secant of width Γ. For the seek of the discussion we simulated a very high binding energy system (E_b = 400 meV) with low thermal broadening (Γ = 10 meV). Is interesting to notice that if a 2D system is considered the Sommerfeld correction factor is so that as $h\nu \to E_G$, then $C^{2D}(\nu) \to 2$ converging to a constant value.[62] This difference between 2D and 3D excitonic semiconductor can be a useful tool to identify the dimensionality of the excitonic system with a simple inspection of the absorption spectrum.

1.2.5 Photo-Luminescence

Once the semiconductor has been photo-excited a number of different relaxation processes can take place, taking the system back to its ground state.

Among them we can make a macroscopic distinction between *radiative* and *non-radiative* relaxation processes. While the radiative recombination, both in *spontaneous* and *stimulated* photon emission, is an intrinsic property of the material, the non-radiative recombination can be due both to intrinsic properties, as in the case of *Auger* recombination process, and extrinsic properties such as localized trap states due to impurities and defects in the crystal structure.

It has been broadly reported that the excited state de-population of hybrid organic-inorganic perovskite can be effectively described with a rate equation such as:[65, 66]

$$\frac{dn}{dt} = -R(n) - k_t n - \gamma n^3 \tag{1.33}$$

accounting for the spontaneous radiative recombination rate $R(n)$, an extrinsic non-radiative recombination rate k_t describing carrier trapping and a non-radiative Auger recombination process, which is known to go like $\approx n^3$. Notice that the photoluminesce (PL) intensity will be proportional to the radiative rate ($I_{PL} \propto R(n)$) which in general is a function of the excited population density. Thus different decay path will directly influence the photo-emission properties of the material.

In this section we present a review of the three main recombination mechanisms involved in the excited state population decay in a direct-band gap semiconductor material and in relation of the specific hybrid organic-inorganic perovskite case.

Spontaneous Emission

Let's consider two generic state ψ_1 and ψ_2 laying in the valence and conduction band respectively and let's define the spontaneous emission rate R_ν so that $R_\nu d\nu$ stands for the number of spontaneous emission events per unit time and volume resulting in the emission of a photon with frequency between ν and $\nu + d\nu$. As described above the number of transitions with frequency lying within ν_0 and $\nu_0 + d\nu_0$ is furnished by the *joint density of state* $\rho_j(\nu_0 d\nu_0)$ (c.f.r. 1.21). These will contribute with an elemental contribution dR_ν to the overall rate:

$$dR_\nu = A_{21}\rho_j(\nu_0)d\nu_0 g(\nu - \nu_0)f_c(E_2)[1 - f_v(E_1)] \tag{1.34}$$

where A_{21} is the spontaneous emission rate in a two levels system, $g(\nu - \nu_0)$ is the emission line shape and $f_{c,v}$ are the occupation probability functions for the conduction/valence bands evaluated respectively at the two states energies.

In the limit of $g(\nu - \nu_0)$ being approximated with a δ function the spontaneous emission rate is readily evaluated as:

$$R_\nu = \int_\nu^{\nu+d\nu} dR_\nu d\nu_0 = A_{21}\rho_j(\nu)f_c(E_2)[1 - f_v(E_1)] \tag{1.35}$$

Notice that the rate is defined by the probability of having a filled state in conduction band $f_c(E_2)$ times the probability of having an empty state in the valence band $[1 - f_v(E_1)]$.

Following Einstein's treatment for the spontaneous (A_{21}) and stimulated (B_{21}) emission rate in a two level system[56, 67] and recalling that B_{21} is the transition rate W by the energy density of the e.m. wave $u_E = nI/c = nFh\nu/c$ we can write:

$$A_{21} = \left(\frac{8\pi h\nu^3 n^3}{c^3}\right)B_{21} = \left(\frac{8\pi h\nu^3 n^3}{c^3}\right)\frac{Wc}{nh\nu F} \tag{1.36}$$

Plugging in equation 1.36 into 1.35 and recalling the definition of the absorption coefficient $\alpha(\nu) = \sigma\rho_j(\nu)[f_v(E_1) - f_c(E_2)]$ where σ is the transition cross section given by 1.17 we can write the spontaneous emission rate as a function of the transition as:

$$R_\nu = \left(\frac{8\pi\nu^2 n^2}{c^2}\right)\alpha(\nu)\frac{f_c(E_2)[1 - f_v(E_1)]}{f_v(E_1) - f_c(E_2)} \tag{1.37}$$

Notice that the transition rate is governed by a precise relation between the occupation probability functions $f_{c,v}$. Defining $\Delta\mu = E_{Fc} - E_{Fv}$ and recalling that $h\nu = E_2 - E_1$ one can show that:

$$f = \frac{f_c(E_2)[1 - f_v(E_1)]}{f_v(E_1) - f_c(E_2)} = \frac{1}{e^{(h\nu-\Delta\mu)/kT} - 1} \tag{1.38}$$

which is the probability function driving the photon flux from a biased black body $b(\nu, \Delta\mu)$.[68] Thus we can write the emission rate as function of the biased black body emission and the absorption coefficient:

$$R_\nu = \alpha(\nu)b(\nu, \Delta\mu) \tag{1.39}$$

Eventually the overall spontaneous emission rate will be evaluated as the integral over all transitions frequencies ν

$$R = \int_0^\infty \alpha(\nu)b(\nu, \Delta\mu)d\nu \tag{1.40}$$

Notice that sometimes the spontaneous emission rate is defined as the *net* emission rate which can be evaluated from 1.40 subtracting the emission at thermal equilibrium, i.e. $\int \alpha(\nu) b(\nu, 0) d\nu$.

Since for a non degenerate semiconductor $h\nu - \Delta\mu >> kT$, equation 1.38 can be approximated with a Boltzmann distribution $\approx e^{(h\nu - \Delta\mu)/kT}$. In this case we can easily redefine our rate as a function of electron-hole densities since it can be shown that for a semiconductor at quasi-thermal equilibrium holds the following relation:

$$np \propto e^{(h\nu - \Delta\mu)/kT} \tag{1.41}$$

where n and p are the electrons and holes density respectively, evaluated according to equation 1.10, giving:

$$R = \beta_{rad} \, np \tag{1.42}$$

where β_{rad} is carrier density independent and is an intrinsic property of the material.

In the simple case where no other phenomena is considered one will have $n(t) = p(t)$. Thus the general rate equation will be $dn/dt = R_G - \beta_{rad} n^2$ where R_G is the charge photogeneration rate. Solving this equation with $n(0) = 0$ one obtains the time evolution of the excited state population density $n(t)$, and in particular it results that at early times ($t \approx 0$) $n(t) \propto R_G t$. Eventually, since $R_G \propto I_{ex}$, the PL intensity at early times will be a quadratic function of the light excitation intensity:

$$I_{PL}(0) \propto \beta_{rad} n^2(0) \approx I_{ex}^2 \tag{1.43}$$

Once the excited state population is built we can apply the initial condition $n(t = 0) = n(0)$, and consider the simplified rate equation $dn/dt = -\beta_{rad} n^2$ in order to get the PL decay trace. This is the so called *bi-molecular* recombination which can be readily integrated giving:

$$n(t) = \frac{n(0)}{(\beta_{rad} n(0) t + 1)} \tag{1.44}$$

and:

$$I_{PL}(t) \propto \beta_{rad} n^2(t) = \frac{\beta_{rad} n^2(0)}{(\beta_{rad} n(0) t + 1)^2} \tag{1.45}$$

Shockley–Read-Hall recombination

When on need to consider the recombination from the conduction (valence) band to a localized state, such as an intra-gap trap, we can replace the the valance (conduction) band DOS with that of the considered localized states in the above treatment thus retrieving a recombination rate given by equation 1.42 but where p (n) is replaced by the density of trapped electrons $N_t(1 - f_t)$ (holes):

$$R_{nt} = \beta_n \, n N_t (1 - f_t) \tag{1.46}$$

where N_t is the density of trap states and f_t is the probability that a trap state is occupied.

If we now consider a semiconductor in which both electron and holes can be trapped we should define two distinct coefficients $\beta_{n,p}$ and two de-trapping rates $G_{n,p}$. Considering that at equilibrium one will have that the trapping and de-trapping rate should balance ($R_{nt,pt} = G_{n,p}$) one can retrieve the expression for the four above mentioned rate as a function of the trap occupation probability f_t:

$$R_{nt} = \beta_n \, n N_t (1 - f_t) \qquad G_n = \beta_n n_t N_t f_t$$

$$\tag{1.47}$$

$$R_{pt} = \beta_p \, p N_t f_t \qquad G_p = \beta_p p_t N_t (1 - f_t)$$

where n_t and p_t are the electrons (holes) density when the quasi-fermi level matches the trap energy E_t. Eventually one can eliminate the trap states occupation probability f_t imposing that at the steady state condition net trapping rate of electrons matches the net recombination rate for the holes, i.e. $R_{nt} - G_n = R_{pt} - G_p$, eventually getting the expression for the Shocley Read Hall expression for recombination through a trap state:

$$R_{SHR} = \frac{np}{\tau_n(p + p_t) + \tau_p(n + n_t)} \tag{1.48}$$

where we have defined the average lifetime for electrons/holes capture $\tau_{n,p} = \frac{1}{\beta_{n,p}N_t}$.

We consider a simple case in which the density of available trap states is always greater than the free e-h pair, so that $n(t) = p(t) >> n_t$, and $\tau_n = \tau_p$ and obtain:

$$R_{SRH} \approx \frac{n^2}{2\tau_n n} = \beta_n N_t n \tag{1.49}$$

Different from the previous case, here the excited state de-population is described by a *monomolecular* recombination mechanism ($dn/dt = R_G - \beta_n N_t n$). In this case $R_G \propto n(0)$ thus, remembering that $R_G \propto I_{ex}$, one get a linear dependence of the PL emission with respect to the excitation density ($I_{PL}(0) \propto I_{ex}$) and a *mono-exponential* decay trace:

$$I_{PL}(t) \propto \beta_n N_t n(t) \approx n(0) e^{-t/\tau_n} \tag{1.50}$$

Auger recombination

Auger recombination is a three particles process in which two carrier of the same sign undergoes an elastic scattering event resulting in the excitation of one carrier to higher kinetic energy, and the recombination of the second with an available carrier of the opposite sign.

In the case of a band-like semiconductor the Auger recombination will involve either two electrons and one hole (R_{Aug}^{eeh}) or two holes and one electron (R_{Aug}^{hhe}). Thus, following an argument similar to the one presented above, one retrieve a recombination rate proportional to the electrons and holes densities:

$$R_{Aug}^{eeh} = A_p n^2 p \qquad R_{Aug}^{hhe} = A_n n p^2 \qquad (1.51)$$

where in the case we take for simplicity $n(t) = p(t)$, as we did in equation 1.33, one simply get a cubic behavior of the Auger rate with respect to the excited state population density:

$$R_{Aug} = \gamma n^3 \qquad (1.52)$$

This recombination mechanism is usually more relevant in the indirect band-gap semiconductor since the radiative recombination is hindered, however it can be observed also in direct band-gap semiconductor in high carrier density regimes.

Methods

2.1 Introduction

In this chapter we will briefly describe the experimental details of our research. We start discussing the samples fabrication procedures, subsequently we furnish the specifications of the commercial setups employed for the standard characterization and eventually we describe the custom-built setup for the time resolved photoluminescence measurements and the excitation cross-correlation measurements.

2.2 Sample fabrication

2.2.1 MAPbI$_3$

The precursor solution of perovskite was prepared following the well-established method reported in literature (refs).

Methylamonium Iodide salt. Methylamine (CH_3NH_2 = MA) solution 33 wt% in absolute ethanol was reacted with hydroiodic acid (HI) 57 wt% in water with excess methylamine at room temperature. After about two hours stirring, we added ethanol in order to facilitate the subsequent crystallization of the salt. Typical quantity reacted are: 96 ml of methylamine solution, 40 ml of hydroiodic acid and 400 ml of ethanol. Crystallization of methylammonium iodide salt (CH_3NH_3I = MAI) was achieved using a rotary evaporator. A white colored powder was formed indicating successful crystallization. The salt was then washed two times in diethyl ether to increase its purity.

Lead Iodide. A lead iodide (PbI_2) solution in N,N-Dimethylformamide (DMF) (462 mg/ml) was heated at 70°C and then spun at 4000 rpm for 60 seconds onto

a clean glass substrate. A subsequent annealing at $70°C$ for 30 min is required in order to obtain a stable PbI_2 thin film substrate. The glass cleaning procedure consisted in a sonicator bath for 20 minutes (10 min Acetone, 10 min IPA) and 10 minutes of O_2 plasma cleaning.

2-step deposition. These substrates were then dipped in a MAI solution in IPA at different concentration and different temperature for 2 minutes in order to get different average crystallite size samples. All the samples were finally rinsed in anhydrous IPA to remove the non-reacted organic precursor. In the following table we report the exact values of temperature and concentration of the MAI solution together with the average crystallite size obtained, as observed from top-view SEM images.

[MAI] (M)	T ($°C$)	Avg. crystallite size
0.063	25	$< 250nm$
0.045	25	$\approx 500nm$
0.031	25	$\approx 650nm$
0.045	70	$\approx 1\mu m$
0.045	90	$\approx 2\mu m$
0.031	70	$\approx 4\mu m$
0.031	90	$> 5\mu m$

Table 2.1: *MAI solution concentrations and temperatures for 2-step deposition technique.*

2-step deposition on Al$_2$O$_3$. A commercial (Sigma Aldrich) alumina nanoparticles dispersion (20 wt% in IPA) is spin-coated at 2000 rpm to form a $\approx 1\mu m$ thick mesoporous layer, dried at $150°C$ for 45 minutes. A solution of PbI_2 in DMF (462 mg/ml) was spin-coated on the substrates at 2000 rpm under nitrogen atmosphere. Samples were annealed on the hot plate for 30 min at $70°C$. Subsequently they were dipped in a solution of MAI in IPA [0.063 M] for 2 minutes at room temperature. Samples are finally rinsed in anhydrous IPA to remove the excess MAI salt.

2-step deposition of MAPbI$_3$-s. The PbI_2 thin film was then dipped in a hot ($90°C$) 5 mg/ml concentrated MAI isopropanol solution. The dipping time was 2 minutes. The sample was finally rinsed in anhydrous isopropanol in order to remove the non-reacted organic precursor.

2.2.2 MAPbBr$_3$

The $CH_3NH_3PbBr_3$ ($MAPbBr_3$) sample we employed a one-step deposition method. Both the precursors CH_3NH_3Br salt and $PbBr_2$ were dissolved in DMF (concentration of 20 wt%). The obtained solution was spin-coated on a cleaned glass substrate at 3000 round per minute for 60 s. Subsequently we annealed the sample at 100 $°C$ for 15 min in order to obtain the perovskite thin film.

2.3 Scanning Electron Microscopy

Scanning electron microscopy (SEM) pictures have been collected using an high vacuum tungsten filament commercial Jeol 6010-LV, with a working bias of 20 kV.

2.4 Low temperature spectroscopic measurements

Some of the spectroscopic experiments described in the following were performed under controlled atmosphere and temperature. In order to do so we employed a continuous flow static exchange gas cryostat (Oxford Instruments). The cryostat consists of three chambers, one inside the other. The sample is housed inside the internal chamber filled with the cryogenic gas (either He or N_2). The cryogenic liquid is fluxed inside the second chamber allowing temperature control of the inner chamber atmosphere temperature. Eventually a third chamber is evacuated ($\approx 10^{-5} - 10^{-6} mbar$) in order to assure thermal isolation from the external ambient.

2.5 Absorption

Absorption measurements were performed using a spectrophotometer (Perkin Elmer Lambda 1050).

In order to evaluate the average light penetration depth we also measured the Uv-Vis absorption coupling an integrating sphere module to the spectrophotometer, thus allowing the collection of both the total transmittance (T%) and total reflectance (R%). The Optical Density was evaluated according to Lambert-Beer's equation:

$$I_T = (I_0 - I_R)\, 10^{-OD \cdot d} \tag{2.1}$$

where I_T, I_0 and I_R are the transmitted, impinging and reflected light respectively, while d is the sample thickness. This was usually evaluated through a cross-section SEM image. The penetration depth α^{-1} is then defined as the inverse of the absorption coefficient $\alpha(\lambda)$ at the chosen wavelength, estimated inverting the previous equation:

$$\alpha(\lambda)^{-1} = -log\left(\frac{I_T(\lambda)}{I_0(\lambda) - I_R(\lambda)}\right) \tag{2.2}$$

2.6 Steady state Photoluminescence

The steady-state photoluminescence (ss-PL) measurements were performed using a femtosecond laser source. The femtosecond system is driven by a mode-locked Ti:Sapphire oscillator (Coherent Micra-18) operating at 80 MHz. This was used as a fundamental broadband source providing pulses with $\approx 20 fs$ duration and a central wavelength of 800 nm. A grating based pulse stretcher (Coherent 9040) was used to temporally expand the pulses before amplification in a 250 kHz actively Q-switched Ti:Sapphire based regenerative amplifier (Coherent RegA 9000).

The amplified pulses were subsequently temporally compressed in a grating based compressor (Coherent 9040), resulting in pulses with temporal widths of $\approx 35fs$ and energies of $\approx 6\mu J$. The amplified output is sent into a two-pass BBO-based collinear OPA (Coherent 9450), allowing spectral conversion to any desired wavelength in the 400-750 nm wavelength range with resulting temporal broadening to $\approx 120fs$. Depending on the specific experiments here, the system was tuned either to 400 nm (for $MAPbBr_3$) or 700 nm (for $MAPbI_3$) and then focused onto the sample.

In order to give a rough estimation of the initial excitation density n_0 we presumed that the all the photons contained in each pulse N_p are absorbed within a volume given by the spot diameter on the sample times the penetration depth of the monochromatic light at the pumping wavelength. The number of photons per pulse as a function of the measured power (average value) is evaluated according to:

$$N_p(P_{cw}) = \frac{P_{cw}}{RR \cdot E_\gamma} = \frac{P_{cw} \cdot \lambda_\gamma}{RR \cdot hc} \tag{2.3}$$

where P_{cw} is the incident power, RR is the laser repetition rate and E_γ is the Energy per photon. Once the penetration depth $\alpha(\lambda)^{-1}$ is evaluated according to the aforementioned procedure, the number of photon absorbed per unit volume is approximated with the following expression:

$$n_0(P_{cw}) = \frac{N_p}{A_p \cdot \alpha(\lambda)^{-1}} = \frac{P_{cw} \cdot \lambda_\gamma}{RR \cdot hc \cdot A_p \cdot \alpha(\lambda)^{-1}} \tag{2.4}$$

where A_p is the spot area on the sample.

2.6.1 Time-Integrated PL and relative quantum yield

In the case of time-integrated and relative quantum yield measurements, the sample photoluminescence was collected through a doublet of 2-inch lenses and focused onto the entrance slit of a spectrometer (Andor SR-303i-B) coupled to an intensified CCD (Andor iStar DH320T-25U-73). This furnished a spectrally resolved PL spectra for each pumping laser intensity. Integrating the spectra we obtained the overall PL counts per second $\Phi(CPS)$ as a function of the impinging laser fluence F. Eventually the relative photoluminescence quantum yield was evaluated as:

$$Relative - QY = \frac{\Phi(CPS)}{F(\mu J/cm^2)} \tag{2.5}$$

2.6.2 Optical gain

The optical gain measurements were performed focusing the excitation beam onto the sample in a stripe shape using a 100 mm focal length cylindrical lens. A knife blade was placed immediately in front of the sample partially blocking the impinging beam in order to control the excitation stripe length. The emission guided out of the side of the sample was collected by a system of lenses and focused on the

spectrometer. Moving the knife edge in a controlled way through a micrometer translation stage, we measured the emission spectra as a function of the excitation stripe length. These spectra were then integrated over the wavelength to obtain the total emission counts versus stripe length.

2.7 Time resolved Photoluminescence (tr-PL)

Time-resolved fluorescence measurements were performed using a femto-second laser source and either a TCSPC detection system or a streak camera detection system (Hamamatsu C5680). An unamplified Ti:Sapphire laser (Coherent Chameleon Ultra II) operating at 80 MHz was tuned to provide pulses with central wavelengths of 700 nm, energies of $\approx 50nJ$, and temporal and spectral bandwidths of $\approx 140fs$ and $\approx 5nm$, respectively. The emitted fluorescence radiation was collected, filtered with a long pass filter in order to remove the excitation scattering. The cutting wavelength was chosen among 495 nm, 700 nm and 750 nm, accordingly to the excitation/emission wavelength. The filtered emission was subsequently focused on a spectrometer coupled to the detection system. Both the strek camera measurements, done using a linear voltage sweep module, and the TCSPC measurements were performed with < 2 MHz repetition rate excitation, achieved through the use of an acousto-optical modulating pulse picker (APE Pulse Select).

2.7.1 Spatially resolved tr-PL

In this case the sample was excited thanks to a home-built microscope working in reflection geometry; the excitation wavelength was 700 nm. For these measurements the microscope was equipped with a dichroic mirror 700 nm long pass (Semrock) and an objective providing 100x magnification (Zeiss) granting a laser spot diameter of roughly $0.7 - 1\mu m$. The signal coming from the sample was cleaned from the pump wavelength thanks to a long pass filter (Thorlabs) and then sent to a spectrometer coupled to a Streak Camera based detection system as described above.

2.8 Excitation cross-correlation photoluminescece

In the photoluminescence excitation cross-correlation (PEC) experiment a 400 nm pulsed laser source with 250 kHz repetition rate is split into two separate beams with a 50% beam splitter. While one of the beam is directly focused onto the sample, the other one is delayed with an electronically controlled delay-stage and subsequently focused onto the the same spot on the sample (see figure 2.2). Notice that both the beams are chopped using the same optical chopper wheel which is, however, characterized by two different blades steps as shown in figure 2.2. The two beams are arranged in order to go through either the external or the internal wheel, resulting to be modulated with two different frequencies ω_1 and ω_1 respectively. Eventually we focused the two beams onto the sample using the same 2 inches 100 mm focal spherical lens.
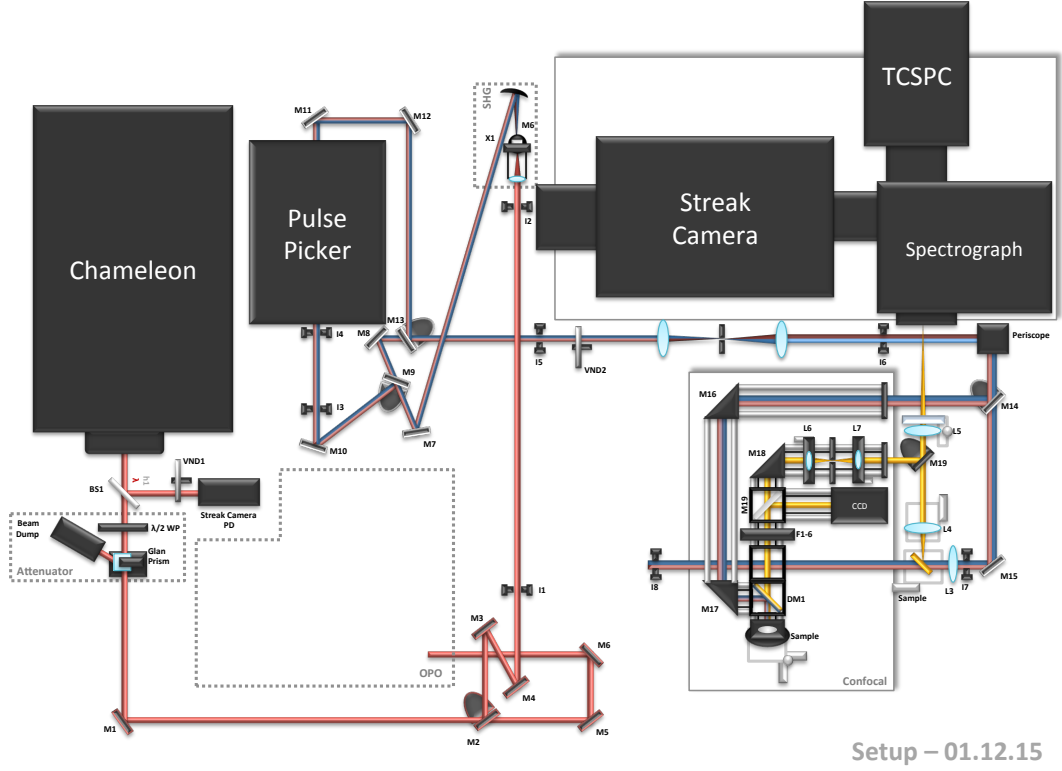
Figure 2.1: *Time-resolved Photoluminescence optical scheme.*

The photoluminescence is collected and focused onto a slow photodiode with a doublet of lenses, after being filtered with a low-pass filter (FEL 435 nm) used in order to remove the pump laser scattering. The photodiode signal is then feed to a lock-in amplifier phase-locked either to the sum or difference frequency $\omega_1 \pm \omega_2$, which is feed to the lock-in by the optical chopper controller.

Suppose that the photoluminescence contain at least a quadratic dependence on the excited state population density $n(t)$. Then when only one train of pulses is present one will have that:

$$I_{PL}^{(2)}(t) \propto n(t)^2 \qquad (2.6)$$

In case both the beams are present, one will have an excited state population density $n(t)$ related to the first incoming pulse, and a $n(t-\tau)$ due to the τ delayed pulse. The resulting quadratic PL contribution:

$$I_{PL}^{(2)}(t,\tau) \propto [n(t) + n(t-\tau)]^2 \qquad (2.7)$$

Collecting the PL signal with a slow photodiode, we should consider the time integral of equation 2.7:

$$I_{PD}(\tau) \propto \int_{-\infty}^{+\infty} [n(t) + n(t-\tau)]^2 dt = \int_{-\infty}^{+\infty} n(t)^2 dt + \int_{-\infty}^{+\infty} n(t-\tau)^2 dt +$$

$$\int_{-\infty}^{+\infty} 2\, n(t)\, n(t-\tau) dt = G_1 + G_2 + G_\chi(\tau) \quad (2.8)$$

where $G_{1,2}$ is the temporal excitation correlation of the two isolated beams and is a signal modulated at either ω_1 or ω_2, while $G_\chi(\tau)$ is the cross-correlation signal resulting specifically from the non linear nature of the luminescence and it is modulated at at $\omega_1 \pm \omega_2$ which we can isolate employing the aforementioned phased-lock detection. For this reason the PEC signal is usually referred to as the difference between the PL signal when both the exciting pulses are present $I_{PL}^{(2)}$ and twice the value of the one pulse PL $I_{PL}^{(1)}$ as a function of the delay τ between the pulses. In order to plot the relative PL variation we normalized this difference to the overall PL signal, thus having:

$$PEC = \frac{(I_{PL}^{(2)} - 2\, I_{PL}^{(1)})}{2\, I_{PL}^{(1)}} \cdot 100 = \frac{\Delta PL}{PL}(\%) \quad (2.9)$$
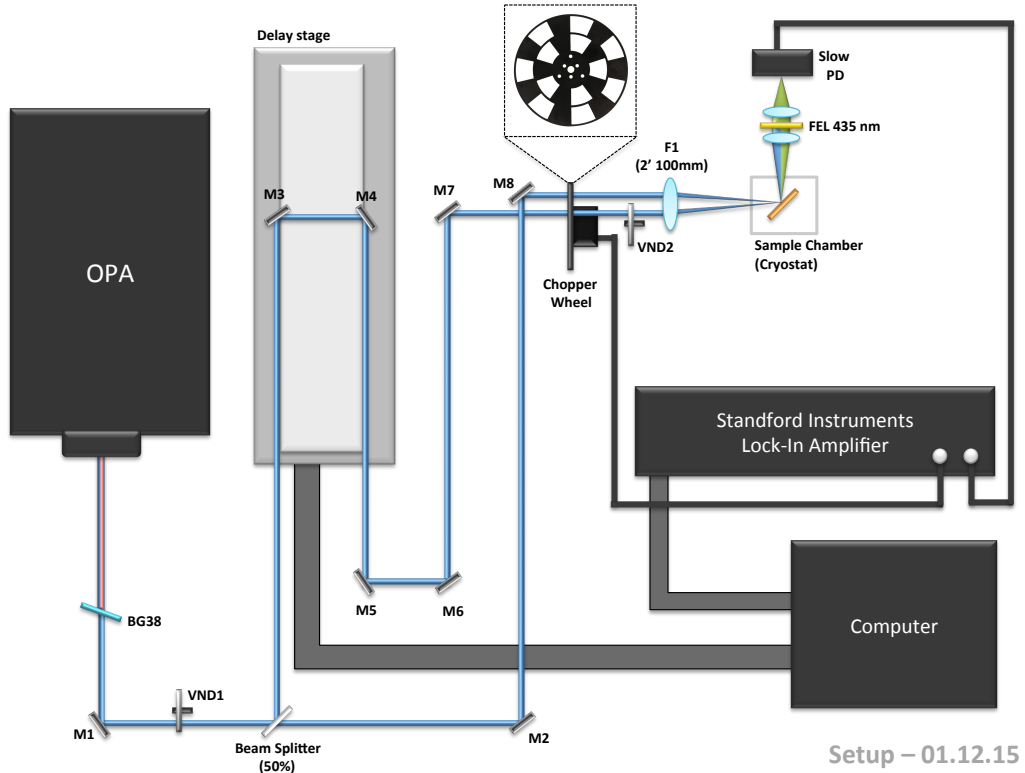
Figure 2.2: *Excitation cross-correlation photoluminescence optical scheme.*

CHAPTER 3

Absorption

3.1 Introduction

One of the main reason accounting for the outstanding performance of hybrid perovskite based solar cells is the strong optical absorption. Good light harvesting properties already with 500 nm thick films, enables the optimization of light absorption with very thin active phase films, thus ensuring a good charge collection efficiency at the device electrodes due to the reduction in the solar cell's series resistance.[68] In this chapter we will discuss the absorption properties of both methylammonium lead-iodide and methylammonium lead-bromide, with an attention on the strong temperature dependence of the absorption coefficient (section 3.2) and role of Coulomb correlations. In section 3.3 we furnish an analytical treatment of the exciton-free carrier ratio that is established under light illumination at the the thermal equilibrium, and eventually in section 3.4 we shed light on the complex influence of the material micro-structure on the perovskite light absorption.

In figure 3.1 we report the UV-Vis absorption measurement of both $MAPbI_3$ (figure 3.1.(a)) and $MAPbBr_3$ (figure 3.1 (b)) in logarithmic scale. As already mentioned in section 1.2.4 the absorption coefficient of hybrid lead-halide perovskite is well described by equation 1.30 through 3D semiconductor Elliot's theory.[62] Inhomogeneous thermal broadening of the optical transitions are taken into account through the convolution of the broadening-free absorption coefficient $\alpha_{T=0K}$ with an hyperbolic secant of with Γ. The fitting function results to be:
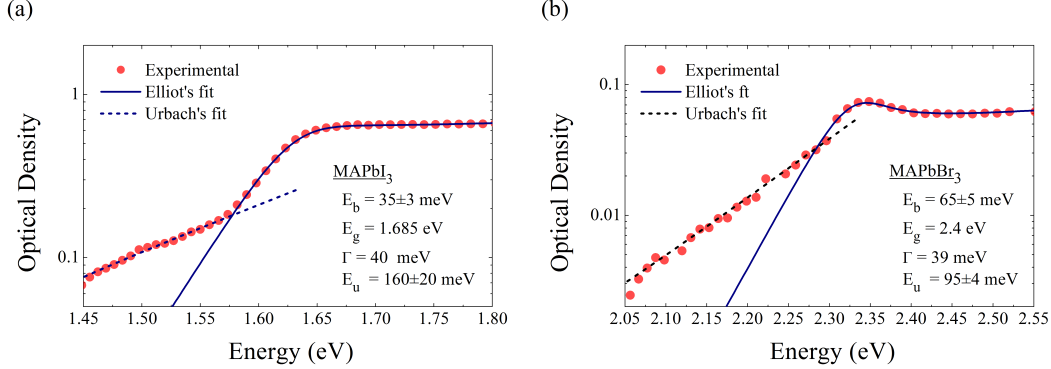
Figure 3.1: *Optical density of both (a) $MAPbI_3$ and (b) $MAPbBr_3$ plotted in log-scale. The solid and dashed blue lines represent the fit according to Elliot's (eq. 3.1) and Urbach's (eq. 3.2) functions respectively.*

$$\alpha(\hbar\omega) = \alpha_{T=0K} * Sech\left(\frac{\hbar\omega}{\Gamma}\right) = \alpha_0^{3D}\left[\sum_{n=1}^{\infty}\frac{4\pi E_b^{3/2}}{n^3}\cdot Sech\left(\frac{\hbar\omega - E_G - \frac{E_b}{n^2}}{\Gamma}\right) + \right.$$

$$\left.\int_{E_g}^{\infty}Sech\left(\frac{\hbar\omega - \varepsilon}{\Gamma}\right)\cdot\frac{2\pi\sqrt{E_b}}{1 - e^{-2\pi\sqrt{\frac{E_b}{h\nu - E_G}}}}\cdot\frac{1}{1 - \frac{8m_r b}{h^3}(\varepsilon - E_g)}\,d\varepsilon\right] \quad (3.1)$$

Notice that this expression contains a slightly different continuous absorption term with respect to the one reported in equation 1.30. This is due to the fact that here we are also considering the non-parabolic correction to the joint density of state. The coefficient b quantifies the deviation of the electronic band structure from the parabolic approximation. In the case of the reported data the factor $\frac{8m_r b}{h^3}$ assumes positive values, thus accounting for a super-parabolic band structure.

Comparing I-based and Br-based perovskite in figure 3.1 (a) and (b) respectively, besides the expected shift of the optical band gap towards higher energies, the most striking observation is the relevant change in the excitonic transition strength, as testified by the clear bump at the absorption band-edge ($\approx 2.32eV$) observable in figure 3.1(b). In figure we report the parameters obtained from the fitting of expression 3.1 (blue line) to the experimental data. Comparing the two samples we can see that the exciton binding energy is almost doubled going from $35meV$ in the case of $MAPbI_3$ to $65meV$ in the case of $MAPbBr_3$, possibly suggesting the stabilization of the excitonic population even at room temperature (see also section 3.3). As we will discuss in more detail later (see section 3.4), the morphology (perceived as the relative degree of poly-crystallinity) of the material is known to have a major influence on the optical properties of the material. For this reason it's fair to notice that, in order to disentangle the intrinsic differences induces by the halide substitution and the ones possibly induced by the morphology, the samples investigated here were grown in similar way, showing a comparable average crystallite size ($\approx 1\mu m$), It's important to highlight that according to the reported fitting parameters in both cases the thermal broadening

is comparable to the exciton binding energy. Recalling that the excitonic resonance is related to the exciton dephasing time (ref also to section 3.2.3), such a large broadening rises doubts on the real possibility of creating a stable excitonic population.

It's worth noticing that in both the considered cases Elliott's model fails to match the experimental data below the band-gap due to a non negligible absorption in that spectral region. We observe that in a log scale the sub-band gap absorption appears as a straight line, thus suggesting that the divergence between the experiment and the theoretical model can be corrected adding an exponential sub-band gap absorption term given by:

$$\alpha_u \propto exp(\frac{(h\nu - E_g)}{E_u})$$ (3.2)

where E_g is the optical band-gap and E_u is refered to as the Urbach energy. This empirical law was first proposed by Urbach in 1953[69] that employed it to describe alkali halides absorption. More recent works[70,71] demonstrated that this law describe effectively very general systems. In particular they showed that a random distribution of impurities in a semiconductor can introduce spatial fluctuation in the lattice potential allowing the presence of some spatially localized energy levels within the forbidden region of the energy gap. These are usually modeled as an exponential tail of the conduction band density of states and is referred to as *Urbach tail*. In the presented case these tails can be attributed both to the excitonic level or to local defects induced trap states. The dashed blue lines in figure 3.1(a) and (b) represent the fitting of equation 3.2 to the sub-bandgap absorption data, the corresponding Urbach energies are also reported in figure. We notice that in both cases the Urbach energy is quite big with respect to the exciton energy, thus making it difficult to understand weather the sub-bandgap absorption is related to an high trap states density or to an excitonic level energetic distribution.

3.2 Temperature dependence of absorption coefficient

In figure 3.2 we report the optical density of both $MAPbI_3$ and $MAPbBr_3$ at variable temperatures between 290 K and 77 K. Focusing on the iodide based perovskite (figure 3.2(a)) we see that lowering the temperature down to 170 K the absorption band-edge slowly shifts towards lower energy (red-shift). However if the temperature is reduced further an abrupt shift to higher energies (blue-shift) is observed, together with the enhancement of the excitonic absorption bump. Eventually at 77 K we observe again a red-shift and the excitonic peak becomes more prominent. Turning now to the bromide perovskite (figure 3.2(b)) while we still observe the continuous band-edge red-shift and excitonic absorption enhancement, no aburpt change is detected in the whole temperature range investigated.

The reported observations highlight the fact that we have several phenomena contributing to the modification of the optical edge upon the temperature reduction. In the following we try to disentangle each of this phenomena and their different temperature dependencies. Firstly we discuss the red-shift of the band edge (subsection 3.2.1), this is a phenomenon referred to as *Varshni Shift* and

it's related mainly to the temperature induced lattice strain. Subsequently in subsection 3.2.2 we discuss the effect of the crystalline symmetry phase transition on the absorption spectrum, thus explaining the abrupt blue-shift observed only in $MAPbI_3$. Lastly we deal with the temperature related excitonic effect, dealing with a general theory for excitonic resonance thermal broadening (subsections 3.2.3.

(a)

(b)
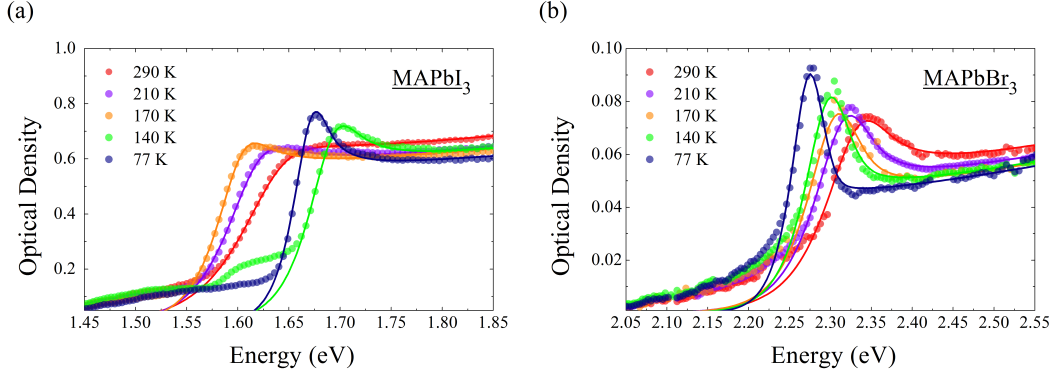
Figure 3.2: *Optical density of both (a) $MAPbI_3$ and (b) $MAPbBr_3$ together with the curves obtained fitting the elliot's expression to the experimental data at 290K (red dots), 210 K (purple dots), 170 K (orange dots), 140 K (green dots)and 77 K (blue dots).*

3.2.1   Varshni Shift

For all semiconductors the energy gap value is a temperature dependent quantity.[53] There are two main reason for this dependence: (a) the thermal expansion of the lattice, altering the periodic potential experienced by the electrons and thus the band structure and E_G, (b) the effects of lattice vibration, that we will debate in more detail in section 3.2.3.

The combination of these effects lead the energy gap (Eg) dependence on temperature to follow the empirical Varshni law:[72]

$$E_G(T) = E_0 - \alpha \frac{T^2}{T + \beta} \qquad (3.3)$$

where E_0 represents the material energy gap at T = 0, while α and β are constant parameters characteristic of a given material. For most of semiconductors (e.g. GaAs, Si) the gap shifts to lower energies with increasing temperature ($dE_G/dT < 0$), however Pb-based bulk semiconductors have an opposite behavior[53] since the lattice dilation contributes increasing the band gap energy with temperature ($dE_G/dT > 0$).[73]

Hybrid perovskite are usually characterized by an excitonic transition in absorption (ref to section 1.2.4), thus making it difficult to properly evaluate the E_G value from a simple UV-Vis absorption measurement. For this reason in order to evaluate the energy gap temperature dependence for this materials an effective approach is to monitor the edge of the absorption in a high temperature regime where the excitonic transition should not play a role (ref to sec

3.2.3). In this region equation 3.3 can be approximated by a linear function of T ($E_G(T) \simeq E_0 + \frac{dE_G}{dT}T$). In figure 3.3 we report the model case of a Cl doped lead-iodide perovskite $CH_3NH_3PbI_3$. In figure 3.3(b) the band edge (taken as the energy at which the first derivative of the absorption spectra is maximum) versus T is reported, a linear fit of this data allows us to extrapolate a $dE_G/dT \simeq 262\mu eV/K$.
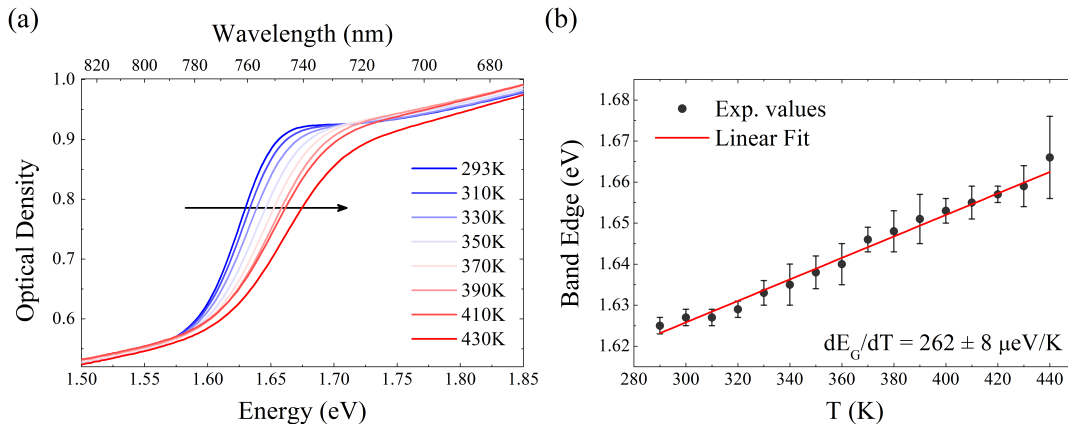
Figure 3.3: *(a) Absorption spectra of Cl doped $CH_3NH_3PbI_3$ deposited on a glass substrate vs temperature (290 K - 440 K). (b) Plot of the band edge vs T. The experimental data are fitted according to the linear approximation of equation 3.3 furnishing $dE_G/dT = 262 \pm 8\mu eV/K$.*

3.2.2 Phase transition

As we mentioned in section 1.1 hybrid lead-halide perovskites in some cases can be characterize by a drastic change in the crystalline symmetry of the unit cell upon temperature variation, thus affecting the optical absorption of the material, however that's not always the case. XRD measurements reported in literatures[18,27,28] show that both the iodide and bromide perovskite undergoes two phase transitions between 77 and 400 K, however, as we discuss in the following, these transitions don't always reveals themselves as a drastic change of the absorption spectra.

In figure 3.4 the energy gap of $MAPbI_3$ and $MAPbBr_3$ samples are reported as a function of the temperature at which the absorption measurement is performed. In both cases we observe a linear shift of the semiconductor band-gap towards higher energies upon temperature increase which we ascribe to the aforementioned Varshni shift. While in the bromide case we do not observe any other relevant change beyond this shift (figure 3.4 top panel), in the iodide case the phase transition between the tetragonal and orthorombic crystalline phases happening at 167 K[27] induces an abrupt change of the energy gap going from 1.635 eV at 170 K to 1.727 at 140 K (figure 3.4 bottom panel).

Surprisingly we do not observe any relevant change of the energy gap around 327 K, temperature corresponding to the tetragonal to cubic crystalline phase transition. This anomaly was studied by Quarti and coworkers.[74] Trough Car-Pariniello molecular dynamics simulations they demonstrated that even if on average the high temperature phase corresponds to the cubic structure expected from XRD measurements, the system deviates from the cubic structure in the
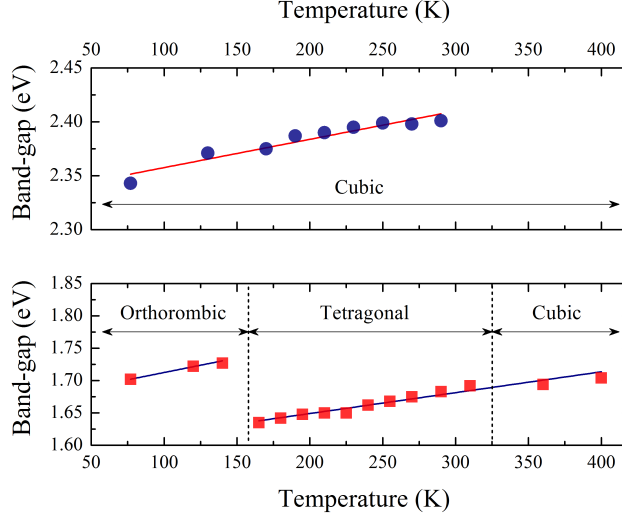
Figure 3.4: *Energy Band-gap of the $MAPbBr_3$ (top panel) evaluated between 77 K and 290 K and of $MAPbI_3$ (bottom panel) evaluated between 77 K and 400 K. The reported values are obtained as fitting parameter of the Elliot's expression for the absorption coefficient (eq. 3.1) to the UV-Vis absorption data.*

sub-picosecond time scale. For this reason on the time scale of electronic transitions the material seldom experiences a cubic environment, rather an increasingly distorted tetragonal one. As a consequence, increasing the temperature beyond 327 K, the optical absorption of the material do not show any dramatic change beyond the usual Varshni shift. It's worth noticing that this peculiar behavior is very important for the feasible application of perovskite solar cell, since it guarantees a stable optical absorption in a vast temperature range which is experienced by the solar cell under working conditions.

3.2.3 Exciton line-broadening

As already discussed the UV-Vis measurements of lead-halide perovskite are characterized by an excitonic transition at the absorption-edge. Modeling the experimental data with equation 3.1 we obtain a transition line broadening Γ of approximately $40 meV$ for both the investigated samples. We notice that this value is roughly comparable to the exciton binding energy of lead-iodide perovskite and slightly smaller than the one of lead-bromide one. Thus a deeper understanding of the physics governing the transition broadening appears to be of paramount importance in order to understand the excitonic population stabilization dynamics.

The excitonic resonance spectral line-width is determined by the mechanism ruling the interaction of the excited electronic state with the lattice vibrations, the so called *exciton-phonon* coupling. In order to roughly quantify this interaction we consider a one-dimensional lattice with two different ions per unit cell, which is the simplest model that can represent the basic vibrational features of a 3D crystal.[53, 75]

Considering for simplicity only nearest neighbor interaction, the potential de-

scribing the ion movement within harmonic approximation will be:

$$U_{harm} = \frac{K}{2}\sum_n [x_1(na) - x_2(na)]^2 + \frac{K}{2}\sum_n [x_2(na) - x_1([n+1]a)]^2 \qquad (3.4)$$

where $x_1(na)$ and $x_2(na)$ are respectively the displacement of the ions about site na (site of ion 1) and na+d (site of ion 2), while K and G are the two different spring constant related to the 1-2 and 2-1 bound (K > G since d < a). The motion equation will be a set of coupled equations:

$$M\ddot{x}_1(na) = -\frac{\partial U_{harm}}{\partial x_1(na)}$$
$$M\ddot{x}_2(na) = -\frac{\partial U_{harm}}{\partial x_2(na)} \qquad (3.5)$$

Being within the harmonic approximation one will seek for plane wave solution, i.e. $x_{1,2}(na) = \epsilon_{1,2}e^{i(kna-\omega t)}$. Moreover one can show that the pair of coupled equation will have solution only if $\omega(k)$ satisfy a determined relation. In particular for each value of k $\omega(k)$ will assume two values, thus defining two distinct *dispersion relations* which are referred to as the *acoustic* branch, which present a linear dispersion at small k: $\omega(k) = ck$ and the *optical* branch, which on the other hand assume a non zero value for k = 0 (see figure 3.5(a)).

(a) (b)
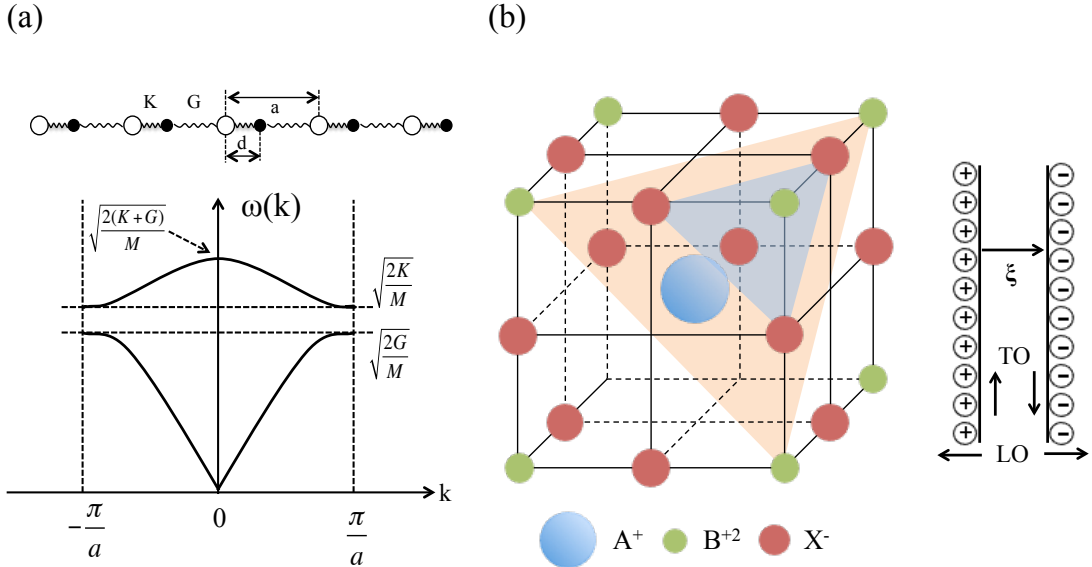
Figure 3.5: *(a) Sketch of the 1-D infinite chain with two ions per unit cell and the resulting dispersion relations for optical and acoustic phonons. (b) Perovskite cubic structure. The blue plain is defined by negative X^- ions while the orange one is defined by positive B^{2+} ions, generating a local capacitor.*

Up to now we considered only oscillation along the chain, the *longitudinal vibration modes*, however there are also oscillation perpendicular to the chain, the

transverse vibration mode. Notably when going to a real 3D lattice, with n atoms per unit cell, the picture is qualitative the same resulting in 3 acoustic modes and $3n$-3 optical modes.

Due to the quantized nature of matter the interaction of the exciton with the lattice vibration modes will be mediated by quasi-particles called *phonons* which represent quanta of vibrational energy of a solid. Each phonon has energy $\hbar\omega(k)$ and obey the Bose-Einstein statistic, thus the phonon distribution function is given by:

$$n_k = \frac{1}{e^{\hbar\omega(k)/kT} - 1} \tag{3.6}$$

Frölich broadening mechanism

Among the different mechanisms governing the exciton-phonon interaction Frölich mechanism is by far the most relevant in ionic crystals such as hybrid perovskite.[75] The physical principle underlying this process consists in the Coulomb interaction between the e-h pairs and a local electric field $\boldsymbol{\xi}$ generated by the lattice vibration. In fact within the perovskite crystal lattice the metal cation (B^{2+}) and the halide anion (X^-) lie on alternate planes acting as a capacitor plates, thus LO phonons (with $\mathbf{k}$ vector orthogonal to such planes) will give rise to a vibrating capacitor with constant charge density but oscillating plate separation inducing a local oscillating electric field whose amplitude will increase with T (figure 3.5(b)). Notice that TO modes won't contribute due to their relative orientation.

The quantitative characterization of this exciton-phonon coupling is not easy, however, in virtue of the above discussion, for 3D ionic semiconductor the degree of broadening is usually taken to be related only to the LO phonon absorption and thus to be proportional to their density $n_{LO}(\hbar\omega_{LO})$ furnished by equation 3.6.

In summary the exciton line broadening Γ is effectively described with the following:[76,77]

$$\Gamma = \Gamma_0 + \frac{\Gamma_B}{e^{\hbar\omega_{LO}/kT} - 1} \tag{3.7}$$

where Γ_0 is an inhomogeneous broadening parameter, which is T independent, while Γ_B is the exciton-phonon coupling parameter.

Exciton binding Energy from T dependence

Notably the above mentioned temperature dependent line-broadening can be employed as a useful tool in order to estimate an upper limit for the exciton binding energy, as reported in our recent work[60] where we considered the case of $CH_3NH_3PbI_{3-x}Cl_x$ perovskite.

As mentioned above the disorder induced inhomogeneous broadening is usually temperature independent, thus in our work we modeled the exciton line-width taking into account only the homogeneous broadening whose formalism we borrowed from a simple the two-level system[63] in which the linewidth of the transition resonance is $\Delta\nu = 1/\pi T_2$, where T_2 is the excited state coherence lifetime. This value

can be affected both by the natural population decay of the excited state population (with time T_1) and by elastic scattering events (with rate γ) that contribute to the line broadening but do not change the excited state population density, according to the following equation:

$$\frac{1}{T_2} = \frac{1}{2T_1} + \gamma \tag{3.8}$$

For most ionic semiconductors at high temperatures (e.g. T > 100 K), exciton-phonon coupling leads predominantly to exciton ionization.[63,78] Thus in the hybrid perosvkite case the T_1 decay will be the sum of an *intrinsic* decay rate (k_0) and thermal dissociation rate (k_T)[63] $\frac{1}{T_1} = k_0 + k_T$, where in first approximation we can model the (k_T) with an Arrhenius like law:

$$k_T = \nu_T e^{-\varepsilon_B/kT} \tag{3.9}$$

where ε_B is our upper estimate for the exciton binding energy, k is the Boltzmann constant and ν_T is the ionization attempt frequency. Plugging-in the relationship 3.8 in the linewidth, $\Delta\nu = 1/\pi T_2$ we obtain:

$$\Delta\nu = \Delta\nu_0 + \nu_T e^{-\varepsilon_B/kT} \tag{3.10}$$

where $\Delta\nu_0$ accounts for the temperature-independent broadening. In figure 3.6 we reported the natural logarithm only of the T dependent part of the experimental exciton line-width ($ln(h\nu - h\nu_0)$) collected as reported in reference[60] as a function of 1/T together with the linear fitting $ln(h\nu_T) - \varepsilon_B/kT$.

Notice that the T span is between 150 K and 290 K, since a structural phase transition (from tetragonal to orthorombic crystalline unite) occurs below 150 K in lead-iodine based perovskite.[27,60] Through the fitting we obtain an upper estimate for the exciton binding energy of 55 ± 20 meV.

Notice that for $\hbar\omega_{LO} >> kT$ equation 3.7 resembles the formulation of equation 3.10. This observation is telling us that the ionization phenomenon, mediated by LO phonons, is involving phonon of energy ε_B. Thus we can safely say that the real binding energy of our system will be $E_B < \varepsilon_B$.

3.3 Steady state exciton population: Saha equation

The inelastic exciton-phonon interaction possibly leading to the bound state ionization is not the only process to take into account. Depending on the electron-hole pair density the probability of forming an excited bound state via coulomb interaction becomes a competing process with respect to the ionization, thus giving rise to a dynamic equilibrium between the e-h plasma n_{eh} and the excitons n_{exc}, eventually leading to a thermal equilibrium between the two species. It's important to notice that in general, due to many-body effects such as phase-space filling and exchange energy, the exciton binding energy E_B is a quantity that depend on the overall excited state population density ($n = n_{exc} + n_{eh}$) within the semiconductor.[79] However this *binding energy renormalization* is usually relevant

Figure 3.6: *Plot of the exciton absorption band broadening $\Delta\nu_0$ in $CH_3NH_3PbI_{3-x}Cl_x$ thin film vs inverse temperature (150 K < T < 290K). The error bar indicates the maximum variation of the experimental value due to the $\pm10K$ uncertainty in the determination of the sample temperature. The solid line is the fit realized according to $ln(h\nu_T) - \varepsilon_B/kT$. Parameters: $\varepsilon_B = (55 \pm 20)meV, \nu_T = (7fs)^{-1}.\chi^2 = 0.92$.*

only in quantum confined system, thus we can safely discard it in the following discussion. Within this approximation the thermal equilibrium established between exciton and e-h plasma is successfully described by the Saha-Langmuir equation.[79,80] This equation was proposed for the first time in 1921 to described the equilibrium between the neutral and ionized state of the hydrogen, in the following we report a simple derivation of this relation in a more general case in order to give a relationship between the ground and the ionized stated of a given system.

Let's treat the system as an ideal gas of N_e electrons, N_h holes and N_{exc} excitons which we will consider as indistinguishable particles. Since the total number of particles is conserved the overall system will be a *canonical ensemble* and the partition function for each class of particle λ within the *Maxwell-Boltzmann approximation* is given by:[81]

$$Z_\lambda = \frac{1}{N_\lambda!} z_\lambda^{N_\lambda} \tag{3.11}$$

where z_λ is the single particle partition function for the λ particle class, defined as:

$$z_\lambda = \sum_l e^{-\varepsilon_l/k_B T} \tag{3.12}$$

where ε_l is the energy in a given state l $= \mathbf{k}$, m_s of wavevector $\mathbf{k}$ and spin s. In the case of free particles the energies will be spin independent and given by $\varepsilon_l = \hbar^2 k^2/2m_\lambda$. In a bulk semiconductor the energy states, despite being discrete, are closely spaced with density $V/(2\pi)^3$, being V the volume of the semiconductor

37

(c.f. section 1.2.1). As a consequence the single particle partition function can be approximated with an integral over the k-space:

$$z_\lambda = \sum_{m_s=-s}^{s} \frac{V}{(2\pi)^3} \int e^{-\frac{\hbar^2 k^2/2m_\lambda}{k_B T}} dk^3 \qquad (3.13)$$

The sum over the spin states m_s will be given by 2s+1 equal terms, thus the expression can be readily simplified in:

$$z_\lambda = \frac{(2s+1)V}{2\pi^2} \int_0^\infty e^{-\frac{\hbar^2 k^2/2m_\lambda}{k_B T}} k^2 dk \qquad (3.14)$$

where we also moved to spherical coordinates ($dk^3 = 4\pi k^2 dk$). This integral can be solved via variable substitution, so that if $y = \hbar k/\sqrt{2m_\lambda k_B T}$ the integral becomes $\int_0^\infty y^2 e^{-y^2} dy = \sqrt{\pi}/4$, thus resulting to be:

$$z_\lambda = (2s+1)\frac{V}{\Lambda^3} \qquad (3.15)$$

where Λ is the *thermal wavelength* of a particle of mass m_λ: $\Lambda = h/\sqrt{2\pi m_\lambda k_B T}$.

Notice that in the case of the exciton class the energy of each states needs to be corrected considering its binding energy $\varepsilon_l = \hbar^2 k^2/2m_\lambda + E_B$. Since this correspond simply to a rigid shift of the energy axes, in the case of an excitonic particle class the partition function results $z_{exc} = z_\lambda e^{-E_B/k_B T}$.

Considering now the ensemble of all the three particles class the partition function will be readily given by:

$$Z = Z_e \cdot Z_h \cdot Z_{exc} = \frac{z_e^{N_e}}{N_e!} \cdot \frac{z_h^{N_h}}{N_h!} \cdot \frac{z_{exc}^{N_{exc}}}{N_{exc}!} \qquad (3.16)$$

The corresponding Helmholtz free energy ($F = -k_B T ln(Z)$), exploiting the Stirling approximation ($ln(N!) \approx Nln(N) - N$) results:

$$F = -k_B T[N_e ln(z_e) + N_h ln(z_h) + N_{exc} ln(z_{exc})$$
$$- N_e ln(N_e) + N_e - N_h ln(N_h) + N_h - N_{exc} ln(N_{exc}) + N_{exc}] \qquad (3.17)$$

Since we are considering the simple scenario in which at every time the number of electron equals the number of holes and the overall number of particles is conserved ($N_e + N_h + N_{exc} = const$), we can then reduce the problem to two species which are the number of free eh pairs (N_{eh}) and the number of bound eh pairs, i.e. excitons (N_{exc}). These will satisfy the following:

$$N_e = N_h = N_{eh}$$
$$N_{exc} = N - N_{eh} \qquad (3.18)$$

thus giving:

$$F = -k_B T [N_{eh}(ln(z_e) + ln(z_h)) + (N - N_{eh})ln(z_{exc})$$
$$- 2N_{eh}ln(N_{eh}) + 2N_{eh} - (N - N_{eh})ln(N - N_{eh}) + N - N_{eh}] \quad (3.19)$$

At the thermal equilibrium the Helmholtz free energy is minimized, thus in order to find the equilibrium values of N_{eh} and N_{exc} we can simply solve the equation $\partial F/\partial N_{eh} = 0$:

$$\frac{\partial F}{\partial N_{eh}} = -k_B T[ln(z_e) + ln(z_h) - ln(z_{exc}) - 2ln(N_{eh}) + ln(N - N_{eh})] = 0 \quad (3.20)$$

thus giving the relationship:

$$\frac{z_e z_h}{z_{exc}} = \frac{N_{eh}^2}{N - N_{eh}} \quad (3.21)$$

Now we need simply to plug the expression 3.15 into 3.21. Here it's worth noticing that being the exciton a quasi-particle made of a bound e-h pair, it will have a reduced mass $m_{exc} = (1/m_e + 1/m_h)^{-1})$ and three energetically degenerated states ($2s + 1 = 3$ and $m_s = -1, 0, 1$). Keeping this in mind one will get:

$$\left(\frac{2\pi\mu k_B T}{h^2}\right)^{3/2} e^{-E_B/k_B T} = \frac{n_{eh}^2}{n - n_{eh}} \quad (3.22)$$

where we also introduced the particle densities as $n_\lambda = N_\lambda/V$ and the total exciton mass $\mu = m_e + m_h$. This expression is usualy reported considering the fraction of free e-h pairs over the total particles density $x = n_{eh}/n$. Thus resulting to be:[80]

$$\frac{x^2}{1 - x} = \frac{1}{n}\left(\frac{2\pi\mu kT}{h^2}\right)^{3/2} e^{-E_B/k_B T} \quad (3.23)$$

The shape of this equation is quite intuitive: the higher the temperature the greater e-h plasma ratio due to improved ionization process, but as the excitation density increases the possibility of e-h interaction with subsequent exciton formation prevails and the ratio is reduced.

In the figure 3.7 we report the dependence of the free charges fraction x with respect to the excitation density n varying either the temperature of the overall system at fixed E_B or its binding energy ($E_B = 20meV \div 200meV$) at room temperature. It's interesting to notice that in order to have a consistent fraction of excitons in conventional experimental condition, such as in transient absorption and photoluminescence measurements, ($n = 10^{17} \div 10^{18} cm^{-3}$) relatively high binding energy are needed ($x < 50\%$ for $E_B > 50meV$). Moreover from this simple analysis we can predict that in the case of hybrid perovskites meant for photovoltaic application the exciton will hardly play a role in the photovoltaic conversion process since in the photovoltaic cell operating condition ($n \simeq 10^{16} cm^{-3}$ and RT) the equilibrium established is largely in favor of the e-h plasma.[60]
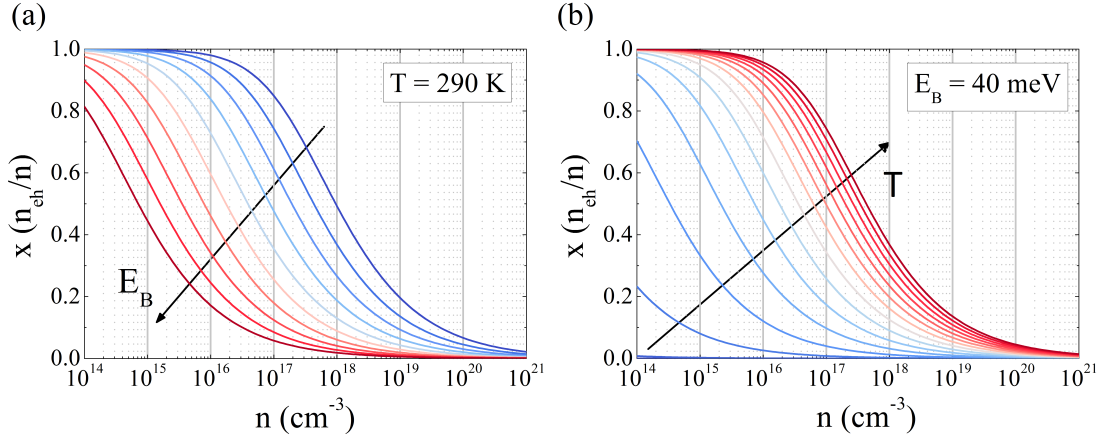
Figure 3.7: *Saha simulations of the fraction of free charge carriers as a function of the total photo-excitation density n: (a) with various binding energies ranging from 20 meV to 200 meV (20 meV steps), at 290 K; (b) over the temperature range 0 K to 290 K with a constant binding energy of 40 meV. The total mass μ for the above simulations was set to 0.2 m_0.*

3.4 The role of micro-structure in the absorption properties

Depending on the processing method, lead-iodide perovskite thin films present a variable mesoscale morphologies with grain size ranging from tens to thousands of nanometers. Notably it has been shown that the obtained morphology affects both the absorption and the luminescence properties[82,83] ultimately driving the device performances.[82,84] In particular it's interesting to notice that for lead-iodide based perovskite there is a wide spread in the exciton binding energy values reported in literature, ranging from 2 to 50 meV.[48,60,85–87] This variability stems only partly from the fact that different techniques have been used to estimate E_B. In fact it's very likely that the major cause for this discrepancy arise from the high variability of local microstructure from sample to sample.

In figure 3.8(a-d) top-view scanning electron microscopy (SEM) images of four representative $MAPbI_3$ samples are reported. These were fabricated using a two-step sequential deposition technique[88,89] dipping a spincoated film of PbI_2 into a CH_3NH_3I (MAI) solution with variable temperature and concentration resulting in an observed average size of the crystallite dimension ranging from $< 250nm$ to $> 2\mu m$. In figure 3.8(e) we reported the UV-Vis absorption spectra of the four reported samples together with the optical band-edge, evaluated as the energy value at which the first derivative of the absorption spectrum is maximized, as a function of the average crystallite size for the whole series of samples investigated. We notice that the optical band-edge experience a continuous shift towards lower energies going from $\approx 1.63eV$ to $\approx 1.60eV$ as the average crystallite size is increased.

Mitzi et al. demonstrated that in 2D tin-based hybrid perovskite one can induce a different relaxation of the halide-metal-halide bonding angle by tuning the organic moieties arrangement,[90] in turn showing that the relaxation plays a fundamental role in the definition of the electronic structure of the material. In accordance with this results, more recently some theoretical studies revealed that
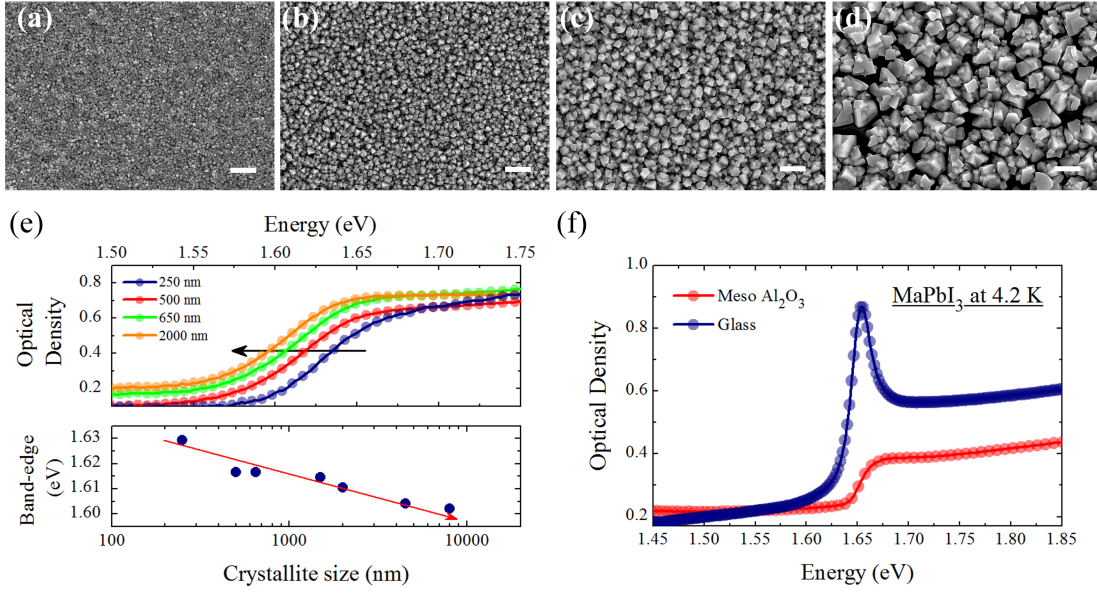
Figure 3.8: *(a-d) Top-view SEM images of $MAPbI_3$ formed using (a) $[MAI] = 0.063M$, $T = 25°C$; (b) $[MAI] = 0.045M$, $T = 25°C$; (c) $[MAI] = 0.031M$, $T = 25°C$; (d) $[MAI] = 0.045M$, $T = 70°C$. Scale bars are 2 μm. (e) UV-Vis absorption spectra of the four samples reported (top) and absorption band-edge as a function of the average crystallite size of the full series (bottom) . (f) UV-Vis absorption spectra of $MAPbI_3$ either spincoated on a flat glass substrate, or infiltrated in a mesoporous $Al_2O_3 scaffold.*

the optical band-gap of $MAPbI_3$ perovskite can be modulated over almost one eV via tuning of the I-Pb-I bond angle, which can be experimentally obtained via organic moiety exchange.[54,55] Thus, we relate the observed shrinkage of the optical band gap in the larger perovskite crystallites to a change in the Pb-I bond stress which is realized with a tuning of the crystallization condition (i.e. temperature and solution concentration). In fact when the crystal grows larger the Pb-I bond stress is relaxed and the absorption band-edge is red-shifted.

A recently pubblished Raman analysis performed by Grancini and co-workers, revealed a stronger distortion in the Pb-I bond in moving from large crystals grown on a flat glass substrate to smaller crystals grown in a mesoporous Al_2O_3 scaffold,[39,91] thus showing that the tuning of the optical properties can be achieved also with a proper choice of the substrate on which the perovskite is deposited. In figure 3.8(f) we report the UV-Vis spectrum collected at 4.2 K of the $MAPbI_3$ perovskite grown either on a flat glass substrate or within a mesoporous Al_2O_3 scaffold. Notably the low temperature spectrum of the perovskite grown on glass not only shows the expected optical band-gap shift induced by the different Pb-I strain relaxation, but is also characterized by a strong excitonic peak which, conversely, is not detected in the perovskite grown within the mesoporous scaffold. The exciton stability dependence on the average crystallite dimension has been thoroughly studied by Petrozza and co-workers.[57] In their work they show that due to the strong contribution of various phonon modes to the effective permittivity, i.e. to electron-hole screening, the variation of the degree of the organic moiety

local order/disorder (and therefore phonon distributions) over different film architectures can result in a tuning of the exciton binding energies. As a consequence the polycristalline disorder of little crystals induces electrostatic potential variation suppressing the exciton formation and stabilization. It's worth noticing that the $MAPbBr_3$ sample reported above, which shows a strong excitonic absorption peak, is grown in 1 μm large crystals, thus confirming the relevance of the microstructure in the definition of perovskite behaviour, with both free carrier and excitonic regimes possible.

Thanks to these observations, we can conclude that the microstructure of the perovskite thin film, related to a different local arrangement of the organic moiety, on the one hand is tuning the Pb-I stress relaxation revealed in Uv-Vis absorption measurements as a shift of the band-gap energy, on the other is also deeply affecting the local electrostatic landscape, thus strongly influencing the electron-hole interactions.

CHAPTER *4*

Photo-luminescence of MAPbI$_3$

4.1 Introduction

As already mentioned in the section 1.1, within the plethora of available hybrid perovskite $MAPbI_3$, is one of the most widely employed material for efficient device fabrication[10, 17, 89, 92, 93] and one of the most studied perovkite,[36, 37, 60, 65, 66, 94] and represents a model case for the description of the fundamental PL properties. In the following we will discuss the photo-luminescence properties in the particular case of a two-step deposited thin film of $MAPbI_3$ perovskite[88] (see section 2.2 for further details on the samples fabrication).

This material is a direct band gap semiconductor characterized by the presence of a weakly bound Wannier-Mott exciton.[49, 60, 65] Due to the low binding energy of the exciton with respect to the LO phonons energy (c.f. section 3.1) at room temperature, and in light of the recent work by Grancini et al.,[57] in the case of iodide based perovskite we will discard the excitonic contribution to the PL.

4.2 A rate equation model for lead-iodide perovskite PL dynamics

Saba and coworkers reported that the integrated PL emission intensity as a function of the pump laser fluence follows a 3/2 power law over more than three orders of magnitude in excitation intensity[65] (see figure 4.2 (a)). This power law testifies that the electron–hole population dynamics result from the competition between a radiative recombination channel and at least one non-radiative path, likely related to a specific intra-gap states acting as traps for electrons or holes.

Following the paradigm of equation 1.33 we consider an intra-gap trap state accounting for an Shockley-Read-Hall (SRH) like recombination path, an Auger non-radiative term and a spontaneous emission which, for simplicity, we take

as bimolecular band to band recombination (c.f.r. 1.42). For exemplification purposes, the sketch in figure 4.1(a) shows an electron trap.

The resulting rate equations for the electrons n_e, holes n_h and filled traps n_t population density will be:

$$\frac{dn_e}{dt} = -\beta_{rad}\, n_e\, n_h - k_t\, n_e\, (N_t - n_t) - \gamma\, n_e\, n_h^2 + R_G$$

$$\frac{dn_h}{dt} = -\beta_{rad}\, n_e\, n_h - G_n\, n_h\, n_t - \gamma\, n_e\, n_h^2 + R_G \qquad (4.1)$$

$$\frac{dn_t}{dt} = k_t\, n_e\, (N_t - n_t) - G_n\, n_h\, n_t$$

where N_t is the density of available trapping sites, G_n is the rate of recombination of a trapped electron with an hole in the valence band and R_G is the photogeneration rate.

4.2.1 Steady-state solution

In figure 4.1(b) the steady-state solutions of the three rate equations ($dn_i/dt = 0$) as a function of the impinging laser fluence $F(\mu J/cm^2)$ is reported. As a consequence of the two competing recombination the solution is characterized by two different regimes.

(a) At low-excitation fluences, trapping is the most efficient recombination path for electrons, thus being $n_t << N_t$ electron trapping is a monomolecular process and n_e will scale linearly with the laser fluence, $n_e \propto F$. However valence band holes trend with fluence is limited by the non-radiative recombination rate with trapped electrons which is a bimolecular process ($\approx n_h\, n_t$), inducing the hole population to scale as the square root of the laser fluence, $n_h \propto \sqrt{F}$. The resulting steady-state PL intensity then reads $PL \propto \beta_{rad}\, n_e\, n_i \propto \beta_{rad}\, F^{3/2}$.

(b) At higher fluences the trapping rate slow down since $n_t \approx N_t$ and the bimolecular radiative recombination of e-h pairs becomes dominant, thus the steady state PL trend changes from superlinear to linear since $n_h\, n_e \propto F$, as shown in figure 4.2(a).

At even higher laser intensities the Auger process are not anymore negligible, resulting in a sublinear trend of the integrated PL and a reduction in PL quantum yield (red dots in figure 4.2(b).

4.2.2 Dynamic solution

The same rate equation can be solved in order to give the dynamic solution and thus fit the PL decays, as shown in figure 4.2(b). For seek of simplicity we removed the generation rate term and simply used as initial state for n_e and n_h the number of absorbed photon,evaluated as:

(a)

(b)
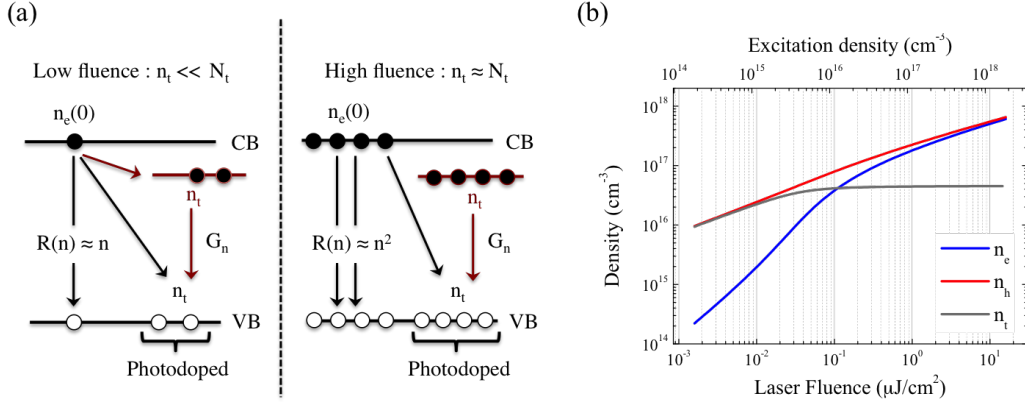
Figure 4.1: *(a) Sketch illustrating the recombination mechanisms for the low- and high-fluence regimes. Figure adapted from references[65, 94] . (b) Electrons (blue), holes (red) and filled traps (grey) population density obtained as the steady state solution of 4.1. As the excitation intensity grows the traps are filled and the bimolecular recombination becomes faster than the trapping rate, therefore preventing the accumulation of trapped electrons.*

$$n_{phot} = \frac{P_{CW}\lambda}{RR\,h\,c\,A_p\,\alpha(\lambda)^{-1}} \quad (4.2)$$

where P_{CW} is the average impinging laser power, RR and A_p are the repetition rate of the pulsed laser and the focal spot on the sample respectively, while λ and $\alpha(\lambda)^{-1}$ are the excitation wavelength and the light penetration depth at that particular wavelength. Also in this case the two different regimes are clearly observable. The decay trace is nearly monoexponential when the sample is excited at low fluence, while deviates more and more from an exponential decay as the pump fluence increases. Notice that when one electron is trapped an hole will be left in the valence band and in steady state a certain population density of *photodoped* holes n_t built up as the electron trap states are filled. This photodoped holes density can be very high even at low fluences due to a very slow de-trapping rate G_n (left panel of figure 4.1 (a)).

In the dynamic solution the two regimes can be physically explained as it follows:

(a) Under low fluence excitation, the photoexcited electron density n_e is much lower than the total concentration of free holes in the valence band, since $n_h(t) = n_e(t) + n_t(t)$ where $n_e(0) << n_t$). In this case, since the additional photoexcited charge does not noticeably alter the hole population density, the system will be well described by the monomolecular recombination case considered in the previous section and the PL decay will be monoexpometnial (c.f.r. equation 1.50).

(b) When the excitation fluence is high enough, such that $n_e(0) > n_t$, then the electron-hole bimolecular recombination is retrieved (as in 1.45), resulting in a power-law decay. When the free-electron concentration drops below the photodoped hole density, the decay again becomes monoexponential.

45

Figure 4.2: *(a) Time-integrated photoluminescence (PL) and relative quantum yield as a function of the initial excitation density. (b) Time-resolved PL decay traces for several intial excitation densities. The solid lines sre obtained computing either the steady state (a) or time-reoslved (b) solution of 4.1 with suitable parameters in order to optimize the matching with the experimental data. Figures adapted from reference.[83]*

4.3   The role of micro-structure in the emission properties

We already discussed in section 3.4 how the variable mesoscale morphologies heavily affects the absorption properties. In this section we investigate the characteristics of the photo-luminescence from two of the samples whose absorption we already discussed, thus showing that the crystallite size induced band-gap tuning goes with a shift of the PL spectral peak and a variation of the PL average life-time.

In figure 4.3(a-d) the top-view scanning electron microscopy (SEM) images of the four representative $CH_3NH_3PbI_3$ samples already presented in section 3.4 are reported for convenience. The top panel of figure 4.3(e) shows the positions of the optical UV-vis absorption spectra band edges as well as the positions of the PL peaks, while the bottom panel report the average PL lifetime as a function of the average crystallite size. Notably the optical absorption edge shift goes with the PL peak position shifts to longer wavelengths as the average crystallite size is increased. At the same time the PL dynamics get slower with an average lifetime of about $2ns$ for the smallest crystallites ($< 250nm$) and of more than $100ns$ for the largest crystallites ($> 1\mu m$).

In figure 4.3(f) the PL lifetime τ_{PL} as a function of the initial excitation density n_0 is reported for two representative samples (corresponding to figure 4.3 (a) and (d) respectively). A simple theoretical relation between these quantities can be retrieved from the rate equation considered above. Working in a low excitation regime we can discard the Auger contribution, thus simplifying the rate equation to $dn = -\beta_{rad} n^2 - A n$. In this simplified case the rate equation allow an analytic solution for $n(t)$, and consequently for the photoluminescence intensity evaluated as $I_{PL}(t) = \beta_{rad}n^2(t)$. Thus the instantaneous PL lifetime τ_{PL} can be readily evaluated as:[95–97]
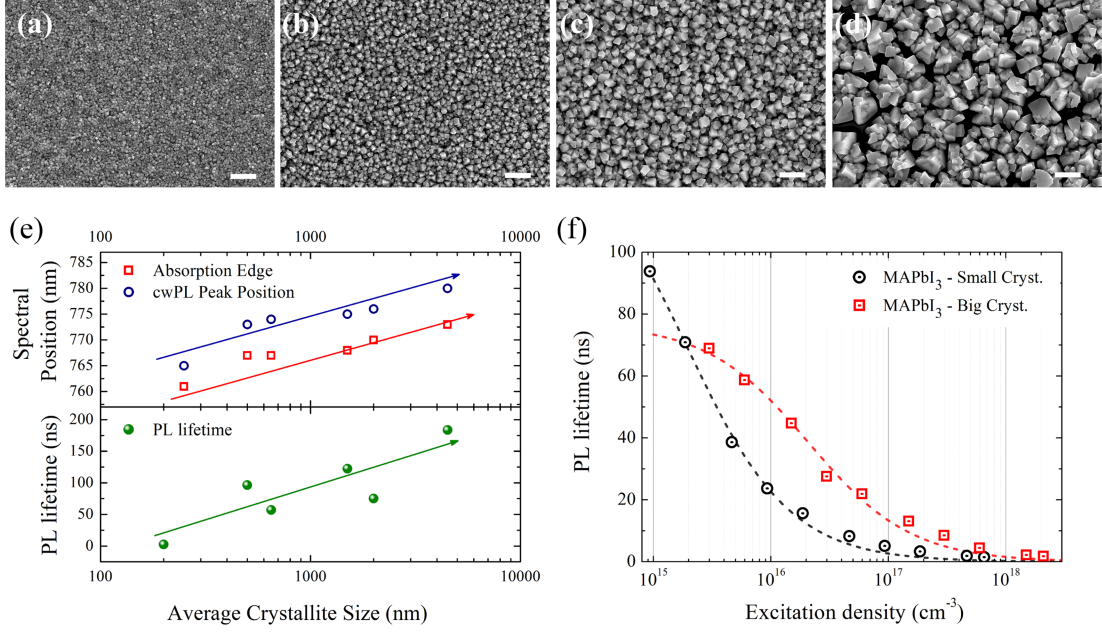
Figure 4.3: *(a,d) Top-view SEM images of $CH_3BH_3PbI_3$ formed using (a) $[MAI] = 0.063M$, $T = 25°C$; (b) $[MAI] = 0.045M$, $T = 25°C$; (c) $[MAI] = 0.031M$, $T = 25°C$; (d) $[MAI] = 0.045M$, $T = 70°C$. Scale bars are 2 μm. (e) Spectral positions of the UV-vis absorption band edge and cw-PL peak (top) and PL average lifetimes as functions of the crystallite size (bottom). (f) PL lifetime as a function of the excitation density for samples with small (black circles) and large (red squares) crystallites. Dashed lines represent the curves obtained fitting the data to eq. 4.3. $\chi^2 > 0.99$. Figures adapted from reference.[83]*

$$\frac{1}{\tau_{PL}} = \left| \frac{d\,ln(I_{PL})}{dt} \right|_{t=0} = A + \beta_{rad}\, n_0 \qquad (4.3)$$

Fitting equation 4.3 to the experimental data we retrieved both the intrinsic bimolecular radiative recombination coefficient β_{rad} and the non radiative rate A. The values are reported in table 4.1.

Sample average crystallite size	$A(1/s)$	$\beta_{rad}(cm^3/s)$
$< 250nm$	$(0.72 \pm 0.03) \cdot 10^7$	$(3.70 \pm 0.21) \cdot 10^{-9}$
$> 1\mu m$	$(1.3 \pm 0.57) \cdot 10^7$	$(0.62 \pm 0.06) \cdot 10^{-9}$

Table 4.1: *Parameters retrieved fitting equation 4.3 to experimental data*

Notably, while the non radiative coefficient A is not much affected, the β_{rad} shows a significant change going from small to big crystallites, thus suggesting a strong correlation between the optical band gap shift and the radiative recombination rate. In order to further corroborate the hypothesis of a relation between E_g and β_{rad} we performed time-resolved PL measurements as the sample temperature is lowered. As we already discussed in section 3.2.1 as the temperature is lowered, while staying above the temperature at which the phase transition occurs, the

perovskite optical band gap shifts to lower energies as a consequence of lattice strain. Thus, accordingly to the aforementioned observations, one would expect a corresponding reduction of the radiative rate. In this case, we considered a $MAPbI_3$ film deposited following the two-step procedure on a Al_2O_3 mesoporous scaffold $1\mu m$ thick (denoted as $Meso - MAPbI_3$ in the following). As the material is spincoated onto the substrate it percolates within the pores of the inert Al_2O_3 scaffold, thus preventing the formation of crystalline domains larger than $50nm$. As we discussed in section 3.4, the reduced crystallite size allows us to exclude excitonic effects even at lower temperatures.[57,60] In figure 4.4(a) the PL lifetimes as a function of the initial excitation density n_0 are reported. At fixed initial excitation density we observe that as the temperature was decreased, the PL lifetime increased and the PL spectra shifted to longer wavelengths (see figure 4.4(b)). Considering again equation 4.3 and looking at the emission recombination rates ($k = 1/\tau_{PL}$) as a function of excitation density, we can see a clear reduction of rate of the change in lifetime. Since β_{rad} is proportional to this rate, such an observation corresponds to a clear reduction of the radiative recombination rate as the temperature is lowered. Hence, the correlation between E_g and β_{rad} observed by increasing the crystal dimension can also be perceived by lowering the temperature, which notably affects the lattice strain, suggesting a direct relation between the two.
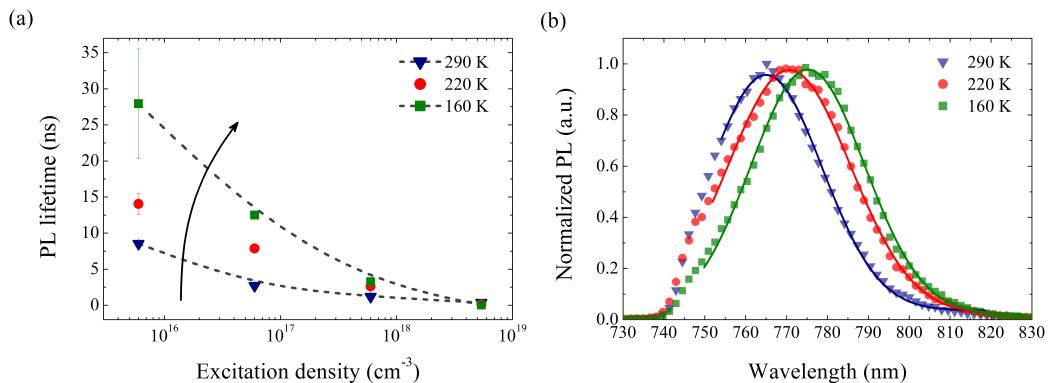
Figure 4.4: *(a) PL lifetime as a function of initial excitation density for $MAPbI_3$ deposited on a mesoporous Al_2O_3 substrate, at room temperature (black triangles), 220 K (red circles), and 160 K (green squares). All temperature a measured within an error of 10 K. The error bars refer to the 95 % confidence intervals of the fitted parameter values. (b) Time-integrated PL spectra measured at the same temperatures (symbols) and the guassian fit to the data (lines). Figures adapted from reference.[83]*

In light of the reported investigations we can claim that the observed changes in absorption and photo-luminescence properties are related to the distortion of the halide-metal-halide bonding angle. The rearrangement of the inorganic cage affecting the overall electronic band-structure induces the red-shift of the energy gap. In turn, due to the relation between the spontaneous radiative rate R_{rad} and the electronic structure of the semiconductor (c.f.r. equation 1.40), also β_{rad} will be indirectly affected by the lattice distortion. Interestingly, a detailed therotical study on the relation between the E_g and β_{rad} has recenely been reported by

Filippetti et. al.[98]

The effect of lattice distortion was both predicted through ab initio calculation[54,55] and experiemntally observed[54,90] when hybrid perovskite with different organic cations are considered. In fact, in this case, the steric hindrance and the local arrangement of the organic cation play a fundamental role in the ground state crystalline structure tuning the Pb-I-Pb bond angle, thus indirectly affecting the electronic band structure. However the possibility of engineering the band gap and the intrinsic radiative lifetime of the compound simply tuning the crystallization procedure pave the way to the optimization of the emission properties thorough a fine-tuning of the depositions steps, thus making hybrid lead-halide perovskite even more appealing, especially in view of the potential employment of these materials for lasing applications.

4.3.1 Micro-structure and optical gain

There are two crucial factors making a semiconducting material a promising candidate for the realization of low threshold CW lasing device. The first is a long excited state lifetime. This characteristic is needed in order to create a large steady-state population under continuous-wave (cw) illumination, which can be beneficial for low-threshold cw lasing. The second important parameter is the gain coefficient of the material, whose value is determined by the interplay between the recombination rates and the nonradiative losses.

In order to shed light on the latter aspect, we performed optical gain measurements using the variable stripe length method[99,100] (for details, see the methods chapter). In this experiment the spatial profile of the excitation laser is made into a stripe through a cylindrical lens, and the emission is collected from one end of the stripe. The output intensity $I(\lambda, l)$ is then related to the stripe length l by the following relation:

$$I(\lambda, l) = \frac{A(\lambda) I_p}{g(\lambda)} \left[e^{g(\lambda) l} - 1 \right] \tag{4.4}$$

where λ is the emission wavelength, $A(\lambda)$ is a constant proportional to the spontaneous emission cross section, I_p is the intensity of the pump laser and $g(\lambda)$ is the optical gain coefficient (c.f. section 1.2.3. The PL intensities from the two samples with large and small crystallites as functions of stripe length at three different pumping powers along with the curves obtained fitting equation 4.4 to the experimental data are reported in figure 4.5(a). In (b) we report the values of the fitted gain coefficients as a function of incident pump intensity, resulting to be consistently higher in the case of larger crystals. These observations allows us to suggest that larger crystals with longer PL lifetimesand higher optical gain must be preferred for the realization of CW-lasing devices.

The above discussion together with section 3.4 are showing that is possible to design the absorption and emission properties for a single material composition by tuning the processing route, thus making solution-processable perovskite-based optoelectronic technology appealing for a variety of application even beyond photovoltaics.

(a)

(b)
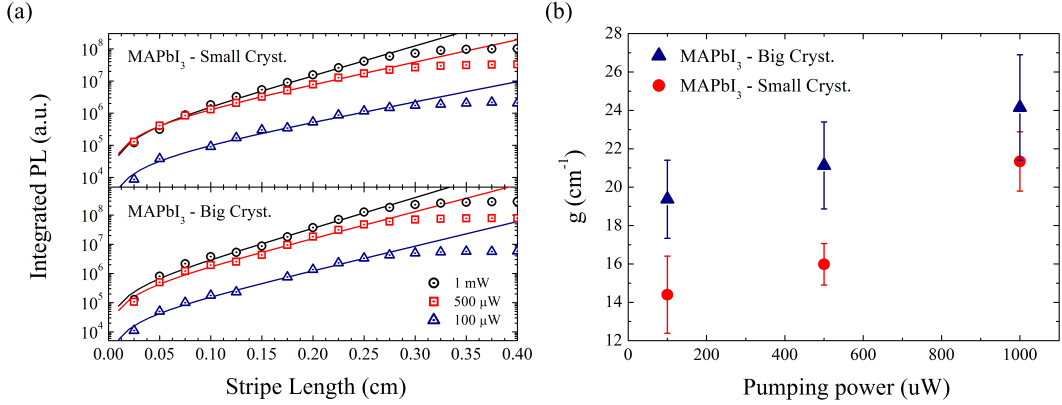
Figure 4.5: *(a) PL intesity as a function of the stripe length l for different laser excitation intensities. (b) Optical gains for $MAPbI_3$ samples with small crystallites (black circles) and big crystallites (red squares) as functions of pump laser intensity. The error bars refer to the 95% confidence intervals of the fitted parameter values. Figures adapted from reference.*[83]

4.4 Surface photophysics: environment interaction

Beyond the paramount importance of the material processing route, discussed in the previous section, the definition of the material opto-electronic properties can be heavily driven by the interaction with the surrounding atmospheric environment, and in particular with moisture.[29–35] In order to disentangle the aforementioned micro-structure effects from the material interaction with humidity, we considered some isolated $MAPbI_3$ crystals of $\approx 10\mu m$ in lateral size. These crystals were grown onto glass substrate via two-step deposition (see section 2.2) in N_2 atmosphere, exposed to air for a couple of hours and subsequently encapsulated spincoating a polymethyl-methacrylate (PMMA) thin film on top. As a consequence of this material preparation the perovksite-moisture interaction will take place mainly at the surface of the crystal thus generating a spatially non-homogeneous optical behavior.

In this section we investigate the spatial non-homogeneity of the crystal emission both in the spectral and time domain. For this purpose we coupled a microscope to a time-resolved detection system granting at the same time a μm spatial and temporal resolution (see the Methods section 2.7.1 section for further details).

In figure 4.6(a) we report the Scanning Electron Microscope (SEM) image of the investigated crystal on which we marked two different points (A and B) from which we collected the PL emission, together with the microscope images showing the laser spot focused either on point A or point B. In figure 4.6(a) the corresponding PL spectra are reported.

The steady state PL shows $10\,nm$ blue shift going from the center of the crystal (point A) to its border (point B), with the corresponding PL peaks at $\lambda_A = 774\,nm$ and $\lambda_B = 765\,nm$ respectively. As vastly reported in literature in lead-halide iodide the PL re-absorption is usually very strong due to the little stoke shift[31,65,101] characterizing this material, thus making a correct evaluation of the exact the spectral position of the emission peak usually very tricky. However it is worth noticing that in our setup the PL is collected by the same microscope
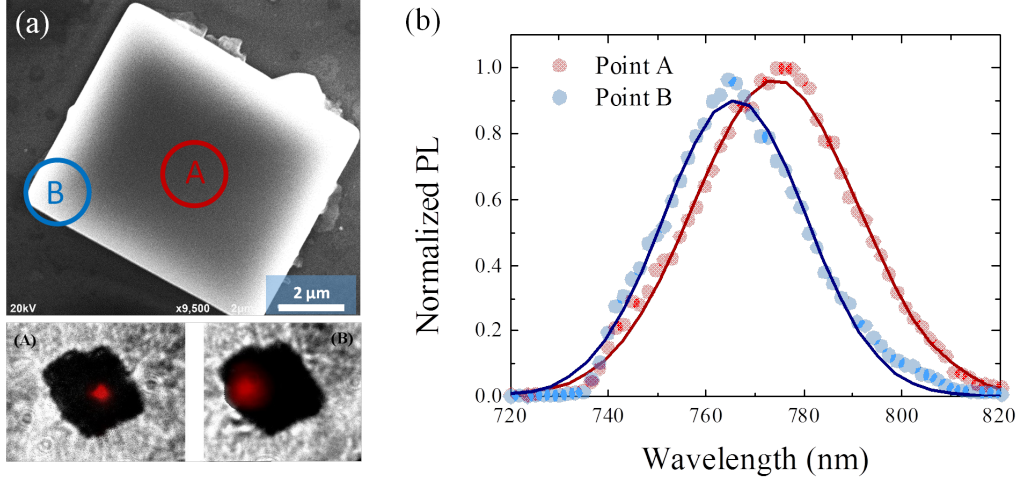
Figure 4.6: *(a) SEM image of a MAPbI$_3$ crystal from which the PL was collected either from the central part of the crystal (marker A) or the border of it (marker B) (top), and the microscope images captured during the PL collection (bottom). (b) Normalized steady state photoluminescence spectra collected either from A (red dots) or B (blue dots). The solid lines represent a Gaussian fit to the data.*

objective used for the pump laser focusing, in reflection geometry, thus we can safely assume that the photons emitted either by A or B will go through the same portion of material before being collected, thus the re-absorption will similarly affect both the spectra. Despite leaving us with a certain degree of uncertainty with respect to the absolute value of the emission central wavelength mentioned above, this allows us to claim that the observed $10\,nm$ shift cannot be ascribed to optical artifacts.

Once verified the robustness of the spectral shift we measured the PL time decays from the two different points investigated under different initial excitation densities n_0. These are reported in figure 4.7.
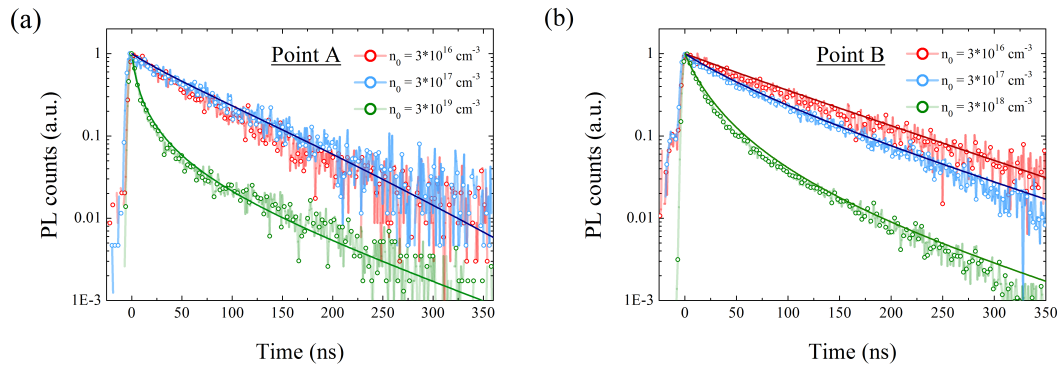
Figure 4.7: *Time-resolved photoluminescence decay collected either from (a) point A or (b) point B at different initial excitation density n_0. The solid lines represent the curves obtained fitting the rate equations model to the data.*

As expected, both in the center and on the surface of the crystal, the intensity

dependence of the PL kinetics resemble the behavior described in section 4.2.2, thus showing two different emission regimes. At low initial excitation densities, i.e. $n_0 \approx 10^{16} \, cm^{-3}$, the PL decay is dominated by trap-filling thus appearing as a long living mono-exponential, while as the laser fluence increases, the electron traps are filled and the radiative recombination retrieve its intrinsic bimolecular nature, signature of an electron-hole plasma emission, which gives rise to the intensity dependent stretched exponential decay.[65,66,83,94]

It's interesting to notice that while in the center of the crystal (point A) the transition between the two regimes is observed round $n_0^A \approx 10^{19} \, cm^{-3}$ at the edge of the crystal (point B) the transition takes place at an excitation density which is roughly one order of magnitude lower $n_0^B < 10^{18} \, cm^{-3}$ (see the green PL decays in figure 4.7). As already discussed, the initial excitation density value corresponding to the transition from the trap-limited towards the e-h plasma regime is determined by the electron trap density N_t, thus suggesting that the difference observed between the two points is related to a consistent reduction of the trap density at the crystal surface.

Parameter	Point A (Center)	Point B (Edge)
N_t	$2 \cdot 10^{17} \, cm^{-3}$	$1 \cdot 10^{17} \, cm^{-3}$
β_{rad}	$0.35 \cdot 10^{-11} \, cm^3/s$	$3.5 \cdot 10^{-11} \, cm^3/s$
k_t	$1 \cdot 10^{-10} \, cm^3/s$	$1 \cdot 10^{-10} \, cm^3/s$
G_n	$3 \cdot 10^{-11} \, cm^3/s$	$5 \cdot 10^{-11} \, cm^3/s$
γ	$4 \cdot 10^{-31} \, cm^3/s$	$4 \cdot 10^{-31} \, cm^3/s$

Table 4.2: *Parameters retrieved fitting the rate equation model 4.1 to the experimental data.*

In order to quantify the difference in trap density N_t between the center and the edge of the crystal we computed the numerical solution of the rate equations model 4.1 for different initial excitation densities, and then superimposed the simulation results to the experimental data. The curves that best matched the experimental data are shown as solid lines in figure 4.7, while the corresponding parameters are reported in table 4.2.

Among all the parameters the only value which are characterized by an important change going from the center to the edge of the crystal are the trap density N_t, which is reduced by a factor of 2, and the bimolecular radiative recombination coefficient β_{rad} which increases by an order of magnitude. As we already noticed, the increase in coefficient β_{rad} goes with a blue-shift of the PL sepctra, thus, in accordance with the discussion reported in section 4.3, we can infer that at the crystal surface a relevant increase of the local distortion of the lead-iodide inorganic cage takes place.

Very interestingly both the trap states passivation and the Pb-I lattice strain have previously been ascribed to the interaction of the crystal with the environment moisture.[30,31] In particular Grancini et al. show by ab initio molecular dynamics simulation, that water molecules can intercalate within the lead-iodide cage forming a partly hydrated phase. Moreover they show that the formation

energy of the $4\,MAPbI_3 \cdot 1\,H_2O$ complex result to be negative, suggesting a spontaneous water incorporation within the crystal lattice. The water incorporation, provoking the swelling of the crystalline unit cell, induces a widening of the gap and faster photo-carrier recombination.[31] At the same time Eperon and co-workers showed that moisture exposure of already formed perovksite films enhance both the photovoltaica and photoluminescene performances. They ascribe this improvement to a reduction in trap density, related to a solvation of the methylammonium which in turn allows an improvement of the crystalline lattice quality.[30]

In conclusion, with our work we observed a spatially non-homogeneous PL spectrum and dynamics, and we ascribe this local optical modifications to the interaction between moisture and the crystal surface. In particular the water molecules, intercalating into the crystalline lattice, on the one hand provokes a local distortion of the Pb-I bonding responsible for the steady state PL spectra shift and β_{rad} enhancement, on the other hand it induces a local defects passivation responsible for the lower initial excitation density needed to saturate the available trap states.

CHAPTER 5

Photo-luminescnce of MAPbBr$_3$ and CsPbBr$_3$

5.1 Introduction

So far we explored a system that, despite showing an excitonic resonance in absorption, is characterized by a photo-luminescence driven by an exciton free photophyics. As we already pointed out, this peculiar characteristic of $MAPbI_3$ can be explained in term of the ratio between the exciton binding energy and the lattice LO phonons energy (see section 4.1), resulting to be ≈ 1.

In order to further investigate the possible excitonic contribution to the photo-luminescence properties of hybrid perovskites we moved to lead-bromide samples which, showing a stronger excitonic transition at the band-edge, are expected to have an higher binding energy and a more stable excitonic population (see section 3.1). In particular in this chapter we deal with three different samples, comparing an $MAPbBr_3$ thin film with $CsPbBr_3$ both as a thin film and as a colloidal suspension of nano-crystals. For all the samples we performed a standard characterization of the photo-luminescence properties through both a steady-state and time-resolved PL investigation. However, since these techniques alone are not enough to unequivocally define the role of the exciton in the photophysics of our systems, we also employed the photoluminescence excitation-cross correlation technique on all the samples. In this experiment, through an heterodyne detection system, one is able to collect a signal which percieves only the non-linear contribution to the PL, thus enabling to distinguish between an electron-hole plasma emission, dominated by a quadratic dependence of the emission decay with respect to the pump intensity, and an exciton population radiative decay which is a linear phenomenon.[75] In this way we are able to show that the PL recombination kinetics of both $MAPbBr_3$ and $CsPbBr_3$ thin films, irrespectively of the high exciton binding energy, are dominated by a trap-limited free electron-hole re-

combination regime with a relevant Auger quenching under high excitation laser fluences. Moreover we observe that the $CsPbBr_3$ nano-crystals show a purely excitonic photo-luminescence with a non-linear detrimental contribution arising only at very high laser fluence.

5.2 Absorption of lead-bromide perovskite: experiment and modeling

In figure 5.1 we report the UV-Vis absorption and steady state photoluminesce (PL) spectra for $MAPbBr_3$ thin film (a), $CsPbBr_3$ thin film (b) and $CsPbBr_3$ nano-crystals (c). First of all we observe an absorption onset at $\approx 2.29eV$ for the hybrid perovskite, moving to higher energies in the case of Cs-based samples at $\approx 2.33eV$ and $\approx 2.52eV$ for the thin film (TF) and nano-crystals (NCs) respectively. Secondly we can qualitatively notice that the exciton resonance oscillator strength is increasing from panel (a) to panel (c).
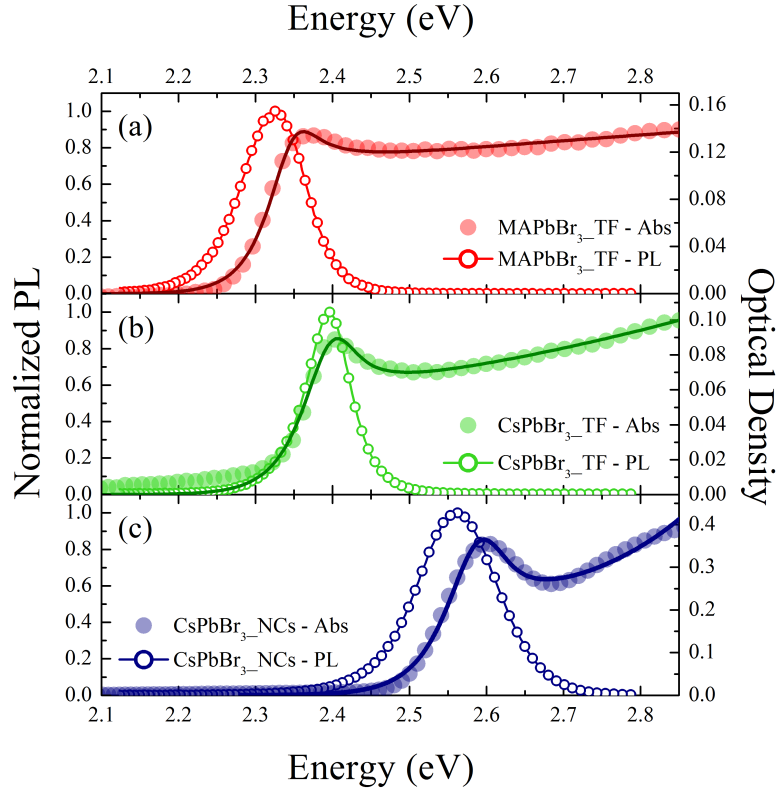
Figure 5.1: *UV-Vis absorption and steady state PL measurements collected from (a) $MAPbBr_3$ thin film, (b) $CsPbBr_3$ thin film and (c) a $CsPbBr_3$ Nano-crystal colloidal solution.*

In order to give a rough estimation of the exciton binding energy and energy gap we modeled the absorption spectra according to the Elliot's theory for the absorption of excitons in bulk semiconductor (see section 1.2.4 and section 3.1 for a detailed description). The curves resulting fitting equation 3.1 to the experimental data are reported as solid lines, the fitting parameters are reported in the following

table.

Sample	$E_B(meV)$	$E_G(eV)$	$\Gamma(meV)$	$npc(eV^{-1})$
$MAPbBr_3 - TF$	43.65 ± 0.66	2.393 ± 0.001	31.51 ± 0.31	-0.434 ± 0.015
$CsPbBr_3 - TF$	63.73 ± 0.43	2.463 ± 0.006	34.67 ± 0.21	0.444 ± 0.006
$CsPbBr_3 - NCs$	82.80 ± 0.61	2.670 ± 0.008	38.87 ± 0.30	1.9 ± 0.003

Table 5.1: *Parameters retrieved fitting the Elliot's equation model 3.1 to the experimental data of 5.1.*

It's fair to notice that, while for the TF samples the fitting procedure gave good results, in the NCs case we obtained a lower reduced-χ^2 value, suggesting that in this case the Elliot's theory for 3D semiconductor is probably not suitable. This is also confirmed by the unexpected high non parabolic parameter (npc). Despite not being fully reliable, the numbers obtained in the NCs case can still be considered a good approximation to the real values.

Considering the TF sample, as expected, when the Cs cation is substituted to the MA we observe a consistent blue-shift of the energy gap going from $\sim 2.4\,eV$ for the $MAPbBr_3$ to $\sim 2.46\,eV$ for the $CsPbBr_3$. The NCs sample show an additional shift with an energy gap of $\sim 2.7\,eV$. The exciton binding energy shows a similar trend reaching a maximum value of $83\,meV$ in the $CsPbBr3_3 - NCs$ sample. The transition inhomogeneous broadening Γ, on the other hand, shows a little variation going from sample to sample, resulting always to be $30 - 40\,meV$.

Considering the case of $MAPbBr_3 - TF$ we notice that despite the high binding energy, resulting to be almost doubled with respect to the iodide counterpart (see section 3.1), the very large energetic broadening of the transition casts a doubt on the possibility of creating a stable exciton population via photo-excitation. In fact a large value for Γ is not only related to the intrinsic thermal broadening of the transition, but also to a polycristalline disorder, usually ascribed to the random orientation of the organic cation, which affects the lattice electrostatic potential thus preventing the exciton formation.[57]

The $CsPbBr_3 - TF$, on the other hand, presents a binding energy value which is almost double with respect to its Γ, thus being a better candidate for the creation of a stable exciton population. However this sample's absorption spectra shows a relevant Urbach tail (see 3.1) suggesting an increased density of trap states. These intra-gap states, acting as exciton dissociation centers, may hamper the exciton stability.

Eventually we notice that, in the $CsPbBr_3 - NCs$ sample, both the additional shift towards higher energies of the band-gap, with respect to the TF, and the high exciton binding energy suggests that we are observing a confinement effect due to the small size of this particles, which from TEM measurements result to be cubes of $\sim 6\,nm$ later size.[40]

Notably if we consider the energetic discrepancy between the PL emission peak (open circles in each of the panel of figure 5.1) and the energy gap values reported in table 5.1 we can notice that for all the three considered sample $\Delta E \simeq 70 - 80\,meV$, thus resulting to be much larger than the expected LO phonon energy

in lead halide perovksite material.[102] Remembering that the Stoke shifts of the emission with respect to the energy gap is ultimately related to the exciton-phonon interaction,[63] the PL spectral position with respect to the energy gap rule against the hypothesis of a direct band-to-band radiative recombination, rather suggesting that the photo-luminescence is mediated by some intermediate coherent state.

5.3 MAPbBr$_3$: nature of the photo-luminescence

The relative PL yield and time-resolved photoluminescence (tr-PL) decays at different pump laser fluences for $MAPbB_3$ are reported in figure 5.2. In these experiments we changed the average laser fluence between 0.08 $\mu J/cm^2$ and 800 $\mu J/cm^2$ which, considering the sample thckness and optical density at the excitation wavelength, corresponds to a photo-exited states density n_0 between $10^{15}cm^{-3}$ and $10^{19}cm^{-3}$. It's fair to notice that we observed an instability of both the time-integrated PL signal intensity and decay time when pumping the sample at high fluences (see red dots in figure 5.2(a)). This phenomenon, already reported for mixed iodide-bromide samples,[103] despite not having yet a clear explanation is usually ascribed to extrinsic effects likely related to the ion/vacancy motion induced by the local electric field generated by the photo-excited electron-hole pairs.[104] In order to discard this spurious effect we left the sample under high fluence illumination for several hours and, only after the signal stabilization, we performed the tr-PL intensity dependence experiment.

At low excitation density the PL is characterized by a long lifetime with a decay trace roughly recalling a mono-exponential decay. As the excitation density is increased the lifetime is shortened and the decay traces show an increasing stretched exponential character. It is very interesting to notice that the relative PL yield plotted as a function of the initial excitation density, reported in figure 5.2 (a), closely resemble the one of the iodide perovskite (see figure 4.2). In fact, modeling these data with the rate equation model given by equations 4.1, we are able to get a simulation fitting very well the PL yield data (solid blue line in figure 5.2 (a)).
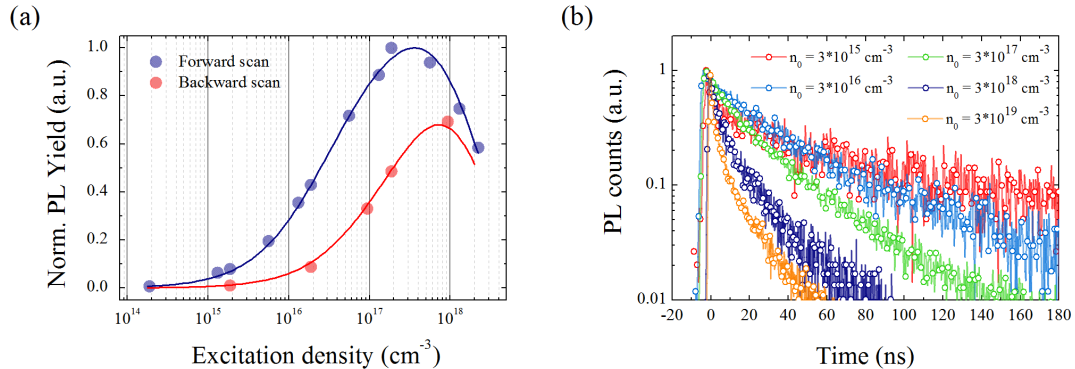
Figure 5.2: *(a) Relative PL yield collected for several initial excitation densities n_0 and (b) time-resolved photoluminescence (tr-PL) decay traces. The blue and red lines are obtained simulating the PL yield experimental data computing the time-integrated solution of equation 4.1.*

Notably in this case in order to match the experimental data we needed to introduce an extra dependence of the bimolecular recombination rate onto the initial excitation density. Due to the degeneracy of the e-h plasma under high excitation density condition the multi-particle interaction induces a quenching of β_{rad} thus slowing down the radiative recombination and reducing the PL yield. As a consequence one can disinguish two regimes. (a) Under low laser fluence, i.e. in the trap limited regime, due to the trap-filling the time integrated PL increases as $I_{ex}^{3/2}$, where I_{ex} is the laser excitation intensity, giving a PL yield growth going as $I_{ex}^{1/2}$. (b) Increasing the exciatation intensity the trpping channel is quenched and purely bimolecular regime is reached, the PL signal increases linearly with I_{ex},[75] thus giving a constant PL yield. However both the aforementioned β_{rad} saturation and the auger non-radiative recombination contribute to the saturation of the PL emission inducing the observed reduction in the PL yield for $n_0 > 10^{17} cm^{-3}$.

As already mentioned above, we observed that keeping the sample under high excitation fluence the time-integrated PL signal drops over time. In order to understand the nature of this PL quenching we repeated the time-integrated PL measurement going backwards, i.e. starting the measurement from high excitation densities after leaving the sample under high intensity illumination for some time. The resulting PL yield is reported in red dots in figure 5.2 (a). Notably when we tried to simulate these data with the model given by 4.1 in order to fit the PL relative yield backward scan we needed to drastically change the fitting parameters, thus strongly suggesting that the observed photo-induced PL quenching is likely related to a change of the radiative/non-radiative recombination channel competition, most likely accounting also for the instability of the aforementioned PL decay trace.

Despite the good matching of the trap-limited e-h plasma model with the time-integrated data we were not able to use this model to fit the decay traces reported in figure 5.2(b). We believe that the main reason for that must be sought into the observed photo-induced trap states formation. Preliminary results, discussed in the following, suggest that a more complex modeling of the trapping mechanism is needed. In particular we introduce a dependency of the trap states density onto the initial excitation density, such as $N_t \sim N_t(n_0)$, thus enabling the model to dynamically account for the aforementioned light induced trap states formation.

5.3.1 Excitation cross correlation experiment

Despite the good matching of an exciton-free model with the experimental data, we notice here that these experimental observations alone cannot exclude an excitonic PL contribution superimposing to the e-h plasma. In particular, considering tr-PL one would expect a linear excitonic recombination only at low excitation density, i.e. in the excitation regime where non linear multi-particle interactions can be neglected. However in that regime the trap limited recombination can easily hide a linear excitonic PL. Moreovoer, looking at time-integrated PL both the ideal scenarios of a pure mono-molecular ($\frac{dn}{dt} = -An + G$) and pure bi-molecular ($\frac{dn}{dt} = -Bn^2 + G$) recombination systems shows a linear growth with the excitation density (n_0).[75] In fact solving the excited state rate equations at the steady state one have that in the first case $n(t = \infty) = G/A$, while in the latter

$n(t = \infty) = \sqrt{G/B}$, where $G \propto I_{ex} \propto n_0$ is the number of excited states generated per second and unit volume by the laser source (generation rate). Thus the corresponding time integrated PL signal will be given by: $I_{mono} = An(t = \infty) \sim n_0$ and $I_{bi} = Bn(t = \infty)^2 \sim n_0$.

In order to isolate the potential excitonic (i.e. linear) contribution to the PL we performed a photoluminescence excitation correlation experiment (PEC).[105–108] In the PEC experiment a pulsed laser source is split with a 50% beam splitter, each of the beams is modulated with an optical chopper blade with two different frequencies ($\omega_{1,2}$) while only one of them is delayed with a delay τ with respect to the other. The beams are subsequently rejoined onto the same spot on the sample and the resulting PL is collected onto a slow photodiode plugged into a Lock-in amplifier referenced to the $\omega_1 + \omega_2$ frequency. The resulting PEC signal leans only on the non linear contribution to the photo-luminescence, thus furnishing a direct tool to probe weather the exciton does play a role in the perovskite lead-bromide photophysics (for a detailed experiment description refer to section 2.8).
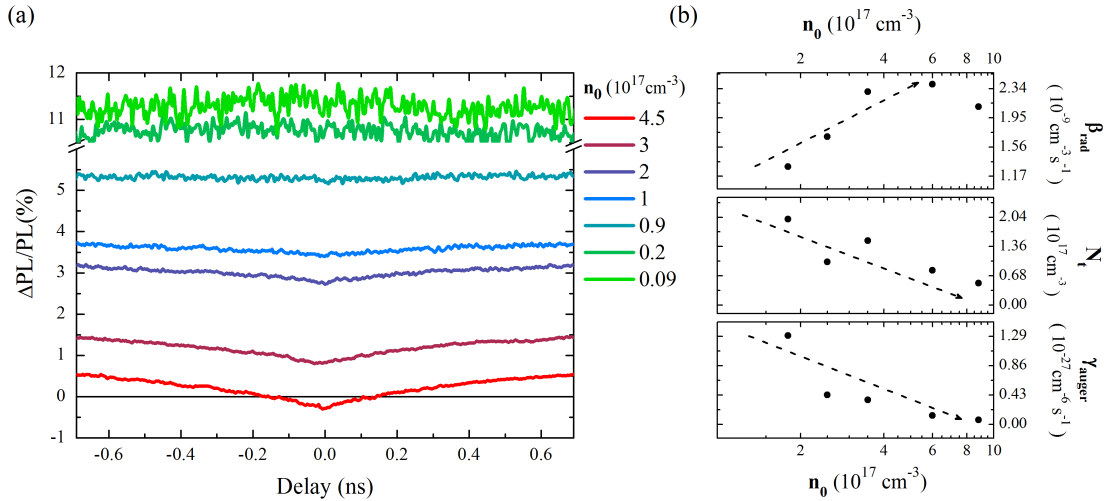
Figure 5.3: *(a) PL Excitation cross-correlation as a function of time delay between the laser pulses, under different initial excitation densities. (b) Values of β_{rad}, N_t and γ fed into the rate equation model (ref. 4.1), in order to best fit the experimental PEC data, as a function of the initial excitation density n_0*

In figure 5.3(a) the $MAPbBr_3$ thin film PEC signal as a function of the delay between the two pulses is reported. We repeated the experiment under increasing initial excitation density, going from $9 \cdot 10^{15} cm^{-3}$ to $4.5 \cdot 10^{17} cm^{-3}$. Once again, in order to avoid spurious effects, we let the sample under high power illumination for several hours in order to stabilize the signal. We observe that under low excitation the signal is positive and almost flat in the delays temporal window explored (-0.7 to 0.7 ns). As the laser intensity is increased we observe both an overall reduction of the PEC signal and the appearance of a negative peak with a dynamic getting progressively faster. Notice that, due to the specific nature of the PEC signal, the presence of a non-null signal at $n_0 < 10^{16} cm^{-3}$ is already an indication of the fact that, even in that regime, the luminescence is governed by a long-living non-linear

radiative process. In particular we ascribe this PEC signal to the bimolecular radiative recombination characterized by a decay time approximately given by $\tau_\beta \simeq (\beta_{rad} n_0)^{-1} \approx 10^{-6}s$, thus accounting for the fact that in the explored delay window the decay cannot be perceived. As the initial excitation density increases the characteristic time of the bimolecular recombination path decreases and at the same time the Auger recombination is no more negligible. Being a non-radiative relaxation path the Auger is a negative contribution to the PEC signal, resulting in the observed deep centered at zero delay time. It is worth noticing that at the highest excitation laser fluence employed we observe a negative PEC signal (red curve in figure 5.3) corresponding to the relative PL yield data decrease observed for $n_0 > 2 \cdot 10^{17} cm^{-3}$ (see 5.2(a)).

In order to support the qualitative picture of the photophysics underlying the light emission in hybrid lead-bromide perovskite, we computed the numerical solution of the rate equation set describing the recombination dynamic of the excited e-h pair (see equations 4.1) considering a two pulse excitation and choosing a suitable triple $[N_t, \beta_{rad}, \gamma]$ in order to match the experimental data for each different initial excitation density (see section A.3 for further details). In figure 5.3(b) we report the values of the trap density N_t, bimolecular recombination rate (β_{rad}) and auger recombination rate (γ) that best fitted the experimental PEC signal, as a function of the initial excitation density n_0. Firstly we observe that the intrinsic radiative bimolecular recombination rate β_{rad}, after an initial increase, saturates at $n_0 \simeq 4 \cdot 10^{17} cm^{-3}$ and then drops for $n_0 > 6 \cdot 10^{17} cm^{-3}$, in accordance with the aforementioned degeneracy of the e-h plasma in high excitation regime. Turning now to the density of electron-trapping sates N_t we observe a consistent reduction of the density of trapping sites N_t as the initial excitation density increases. Tough this results are still preliminary the observed light-induced quenching is indirectly suggesting that in the hybrid lead-bromide perovskite the charge carrier trapping is mediated by charged defect sites. In fact upon light illumination the photo-generated charge carriers can slowly neutralize these sites, thus reducing the traps contribution to the excite state recombination dynamic. Eventually we observe that the Auger recombination rate γ is reduced along with the traps density, thus suggesting that we are observing a trap mediated Auger recombination as already reported for other crystalline semiconductors.[68]

Summarizing we claim that the observed PEC signal as a function of the initial excitation density arises from the competition between the radiative e-h plasma recombination, dominant at low excitation fluences, and the three-particle non-radiative contribution, superimposing to the first one.

Riparafrasa aggingendo che la dipendenza dalla temperatura e il fatto che siano siti carichi suggerisch che siano ioni mobili come per Michele

In order to investigate in more detail the slow trap density variation, leading to the observed signal instability, we performed the PEC experiment under high excitation fluence ($\approx 30 \mu J/cm^2$) collecting subsequent scans (5 minute each) until signal stabilization. We then repeated the experiment keeping the sample in a controlled temperature atmosphere ranging from room temperature to 77 K. As shown in figure 5.4 the signal collected at room temperature grows in time and it is stabilized after approximately one hour measurement. Notably the time needed
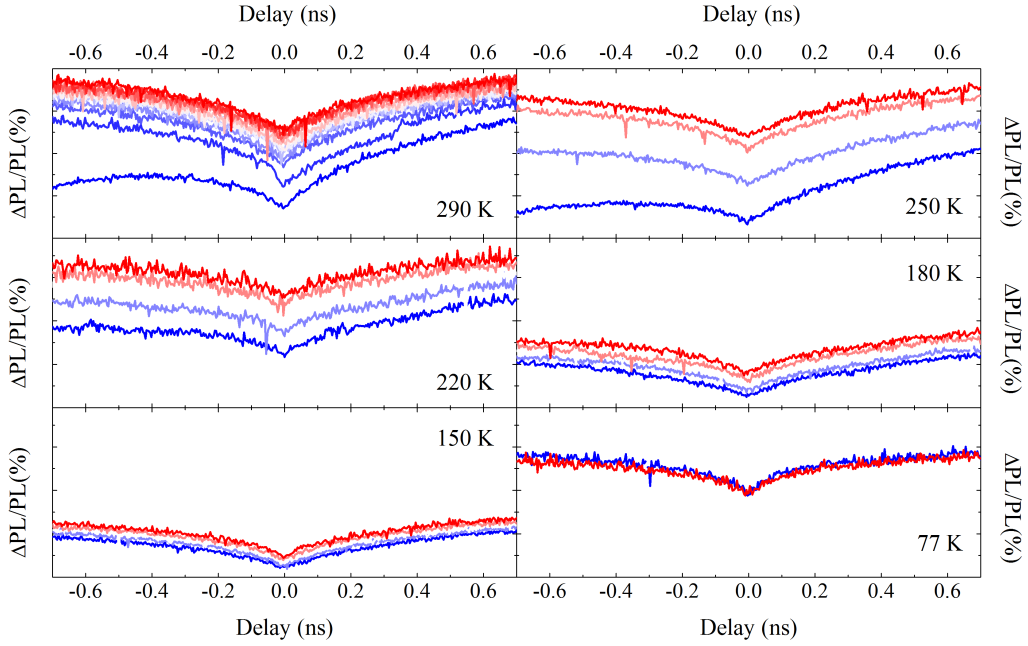
Figure 5.4: *Excitation cross-correlation signal collected from an MAPbBr₃ thin film under a laser fluence of $\approx 30\mu J/cm^2$ (1 mW average power on a 70μm radius spot) as a function of the time delay between the pulses. The measurement was repeated at different temperature between 290 K and 77 K.*

to stabilize the PEC signal decreases as the temperature is decreased, and it's nullified at 77 K since in that case the PEC signal is already stable after only one scan. We notice that, according to our previous interpretation, the observed increase of the PEC signal over long time scale is at least partially due to a slow reduction of the Auger rate γ. Being the Auger recombination a trap mediated process ($\gamma \propto N_t$) when we observe that with decreasing temperature the quenching of this non-radiative path gets faster, we are actually observing that the charged trapping sites are passivated in a progressively shorter time as the temperature goes down.

Drawing the conclusion, despite being preliminary studies, the intensity and temperature dependance of the PEC experiment partially unveil the nature of the trapping sites. On the one hand the reported decrease of trap density with increasing excitation laser fluence suggests that the trapping process is mediated by non-neutral trapping site; on the other hand the marked temperature dependence of the trap passivation rate suggests a shallow trapped carrier energy level. In fact, while at room temperature the thermally activated de-trapping process is quite efficient leading to a slow trap-filling, at lower temperature the de-trapping becomes negligible and the trapping rate passivation is quicker. It's worth noticing that the phyical picture we reported is compatible with an ions/vacancies motion mediated trapping as already vastly investigated and reported in the lead-iodide perovskite case[104, 109] and in the mixed halide one.[103]

5.4 CsPbBr$_3$: the role of the exciton

As already discussed in the introduction, recent works in hybrid lead-halide perovskite demonstrated that the polarized MA^+ organic moiety is characterized by an high mobility in the 0.1-1 ps time scale,[110] indirectly influencing the electronic properties of the material via the dipole-lattice dynamic interaction. In particular Grancini et al. observed that the electrostatic potential variation induced by the organic moiety morphological disorder can disrupt the long-range crystalline order preventing the possibility to sustain a stable exciton population.[57] For this reasons, in order to grant an higher energetic order, we moved to consider a perovskite with an inorganic cation as $CsPbBr_3$. Moreover we considered both a thin film sample and a nano-crystals colloidal suspension of the same material, thus exploring how the different material micro-structuring affects the emission properties in the Cs based perovskite case.
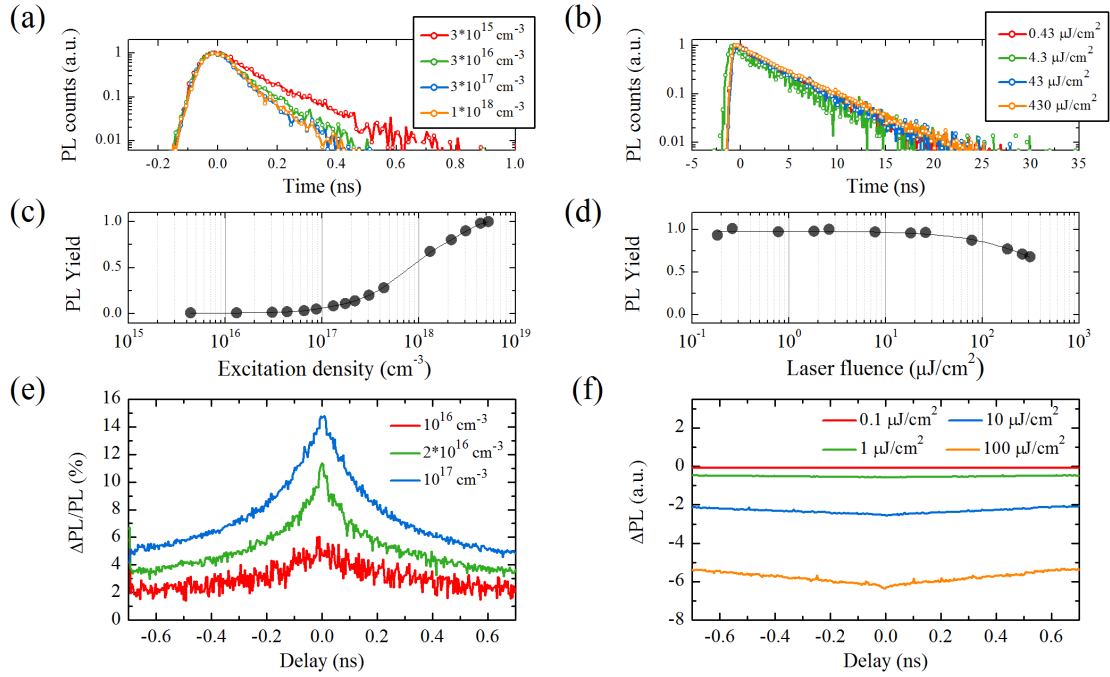
Figure 5.5: *Photoluminescence decays and normalized relative PL yield of $CsPbBr_3$ thin film (a,c) and nanocrystals (b,d), as a function of initial excitation density n_0 and impinging laser fluence respectively. (e)-(f) PL Excitation cross-correlation measurements for the same samples collected respectively at $n_0 = 10^{16} cm^{-3}$ (red), $n_0 = 2 * 10^{16} cm^{-3}$ (green), $n_0 = 10^{17} cm^{-3}$ (blu) for the thin film (e) and $F = 0.1 \mu J cm^{-2}$ (red), $F = 1 \mu J cm^{-2}$ (green), $F = 10 \mu J cm^{-2}$ (blue) and $F = 100 \mu J cm^{-2}$ (orange) for the nanocrystals (f). $\lambda_{ex} = 400nm$, repetition rate $RR = 250 kHz$.*

In figure 5.5 (a) and (b) we report the time-resolved photoluminescence decays for the thin film (TF) (a) and the nano-crystals (NCs) sample. First of all we observe that the TF sample PL decays within $1ns$, thus resulting to be approximately one order of magnitude faster than the NCs. As a result the PL decay traces reported in panel (a) of figure 5.5 are heavily affected by the system impulse response, being of $\sim 70ps$. However, despite being at the limit of our temporal

resolution, we can observe a clear dependence of the characteristic PL decay time on the initial excitation density n_0, suggesting once again a bi-molecular radiative recombination process. On the contrary the NCs sample shows a neat mono-exponential PL decay with a $\approx 4ns$ lifetime irrespectively of the impinging laser fluence. Notably both these characteristics are signature of a coherent state, i.e. excitonic photo-luminescence.

Subsequently we evaluated the relative PL yield on both the samples, data reported in figure 5.5 (c) and (d). Interestingly also in this case the TF and NCs show dramatically different behaviors under increasing pumping laser power. On the one hand the $CsPbBr_3$ TF sample is characterized by a very low PL yield under low excitation fluence, which increases once the laser fluence generate an $n_0 > 10^{17}cm^{-3}$ excited states per unit volume. On the other hand the NCs sample is characterized by a constant PL yield, dropping slightly when $F > 50\mu Jcm^{-2}$.

We notice that in the case of $CsPbBr_3$ TF both the pump intensity dependence of the PL lifetime and the increasing in PL yield (see figure 5.5 (a) and (c) respectively) resemble what we already reported for $MAPbBr_3$ sample, thus suggesting that, despite the cation substitution, the photophysics driving the photo-luminescence is again related to a trap-limited electron-hole plasma radiative recombination. In the NCs case, on the other hand, the constant PL yield in the low excitation regime is consistent with the hypothesis of a solely excitonic photo-luminescence. It's interesting to notice that the PL quenching observed in figure 5.5 (d) in the high excitation regime is not accompanied by a shortening of the emission lifetime, thus ruling out the formation of a competing non-radiative decay path in the same temporal regime of the intrinsic PL rate emission as discussed in the case of both $CsPbBr_3$ and $MAPbBr_3$ thin film.

In order to both verify the e-h plasma pictures we proposed for the $CsPbBr_3$ TF and to elucidate the nature of the aforementioned PL quenching in NCs we performed on both the samples the PEC experiment under different initial excitation densities, data reported in 5.5 (e) and (f) respectively.

In the $CsPbBr_3$ TF case we observe a positive PEC signal peaking at zero time delay and growing as the exciting laser intensity is increased. In accordance with the PL yield data of figure 5.5(c) even under the highest available exciting laser fluence we do not observe any detrimental contribution to the PL, suggesting that the Auger decay path is not playing any relevant role within the explored initial excitation density range. Moreover the PEC dynamic gets faster as the initial excitation density increases and at $n_0 = 10^{17}cm^{-3}$ the signal is reduced of a $1/e$ factor after $\approx 0.4ns$, a value which is fully compatible with the sub-nanosencd PL decay reported in figure 5.5(a). As already discussed a positive PEC signal is related to a non linear PL contribution, thus supporting the proposed e-h plasma model with a reduced Auger contribution for the TF photo-luminescence.

In figure 5.5(f) the PEC collected from the $CsPbBr_3$ NCs sample under an increasing excitation laser fluence. Notice that in this case the PL change (ΔPL) was so large that the normalization in order to retrieve a relative value was non-trivial, thus the absolute PL variation is reported in arbitrary units. Under low excitation fluence we obtain a zero PEC signal, and as the excitation laser intensity is increased the signal becomes negative monotonically, however keeping the same

temporal dynamic. In the case of NCs it is intuitive to consider the average number of excitations per nano-crystal corresponding to the laser fluence reported in figure. Through the definition of an *effective* bulk absorption coefficient $\alpha_{eff} \sim 2 \cdot 10^4 \, cm^{-1}$ one can evaluate the NC absorption cross section as $\sigma \simeq \alpha_{eff} \cdot V$, where V is the nano-crystal volume and ϕ is the impinging photon flux. The average number of excitations for each of the nano-crystal is then readily evaluated as $n_{ex} = \sigma \cdot \phi$. It's very interesting to notice that the relative PL yield starts to drop significantly from unity when $n_{ex} > 1$, thus suggesting that the observed PL quenching is due to a non-linear interaction between excited states. In particular as the first pulse is absorbed the excited state population density will be $n_{ex} \propto n_0$ and under high enough laser fluence more than one excited state per nano-crystal will be created. However the ultra-fast auger interaction among the photo-excited species induces their de-excitation bringing the system back to the single excitation per nano-crystal status irrespective of the initial excitation. Overall this fast non-radiative de-excitation results in a saturation of the PL emission. As a consequence the first incoming pulse will saturate the PL emission and the delayed pulse brings a detrimental contribution to the PL ($\Delta PL < 0$). The PL emission will be recovered with the intrinsic exciton lifetime τ_{ex}: $n_{ex}(t) \simeq n_0 \, e^{-t/\tau_{ex}}$, thus giving a PEC signal going back to zero with a characteristic time $\tau_{ex} \simeq 4 \, ns$, irrespective of the impinging laser intensity.

As a consequence of these observation we consider the PEC signal to be fully consistent with the excitonic emission we proposed above. In particular:

(a) when the average excitation per nano-crystal is below 1 the PL emission is driven by a purely escitonic radiative recombination. Being this process linear, a zero PEC signal is observed.

(b) For $n_{ex} > 1$ an ultrafast multi-excioton non-linear interaction hinder the possibility to populate each nano-crystal with more than one excitations, thus resulting in a saturation of the excited state population and a negative PEC signal, increasing in absolute value as the excitation fluence is increased.

The origin of such a auger process is however out of scope of this study, though it highlights a major bottleneck in the application of these structures in lasing applications. Like the cases of PbS and CdSe based nanocrystals, one may have to explore core-shell kind of heterostructures to obtain considerable gain even in the single exciton regime[111, 112] and avoid multi-partcle interactions.

In figure 5.6 the optical density of $CsPbBr_3$ TF and NCs are reported in log scale (dots) together with the corresponding fitting curves (sold lines). The shaded are between the experimental and fitted curves furnish a visual quantification of the relative weight of the Urbach tail in the absorption of these two samples. It's very interesting to notice how, despite sharing the same chemical composition, the different production procedures is leading to a much higher defect density in the case of the thin film with respect to the nano-crystals. Even if not conclusive this simple observation allows us to claim that the crystalline quality is a crucial element in the determination of the material photo-luminescence properties, to the point of determining the photophysics governing the recombination processes.
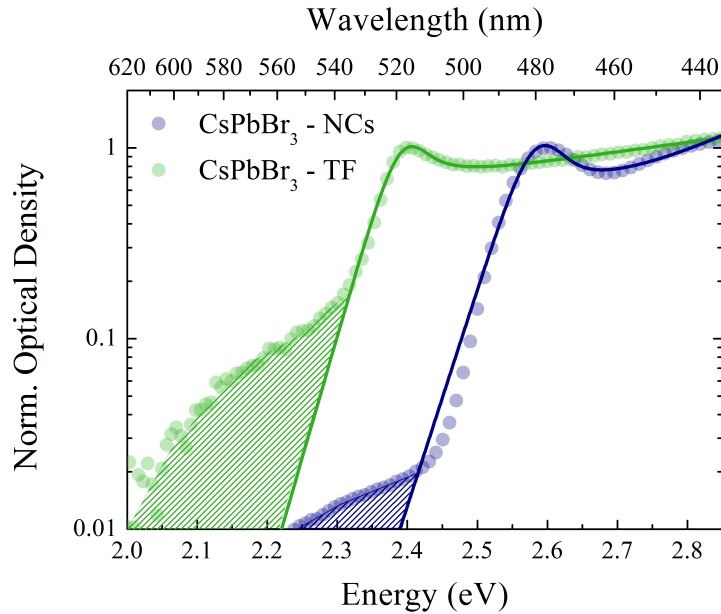
Figure 5.6: *Optical density of CsPbBr₃ thin film and nano-crystals (green and blue dots respectively), together with the curves obtained fitting equation 3.1 to the experimental data. The shaded area represent a visual quantification of the Urbach tail contribution to the absorption.*

In summary, thanks to the combination of a traditional tr-PL and PL yield characterization with the PEC experimental techniques, we demonstrated that the lead-bromide perovksite thin film samples are characterized by a recombination dynamic driven by a trap-limited electron-hole plasma emission, irrespectively of the cation substitution leading to a larger estimated exciton binding energy. Moreover we discussed the dramatic influence of the material microstructuring on the emission properties. In particular we showed that the $CsPbBr_3$ nano-crystals, despite sharing the same chemical nature with the thin film samples, are characterized by a purely excitonic PL limited only by an absorption saturation effect. Eventually we showed that this drastic difference is, at least partially, due to an higher defects density which, disrupting the long range crystalline order, hamper the stabilization of an excitonic population.

Conclusions

THE perovskite based photovoltaic technology has been characterized by an extremely rapid development, drawing the majority of the research effort to the device performances enhancement and leaving behind a thorough understanding of the photon to current conversion mechanisms in this class of semiconductors.

The work presented in this thesis contributes to the filling of the huge gap between the devices performance improvement and the understanding of the photophysics behind the photovoltaic process. We performed a steady state and time-resolved spectroscopic investigation of the absorption and photo-luminescence on both lead-iodide and lead-bromide perovskite samples, focusing on the relation between the material micro-structuring and its optoelectronic properties.

Absorption spectroscopy

With a temperature dependent UV-Vis absorption measurements on $CH_3NH_3PbI_3$ ($MAPbI_3$) and $CH_3NH_3PbBr_3$ ($MAPbBr_3$) sample we are able to define the context in which the lead-halide perovskites need to be located. In both the investigated case we observe the clear spectroscopic signature of an exciton, i.e. a coherent state due to the coulomb interaction between an hole in the valence band and en electron in the conduction band. Thus as a preliminary conclusion we can with certainty ascribe this class of materials to the family of the crystalline direct band-gap semiconductors.

Subsequently we investigated the influence of the crystalline micro-structure on the absorption properties of lead-iodide perovksite. We observe that when the material is grown within an inert meso-scaffold and/or in the shape of small grain poly-crystalline thin films the excitonic contribution to the absorption spectra is quenched even at low temperature. Thus we show that the material formation process, disrupting the long-range crystalline order, can alter the local electric screening and consequently tune the photophysical processes governing the exciton to free-carrier ratio at thermal equilibrium.

Luminescence spectroscopy

We investigated the steady state and time-resolved photo-luminescence (PL) of $MAPbI_3$ showing that a **Shockley–Read-Hall**, i.e. a trap limited electron-hole plasma, recombination process governs the light emission. Thus we identified as crucial the competition between the intrinsic bimolecular radiative recombination rate β_{rad} and the density of available traps N_t. Notably we showed that the opto-electronic properties of this material are characterized by an intrinsic variability. In fact we observed that different deposition routes, influencing the lead-iodide cage strains, can indirectly alter the electronic structure of the semiconductor resulting into a direct tuning of the luminescence spectral position and characteristic lifetime.

Subsequently we investigated the lead-bromide perovskite both in its hybrid ($MAPbBr_3$) and fully inorganic ($CsPbBr_3$) form. Combining the PL excitation cross-correlation technique with the more conventional time-resolved and steady state PL measurements we are able to define the role of the exciton in the light emission process. We show that when the material is deposited as a thin film, despite showing a strong excitonic feature in absorption, the system relaxation taking place after the photo-excitation is once more dominated by a **Shockley–Read-Hall** recombination, characterized by a photo-induced dynamic variation of trap density. The exciton emission, however, can be retrieved controlling the material's microstructure. In fact considering a colloidal suspension of $CsPbBr_3$ nano-crystals we observe a solely excitonic photo-luminescence limited only by a non-radiative exciton-exciton interaction effect.

In summary on the one hand we identified the reduction of traps density, via material's processing optimization, as one of the key issue to tackle in order to improve the device performances as photovoltaic and light emitting devices. On the other hand we showed that the synergy between the choice of the cation and the material's deposition route can drastically change the photophysics governing the light matter interaction of these material. Thus we identify both the reduction of crystalline defects and the micro-structuring as the way forward in the tailoring and engineering of lead-halide perovskites for photonics applications.

Appendix

I~n this section we will report the coding scripts employed for the implementation of fitting and simulation of the experimental data as specified into the text.

All the software were developed in **Python 3.0** language into the *iPhyton notebook* environment.

For seek of completeness and clarity we list in here the headers used in order to import the necessary library for the codes execution.

```python
import numpy as np
import matplotlib.pyplot as plt
import matplotlib.ticker as ticker
# ODEpack tool for differential equation integration
from scipy.integrate import odeint
# Optimization tool
import scipy.optimize as opt
#Interpolation tool
from scipy.interpolate import interp1d
```

A.1   Elliot's theory absorption coefficient

Since the absorption coefficient fitting was performed through an ordinary least squares method, first of all we defined a function taking both the parameters initial values vectors `p`, the experimental data `a_exp` and the energy x-axis `e`. The function returns the difference between the experimental data and the simulated absorption coefficient.

```python
def Elliots_fit(p, a_exp, e):
```

```python
Eb, Eg, gamma, npc, k = p

# Descrete transitions to the excitonic states
absex = np.zeros((e.size))
n = np.linspace(1, 500, 500)

for i in range (0, e.size):
    expr = 4*np.pi*(Eb**(3/2))/(n**3)*1 ...
        ((np.cosh((e[i]-Eg+Eb/n**2)/gamma)))
    S = expr.cumsum(axis=0)
    absex[i] = S[-1]

# Band to band absorptio with Sommerfeld correction
abseh = np.zeros((e.size))

def fun_eh(x,e,gamma,Eb,Eg,npc):
    D = (x-Eg)/Eb
    return (1/(np.cosh((e-x)/gamma))*2*np.pi*np.sqrt(Eb)...
        /(1-np.exp(-2*np.pi/(np.sqrt(D))))*1/(1-npc*(x-Eg)))

for i in range (0, e.size):
    q = quad(fun_eh, Eg, inf, args=(e[i],gamma,Eb,Eg,npc))
    abseh[i] = q[0]

# Complete Abs simulation (background added)

abs_sim = np.zeros((e.size))

for i in range (0, e.size):
    abs_sim[i] = (e[i]/Eb**(3/2))*(absex[i]+abseh[i])
return(abs_sim*k-abs_exp_fit)
```

Subsequently the experimental data are loaded, and the least square method is called through the `opt.leastsq` function. Within the least square minimization the function will be called each time with different parameters and the procedure will stop once the difference is lower than the error tolerance chosen. Eventually the standard errors are evaluated for each of the parameters.

```python
# Data loading
data = np.loadtxt('filepath', delimiter="\t", skiprows=0)
e_exp = 1240/data[:,0]        # concerted from nm to eV
a_exp = data[:,1]-data[0,1]   # removing the background


# Intial Values
Eb = 0.030                    # exciton binding energy (eV)
```

```
gamma = 0.029          # inhomogeneous line broadening (eV)
Eg = 2.402             # semiconductor bandgap (eV)
npc = −0.31            # non−parabolic coefficient
k = 0.0035


# Energy axis generation
ix0 = np.searchsorted(e_exp,1240/430)
ix1 = np.searchsorted(e_exp,1240/555)
e = np.linspace(e_exp[ix0], e_exp[ix1], 500) # energy axes (eV)


p0 = [Eb, Eg, gamma, npc, k]

#Fit Calling
# Interpolating the simulated abs over the exp x−axis
f = interp1d(e_exp,a_exp)
abs_exp_fit = f(e)
opt_out = opt.leastsq(Elliots_fit, p0, ...
                      args=(abs_exp_fit, e), full_output=1)
fitted_param = opt_out[0]

#Standard error evaluation
fitting = Elliots_eval(fitted_param, e)
if (len(abs_exp_fit) > len(p0)) and opt_out[1] is not None:
    s_sq = ((fitting−abs_exp_fit)**2).sum()...
        ((len(abs_exp_fit)−len(p0)))
    pcov = opt_out[1] * s_sq
else:
    pcov = inf

error = []
for i in range(len(opt_out[0])):
    try:
        error.append( np.absolute(pcov[i][i])**0.5)
    except:
        error.append( 0.00 )
pfit_leastsq = opt_out[0]
perr_leastsq = np.array(error)
```

A.2 Rate equation model

In order to simulate the PL time evolution under different exciting laser fluence we computed the numerical solution to the 4.1 model using different initial excitation densities n_0 as initial condition. Here the physical constants and the simulation parameters `Nt`, `kb`, `gt`, `gr` **and** `gamma` are initialized.

```
#Initial condition for excited state population
Pcw = np.logspace(0,4.1,100)*1e-6          # Avarage CW power in W
lambda = 400*1e-9                           # wavelength in m
h = 6.67*(10**(-34))                        # Plank Constant [Js]
c = 3*(10**8)                               # Speed of light
Ap = np.pi*(70*10**(-6))**2                 # Spot size in m^2
OD = 0.28
```

```
#Since the penetration depth is round 1um (OD=0,27 @ 400nm for 700nm
    thick sample), we consider the light to be absorbed in the whole
    thickness of the sample
d = 700*1e-9     # Sample thickness in m
```

```
Iex = Pcw/(Ap)   # Excitation intensity (W/m^2)
RR = 250*1e3     # Repetiotion rate (1/s)
```

```
Nt = 1e18            # available traps density (cm^-3)
kb = 4e-10           # bimolecular recombination rate
gt = 6e-11           # electron trapping rate (cm^3/s)
gr = 1e-12           # detrapping rate  (cm^3/s)
gamma = 1e-28        # Auger rec rated  (cm^6/s)
```

```
# Fluence (uJ/cm^2)
F = Pcw/(RR*Ap*1e4)*1e6
# Excitation density cm^-3
n_phot = Pcw*(lambda)/(RR*h*c*Ap*d)*10**(-6)
```

In order to take into account the bi-molecular recombination rate (β_{rad}) quenching due to a fermion gas degeneracy under high excitation fluences, for each initial excitation density we defined an effective β_{eff} as: `k = kb*sat[i]`, where `sat[i]` is the i-th element of the *saturation* coefficient. The saturation coefficient value as a function of the excitation density was evaluated from a separate calculation taking into account two degenerate fermion gases, representing the holes in the valence band and the electron in the conduction band, and computing the radiative recombination rate as a function of the excited population density: $\beta_{rad}(n_0)$. Normalizing this value to one we obtained the *saturation factor* stored in `sat[i]`.

```
# kb saturation from degenerated fermion gases calculations

Calc = np.loadtxt('kb_sat.txt', delimiter="\t", skiprows=0)
n_abs_calc = Calc[:,0] # excitation density in cm^-3
sat_fact = Calc[:,1]
f_sat = interp1d(n_abs_calc,sat_fact)
sat = f_sat(n_phot*(1-10**(-OD)))
```

The set of ordinary differential equation described in section 4.2 is implemented defining a function `f(y, t, kb_eff)` which takes as parameters the initial condition vector `y`, containing the population densities at time zero, the time vector `t`

containing all the time step at which the solution is computed and the effective β_{eff}.

```
# solve the system dy/dt = f(y, t)
def f(y, t, kb_eff):
        ne_i = y[0]
        nh_i = y[1]
        nt_i = y[2]


        # rate eq for electrons
        dne = − kb_eff*ne_i*nh_i − gt*ne_i*Nt*(1−nt_i/Nt) − gamma*
            ne_i*nh_i**2
        # rate eq for holes
        dnh = − kb_eff*ne_i*nh_i − gr*nh_i*nt_i − gamma*ne_i*nh_i**2
        # rate eq for traped electrons
        dnt = gt*ne_i*(Nt−nt_i) − gr*nh_i*nt_i

        return [dne, dnh, dnt]
```

Notice that since the de-trapping rate G_n is usually very slow, the filled traps population density won'r decay completely within the time range between two subsequent pulses, being in our case $t_{pp} = \frac{1}{RR} = 4\mu s$. As a consequence when the sample is excited with a pulsed laser a filled traps background will be established. This background will affect the recombination dynamics since it contribute to the reduction of the effective density of available traps N_t. In order to account for this phenomenon in our computation we computed the dynamic solution of `f(y, t,k_eff)` due to the first incoming pulse, i.e. setting the initial condition for the density of traps to zero (`y0first = [n_abs,n_abs,0]`). Subsequently we consider a second incoming pulse which will build up a photo-excited population over the electron and holes population evaluated at time $t = t_{pp}$ after the first incoming pulse. The resulting initial condition vector for the second pulse will then be: `y0 = [n_abs+ne_first[ix,i],n_abs+nh_first[ix,i],nt_first[ix,i]]`.

The PL dynamic is then evaluated as $PL(t) = k\,n_e\,n_h$ and normalized to one in order to be compared with experimental data, while the time-integrated values is simply obtained as `PL[i] = np.trapz(PL_dyn[:,i],t)*RR`.

```
# time grid
t = np.logspace(−13,−4, 100000)


#Initialization


#First pulse population giving the initial condition
#for the rest of the pulses
ne_first = np.zeros((t.size,Pcw.size))
nh_first = np.zeros((t.size,Pcw.size))
nt_first = np.zeros((t.size,Pcw.size))
PL_first = np.zeros((t.size,Pcw.size))
```

```python
#Rest of pulses initialization
ne = np.zeros((t.size,Pcw.size))
nh = np.zeros((t.size,Pcw.size))
nt = np.zeros((t.size,Pcw.size))
PL = np.zeros((Pcw.size))
PL_dyn = np.zeros((t.size,Pcw.size))


for i in range(0,Pcw.size):
    n_abs = n_phot[i]*(1−10**(−OD))
    k = kb*sat[i]
    # initial condition vector [electron,hole,trap]
    y0first = [n_abs,n_abs,0]

    #First pulse simulation
    soln_first = []
    soln_first = odeint(f, y0first, t, args=(k,))
    ne_first[:,i] = soln_first[:, 0]
    nh_first[:,i] = soln_first[:, 1]
    nt_first[:,i] = soln_first[:, 2]

    #Rest of the pulses simulation
    ix = np.searchsorted(t,1/RR)
    y0 = [n_abs+ne_first[ix,i],n_abs+nh_first[ix,i],nt_first[ix,i]]

    soln = []
    soln = odeint(f, y0, t, args=(k,))
    ne[:,i] = soln[:, 0]
    nh[:,i] = soln[:, 1]
    nt[:,i] = soln[:, 2]

    PL_first[:,i] = k*nh_first[:,i]*ne_first[:,i]

    PL_dyn[:,i] = k*nh[:,i]*ne[:,i]
    PL[i] = np.trapz(PL_dyn[:,i],t)*RR

PLQY = PL/Iex
PLQY_norm = PLQY/np.amax(PLQY)
```

A.3 Excitation Cross-Correlation

The excitation cross-correlation experiment simulation were carried out similarly to what already presented above and following the procedure presented in the work by Borgwart et al.[113] We highlight that two separate trains of pulses, indicated for convenience as *pump* and *probe*, are considered. In the presented case we considered a symmetric pump condition, i.e. `P_probe = P_pump`.

```python
# Initial condition for excited state population
P_pump = np.array([2500, 1700, 1000, 700, 500, 100])*1e-6       #
    Avarage CW power (W)
P_probe = P_pump
lamda = 400*1e-9                        # Excitation wavelength (m)
h = 6.67*(10**(-34))                    # Plank Constant (Js)
c = 3*(10**8)                           # Speed of light
Ap = np.pi*(70*10**(-6))**2             # Spot size (m^2)
Iex_pump = P_pump/Ap                    # Excitation intensity (W/m^2)
Iex_probe = P_probe/Ap
OD = 0.27                               # Optical density at the pumping
    wavelength


# Since the penetration depth is round 1um (OD=0,27 @ 400nm for 700nm
    thick sample), we consider the light to be absorbed in the whole
    thickness of the sample

d = 700*1e-9    # Sample thickness (m)

RR = 250*1e3    # Repetition rate (1/s)

Nt = 8e18       # available traps density (cm^-3)
kb = 4e-10      # bimolecular recombination rate
gt = 6e-11      # electron trapping rate (cm^3/s)
gr = 1e-12      # hole rec. with trapped electron rate   (cm^3/s)
gamma = 1e-28   # Auger rec rated   (cm^6/s)

# Fluence (uJ/cm^2)
F_pump = P_pump/(RR*Ap*1e4)*1e6
F_probe = P_probe/(RR*Ap*1e4)*1e6
# Initial excitation density cm^-3
n0_pump = P_pump*(lamda)/(RR*h*c*Ap*d)*10**(-6)
n0_probe = P_probe*(lamda)/(RR*h*c*Ap*d)*10**(-6)

# Density of absorbed photon considering a saturation
nabs_pump = nabs_probe = np.zeros((P_pump.size))

for i in range(0,P_pump.size):
    nabs_pump[i] = n0_pump[i]*(1-10**(-OD))
    nabs_probe[i] = n0_probe[i]*(1-10**(-OD))
```

In the following we define both the time vector and the vector containing the time delay τ between the two pulses with a logarithmic spacing.

```python
# Time grid
```

```
t = np.logspace(-13,-4, 10000)

# Delay vectors
tau_pos = np.logspace(-12,-6, 50)
tmp = np.zeros((2,tau_pos.size))
tmp[0,:] = tau_pos
tau_neg_tmp = np.fliplr(tmp)*(-1)
tau_neg = tau_neg_tmp[0,:]
tau = np.hstack((tau_neg,tau_pos))

# Initialization of 1-pulse PL
PL_pump = np.zeros((t.size, P_pump.size))
PL_probe = np.zeros((t.size, P_pump.size))
ne_pump = ne_pump1 = np.zeros((t.size, P_pump.size))
nh_pump = nh_pump1 = np.zeros((t.size, P_pump.size))
nt_pump = nt_pump1 = np.zeros((t.size, P_pump.size))
ne_probe = ne_probe1 = np.zeros((t.size, P_pump.size))
nh_probe = nh_probe1 = np.zeros((t.size, P_pump.size))
nt_probe = nt_probe1 = np.zeros((t.size, P_pump.size))

SPump = np.zeros((P_pump.size))
SProbe = SPump

# Initialization of 2-pulse PL
t_2 = np.zeros((t.size, tau.size, P_pump.size))
ne_2 = np.zeros((t.size,tau.size, P_pump.size))
nh_2 = np.zeros((t.size,tau.size, P_pump.size))
nt_2 = np.zeros((t.size,tau.size, P_pump.size))
PL_1 = np.zeros((t.size,tau.size, P_pump.size))
PL_2 = np.zeros((t.size,tau.size, P_pump.size))
S1 = np.zeros((tau.size, P_pump.size))
S2 = np.zeros((tau.size, P_pump.size))
Xcorr = np.zeros((tau.size, P_pump.size))
```

Firstly we evaluated the single pulse PL with the same procedure presented above, thus obtaining the time-integrated PL as a function of the laser pumping power as `SPump[i] = np.trapz(PL_pump[:,i],t)` and `SProbe[i] = np.trapz(PL_probe[:,i],t)`.

```
# 1 pulse PL
for i in range(0,P_pump.size):

    k = kb*sat[i]

    # first pulse simulation for the trap states background creation

    # initial condition vector [electron,hole,trap,exc]
```

```
y0_pump1 = [nabs_pump[i],nabs_pump[i],0]
y0_probe1 = [nabs_probe[i],nabs_probe[i],0]


sol_pump1 = []
sol_probe1 = []
sol_pump1 = odeint(f, y0_pump1, t, args=(k,))
sol_probe1 = odeint(f, y0_probe1, t, args=(k,))


ne_pump1[:,i] = sol_pump1[:, 0]
nh_pump1[:,i] = sol_pump1[:, 1]
nt_pump1[:,i] = sol_pump1[:, 2]


ne_probe1[:,i] = sol_probe1[:, 0]
nh_probe1[:,i] = sol_probe1[:, 1]
nt_probe1[:,i] = sol_probe1[:, 2]


# real pulse
ix = np.searchsorted(t,1/RR)
# initial condition vector [electron,hole,trap]
y0_pump = [nabs_pump[i]+ne_pump1[ix,i],...
           nabs_pump[i]+nh_pump1[ix,i],nt_pump[ix,i]]
y0_probe = [nabs_probe[i]+ne_probe1[ix,i],...
            nabs_probe[i]+nh_pump1[ix,i],nt_probe[ix,i]]

print(y0_probe)

sol_pump = []
sol_probe = []
sol_pump = odeint(f, y0_pump, t, args=(k,))
sol_probe = odeint(f, y0_probe, t, args=(k,))


ne_pump[:,i] = sol_pump[:, 0]
nh_pump[:,i] = sol_pump[:, 1]
nt_pump[:,i] = sol_pump[:, 2]


ne_probe[:,i] = sol_probe[:, 0]
nh_probe[:,i] = sol_probe[:, 1]
nt_probe[:,i] = sol_probe[:, 2]


PL_pump[:,i] = k*nh_pump[:,i]*ne_pump[:,i]
PL_probe[:,i] = k*nh_probe[:,i]*ne_probe[:,i]

#1 pulse PL integral
SPump[i] = np.trapz(PL_pump[:,i],t)
SProbe[i] = np.trapz(PL_probe[:,i],t)
```

Afterwards we considered the PL emission in presence of both the *pump* and *probe* pulses. For each pumping power and time delay the time integrated PL will be given by the sum of the PL arising from the first pulse integrated between the time zero and $t = \tau$, plus the PL due to the second pulse building up a photo-excited carrier population over the first-pulse leftover population:

$$I_{PL}^{(2)} = S_1 + S_2 = \int_0^{\tau} I_{PL}^{(pump)}(t)\,dt + \int_{\tau}^{\infty} I_{PL}^{(probe)}(t)\,dt \tag{A.1}$$

where $I_{PL}^{(probe)}$ is evaluated solving the rate equation set with the proper initial condition, given by $n_0^{2^{nd}\,pulse} = n_0 + n^{1^{st}\,pulse}(t = \tau)$. The relative PL variation is then evaluated as:

$$PEC = \frac{I_{PL}^{(2)} - \int_0^{\infty} I_{PL}^{pump}(t)dt - \int_0^{\infty} I_{PL}^{probe}(t)dt}{I_{PL}^{(2)}} \tag{A.2}$$

This value is indicated in the following script as `Xcorr[i,j]`, where `i` runs over the time delays and `j` over the pumping powers.

```
# 2 pulse PL


for j in range(0,P_pump.size):

    k = kb*sat[j]

    for i in range(0,tau.size):

        if tau[i]>=0:  # Pump pulse arrive first PL emission

            ix = np.searchsorted(t,tau[i])
            PL_1[0:ix,i,j] = PL_pump[0:ix,j]
            # The probe pulse pile up on the residual pump pop
            y0_2 = [ne_pump[ix,j]+nabs_probe[j], ...
                    nh_pump[ix,j]+nabs_probe[j], nt_pump[ix,j]]
            sol2_temp = odeint(f, y0_2, t, args=(k,))
            t_2[:,i,j]=t-tau[i]

            ne_2[:,i,j] = sol2_temp[:, 0]
            nh_2[:,i,j] = sol2_temp[:, 1]
            nt_2[:,i,j] = sol2_temp[:, 2]

            PL_2[:,i,j] = k*nh_2[:,i,j]*ne_2[:,i,j]

            # Integral and X_Corr
            S1[i,j] = np.trapz(PL_1[0:ix,i,j],t[0:ix])    # Integral
                of first pulse
```

```python
        S2[i,j] = np.trapz(PL_2[:,i,j],t)              # Integral
            of second pulse
        Xcorr[i,j] = (S1[i,j]+S2[i,j]-SPump[j]-SProbe[j])...
        ((S1[i,j]+S2[i,j]))


    else: # Probe pulse arrive first

        ix = np.searchsorted(t,-tau[i])
        # print(ix)
        PL_1[0:ix,i,j] = PL_probe[0:ix,j]
        # The pump pulse pile up on the residual probe pop
        y0_2 = [ne_probe[ix,j]+nabs_pump[j], ...
                nh_probe[ix,j]+nabs_pump[j], nt_probe[ix,j]]
        sol2_temp = odeint(f, y0_2, t, args=(k,))
        t_2[:,i,j]=t-tau[i]

        ne_2[:,i,j] = sol2_temp[:, 0]
        nh_2[:,i,j] = sol2_temp[:, 1]
        nt_2[:,i,j] = sol2_temp[:, 2]

        PL_2[:,i,j] = k*nh_2[:,i,j]*ne_2[:,i,j]

        # Integral and X_Corr
        S1[i,j] = np.trapz(PL_1[0:ix,i,j],t[0:ix])   # Integral
            of first pulse
        S2[i,j] = np.trapz(PL_2[:,i,j],t);            # Integral
            of second pulse
        Xcorr[i,j] = (S1[i,j]+S2[i,j]-SPump[j]-SProbe[j])...
        ((S1[i,j]+S2[i,j]);)
```

Eventually the experimental data are loaded and a least square differences minimization procedure was used to fit the simulation to the data in order to account for an instrumental prefactor affecting the experimental data.

```python
# Data loading
data = np.loadtxt('filepath', delimiter="\t", skiprows=1)
tau_exp = data[:,0]*10**(-15) # factor 10**(-15) is to go from fs to
    s
Xcorr_exp = np.zeros((tau_exp.size,P_pump.size))
Xcorr_sim_norm = np.zeros((tau.size,P_pump.size))

def func(k, Xcorr_exp, Xcorr_k):
    return (np.abs((Xcorr_k*k) - Xcorr_exp))

for i in range(0,P_pump.size):
    # exp data need to be multiplied by a factor of 10
```

```
Xcorr_exp[:,i] = data[:,i+1]*10
# interpolating the simulated Xcorr over the exp delays
f = interp1d(tau,Xcorr[:,i])
Xcorr_k = f(tau_exp)
k_lsq = opt.leastsq(func, 0.1, args=(Xcorr_exp[:,i], Xcorr_k))

Xcorr_sim_norm[:,i] = Xcorr[:,i]*np.absolute(k_lsq[0])
```

Bibliography

[1] The end of the Oil Age. *The Economist*, 2003.

[2] M. a. Peña and J. L G Fierro. Chemical structures and performance of perovskite oxides. *Chemical Reviews*, 101(7):1981–2017, 2001.

[3] H. Topsøe, A. Arzruni, and G. Bath. XVI.Auszüge. *Zeitschrift für Kristallographie - Crystalline Materials*, 8(1-6):246–320, nov 1884.

[4] Chr. Kn. Møller. Crystal Structure and Photoconductivity of Caesium Plumbohalides. *Nature*, 182(4647):1436, nov 1958.

[5] Dieter Weber. CH3NH3PbX3, a Pb(II)-System with Cubic Perovskite Structure. *Zeitschrift für Naturforschung*, 33b(August 1978):1443–1445, 1978.

[6] David B. Mitzi. *Synthesis, Structure, and Properties of Organic-Inorganic Perovskites and Related Materials*, pages 1–121. John Wiley & Sons, Inc., 2007.

[7] C. R. Kagan. Organic-Inorganic Hybrid Materials as Semiconducting Channels in Thin-Film Field-Effect Transistors. *Science*, 286(5441):945–947, oct 1999.

[8] Konstantinos Chondroudis and David B Mitzi. Electroluminescence from an Organic-Inorganic Perovskite Incorporating a Quaterthiophene Dye within Lead Halide Perovskite Layers. *Chemistry of Materials*, 11(11):3028–3030, nov 1999.

[9] Kojima, A.; Teshima, K; Miyasaka, T.; Shirai, Y. . Under the spotlight: The organic–inorganic hybrid halide perovskite for optoelectronic applications,. *Proceedings 210th ECS Meeting*, 2006.

[10] Akihiro Kojima, Kenjiro Teshima, Yasuo Shirai, and Tsutomu Miyasaka. Organometal halide perovskites as visible-light sensitizers for photovoltaic cells. *Journal of the American Chemical Society*, 131(17):6050–1, May 2009.

[11] Jeong-Hyeok Im, Chang-Ryul Lee, Jin-Wook Lee, Sang-Won Park, and Nam-Gyu Park. 6.5% Efficient Perovskite Quantum-Dot-Sensitized Solar Cell. *Nanoscale*, 3(10):4088, 2011.

[12] Hui-Seon Kim, Chang-Ryul Lee, Jeong-Hyeok Im, Ki-Beom Lee, Thomas Moehl, Arianna Marchioro, Soo-Jin Moon, Robin Humphry-Baker, Jun-Ho Yum, Jacques E Moser, Michael Grätzel, and Nam-Gyu Park. Lead iodide perovskite sensitized all-solid-state submicron thin film mesoscopic solar cell with efficiency exceeding 9%. *Scientific reports*, 2:591, jan 2012.

[13] Lioz Etgar, Peng Gao, Zhaosheng Xue, Qin Peng, Aravind Kumar Chandiran, Bin Liu, Md. K Nazeeruddin, and Michael Grätzel. Mesoscopic CH3NH3PbI3/TiO2 Heterojunction Solar Cells. *Journal of the American Chemical Society*, 134(42):17396–17399, 2012.

[14] Michael M Lee, Joël Teuscher, Tsutomu Miyasaka, Takurou N Murakami, and Henry J Snaith. Efficient hybrid solar cells based on meso-superstructured organometal halide perovskites. *Science (New York, N.Y.)*, 338(6107):643–7, nov 2012.

[15] Qi Chen, Huanping Zhou, Ziruo Hong, Song Luo, Hsin-Sheng Duan, Hsin-Hua Wang, Yongsheng Liu, Gang Li, and Yang Yang. Planar heterojunction perovskite solar cells via vapor assisted solution process. *Journal of the American Chemical Society*, (Scheme 1):3–6, 2013.

[16] Jun-Yuan Jeng, Yi-Fang Chiang, Mu-Huan Lee, Shin-Rung Peng, Tzung-Fang Guo, Peter Chen, and Ten-Chin Wen. CH3NH3PbI3 Perovskite/Fullerene Planar-Heterojunction Hybrid Solar Cells. *Advanced Materials*, 25(27):3727–3732, 2013.

[17] Dianyi Liu and Timothy L. Kelly. Perovskite solar cells with a planar heterojunction structure prepared using room-temperature solution processing techniques. *Nature Photonics*, 8(2):133–138, December 2013.

[18] Chen, Q.; De Marco, N.; Yang, Y.(Michael); Song, T.-B.; Chen, C.-C.; Zhao, H.; Hong, Z.; Zhou, H.; Yang, Y. Under the spotlight: The organic–inorganic hybrid halide perovskite for optoelectronic applications,. *Nano Today*, 10(3):355–396, 2015.

[19] Shuping Pang, Hao Hu, Jiliang Zhang, Siliu Lv, Yaming Yu, Feng Wei, Tianshi Qin, Hongxia Xu, Zhihong Liu, and Guanglei Cui. NH2CH=NH2PbI3: An alternative organolead iodide perovskite sensitizer for mesoscopic solar cells. *Chemistry of Materials*, 26(3):1485–1491, 2014.

[20] Giles E. Eperon, Samuel D. Stranks, Christopher Menelaou, Michael B. Johnston, Laura M. Herz, and Henry J. Snaith. Formamidinium lead trihalide: a broadly tunable perovskite for efficient planar heterojunction solar cells. *Energy & Environmental Science*, 7(3):982, 2014.

[21] Jin-Wook Lee, Dong-Jin Seol, An-Na Cho, and Nam-Gyu Park. High-Efficiency Perovskite Solar Cells Based on the Black Polymorph of HC(NH2)2PbI3. *Advanced Materials*, 26(29):4991–4998, 2014.

[22] Nakita K. Noel, Samuel D. Stranks, Antonio Abate, Christian Wehrenfennig, Simone Guarnera, Amir Haghighirad, Aditya Sadhanala, Giles E Eperon, Sandeep K. Pathak, Michael B Johnston, Annamaria Petrozza, Laura Herz, and Henry Snaith. Lead-Free Organic-Inorganic Tin Halide Perovskites for Photovoltaic Applications. *Energy & Environmental Science*, 7:3061–3068, 2014.

[23] Feng Hao, Constantinos C. Stoumpos, Duyen Hanh Cao, Robert P. H. Chang, and Mercouri G. Kanatzidis. Lead-free solid-state organic–inorganic halide perovskite solar cells. *Nature Photonics*, 8(6):489–494, may 2014.

[24] V. M. Goldschmidt. Krystallbau und chemische zusammensetzung. *Berichte der deutschen chemischen Gesellschaft (A and B Series)*, 60(5):1263–1296, 1927.

[25] Chonghea Li, Xionggang Lu, Weizhong Ding, Liming Feng, Yonghui Gao, and Ziming Guo. Formability of ABX_3 (X = F, Cl, Br, I) halide perovskites. *Acta Crystallographica Section B Structural Science*, 64(6):702–707, 2008.

[26] Green, M.; Ho-Baillie, A.; Snaith, H.J. The emergence of perovskite solar cells. *Nature Photonics*, 8(7):506–514, 2014.

[27] Tom Baikie, Yanan Fang, Jeannette M. Kadro, Martin Schreyer, Fengxia Wei, Subodh G. Mhaisalkar, Michael Graetzel, and Tim J. White. Synthesis and crystal chemistry of the hybrid perovskite (CH3NH3)PbI3 for solid-state sensitised solar cell applications. *Journal of Materials Chemistry A*, 1(18):5628, 2013.

[28] Constantinos C Stoumpos, Christos D Malliakas, and Mercouri G Kanatzidis. Semiconducting Tin and Lead Iodide Perovskites with Organic Cations: Phase Transitions, High Mobilities, and Near-Infrared Photoluminescent Properties. *Inorganic Chemistry*, 52(15):9019–9038, aug 2013.

[29] Kelsey K. Bass, R. Eric McAnally, Shiliang Zhou, Peter I. Djurovich, Mark E. Thompson, and Brent C. Melot. Influence of moisture on the preparation, crystal structure, and photophysical properties of organohalide perovskites. *Chem. Commun.*, 50(99):15819–15822, 2014.

[30] Giles E Eperon, Severin N Habisreutinger, Tomas Leijtens, Bardo J Bruijnaers, Jacobus J. van Franeker, Dane W. DeQuilettes, Sandeep Pathak, Rebecca J. Sutton, Giulia Grancini, David S. Ginger, Rene a J Janssen, Annamaria Petrozza, and Henry J Snaith. The Importance of Moisture in Hybrid Lead Halide Perovskite Thin Film Fabrication. *ACS Nano*, 9(9):9380–9393, sep 2015.

[31] Giulia Grancini, Valerio D'Innocenzo, Emma R. Dohner, Nicola Martino, Ajay Ram Srimath Kandada, Edoardo Mosconi, Filippo De Angelis, Hemamala I Karunadasa, Eric T Hoke, and annamaria Petrozza. CH3NH3PbI3 Perovskite Single Crystals: Surface Photophysics and its Interaction with the Environment. *Chem. Sci.*, 00:1–6, 2015.

[32] Stranks, S.; Snaith, H.J. Metal-halide perovskites for photovoltaic and light-emitting devices. *Nature Nanotechnology*, 10(5):391–402, 2015.

[33] Tomas Leijtens, Giles E. Eperon, Nakita K. Noel, Severin N. Habisreutinger, Annamaria Petrozza, and Henry J. Snaith. Stability of Metal Halide Perovskite Solar Cells. *Advanced Energy Materials*, 2015.

[34] Hao Gao, Chunxiong Bao, Faming Li, Tao Yu, Jie Yang, Weidong Zhu, Xiaoxin Zhou, Gao Fu, and Zhigang Zou. Nucleation and Crystal Growth of Organic–Inorganic Lead Halide Perovskites under Different Relative Humidity. *ACS Applied Materials & Interfaces*, 7(17):9110–9117, 2015.

[35] Samuel D. Stranks, Pabitra K. Nayak, Wei Zhang, Thomas Stergiopoulos, and Henry J. Snaith. Formation of Thin Films of Organic-Inorganic Perovskites for High-Efficiency Solar Cells. *Angewandte Chemie International Edition*, 2015.

[36] Samuel D Stranks, Giles E Eperon, Giulia Grancini, Christopher Menelaou, Marcelo J P Alcocer, Tomas Leijtens, Laura M Herz, Annamaria Petrozza, and Henry J Snaith. Electron-hole diffusion lengths exceeding 1 micrometer in an organometal trihalide perovskite absorber. *Science (New York, N.Y.)*, 342(6156):341–4, 2013.

[37] Guichuan Xing, Nripan Mathews, Shuangyong Sun, Swee Sien Lim, Yeng Ming Lam, Michael Grätzel, Subodh Mhaisalkar, and Tze Chien Sum. Long-range balanced electron- and hole-transport lengths in organic-inorganic CH3NH3PbI3. *Science (New York, N.Y.)*, 342(6156):344–7, 2013.

[38] Pablo Docampo, Fabian Hanusch, Samuel D. Stranks, Markus Döblinger, Johann M. Feckl, Martin Ehrensperger, Norma K. Minar, Michael B. Johnston, Henry J. Snaith, and Thomas Bein. Solution Deposition-Conversion for Planar Heterojunction Mixed Halide Perovskite Solar Cells. *Advanced Energy Materials*, 4(14):1–6, may 2014.

[39] Giulia Grancini, Sergio Marras, Mirko Prato, Cinzia Giannini, Claudio Quarti, Filippo De Angelis, Michele De Bastiani, Giles E. Eperon, Henry J. Snaith, Liberato Manna, and Annamaria Petrozza. The Impact of the Crystallization Processes on the Structural and Optical Properties of Hybrid Perovskite Films for Photovoltaics. *The Journal of Physical Chemistry Letters*, 5(21):140926103112004, sep 2014.

[40] Quinten a. Akkerman, Valerio D'Innocenzo, Sara Accornero, Alice Scarpellini, Annamaria Petrozza, Mirko Prato, and Liberato Manna. Tuning the Optical Properties of Cesium Lead Halide Perovskite Nanocrystals by Anion Exchange Reactions. *Journal of the American Chemical Society*, 137(32):10276–10281, 2015.

[41] Norman Pellet, Joël Teuscher, Joachim Maier, and Michael Grätzel. Transforming Hybrid Organic Inorganic Perovskites by Rapid Halide Exchange. *Chemistry of Materials*, page 150303133239003, 2015.

[42] Edoardo Mosconi, Anna Amat, Md. K. Nazeeruddin, Michael Grätzel, and Filippo De Angelis. First-Principles Modeling of Mixed Halide Organometal Perovskites for Photovoltaic Applications. *The Journal of Physical Chemistry C*, 117(27):13902–13913, jul 2013.

[43] Jun Hong Noh, Sang Hyuk Im, Jin Hyuck Heo, Tarak N Mandal, and Sang Il Seok. Chemical management for colorful, efficient, and stable inorganic-organic hybrid nanostructured solar cells. *Nano letters*, 13(4):1764–9, apr 2013.

[44] Dong Shi, Valerio Adinolfi, Riccardo Comin, Mingjian Yuan, Erkki Alarousu, Andrei Buin, Yin Chen, Sjoerd Hoogland, Alexander Rothenberger, Khabiboulakh Katsiev, Yaroslav Losovyj, Xin Zhang, Peter A Dowben, Omar F Mohammed, Edward H Sargent, and Osman M Bakr. Low trap-state density and long carrier diffusion in organolead trihalide perovskite single crystals. *Science*, 347:519–522, 2015.

[45] Haiming Zhu, Yongping Fu, Fei Meng, Xiaoxi Wu, Zizhou Gong, Qi Ding, Martin V. Gustafsson, M. Tuan Trinh, Song Jin, and X-Y. Zhu. Lead halide perovskite nanowire lasers with low lasing thresholds and high quality factors. *Nature Materials*, (April):1–8, 2015.

[46] Guichuan Xing, Nripan Mathews, Swee Sien Lim, Natalia Yantara, Xinfeng Liu, Dharani Sabba, Michael Grätzel, Subodh Mhaisalkar, and Tze Chien Sum. Low-temperature solution-processed wavelength-tunable perovskites for lasing. *Nature materials*, 13(5):476–80, may 2014.

[47] Zhi-Kuang Tan, Reza Saberi Moghaddam, May Ling Lai, Pablo Docampo, Ruben Higler, Felix Deschler, Michael Price, Aditya Sadhanala, Luis M. Pazos, Dan Credgington, Fabian Hanusch, Thomas Bein, Henry J. Snaith, and Richard H. Friend. Bright light-emitting diodes based on organometal halide perovskite. *Nature Nanotechnology*, (August):1–6, aug 2014.

[48] Umari, P.; Mosconi, E. and De Angelis, F. Relativistic gw calculations on ch3nh3pbi3 and ch3nh3sni3 perovskite for solar cells applications,. *Scientific Report*, 4:4467, 2014.

[49] Even, J.; Pedesseau, L.; Jancu, J.-M.; Katan, C. Importance of spin–orbit coupling in hybrid organic/inorganic perovskites for photovoltaic applications,. *The Journal of Physical Chemistry Letters*, 4(17):2999–3005, 2013.

[50] Brivio, F.; Walker, A.B.; Walsh, A. Structural and electronic properties of hybrid perovskites for high-efficiency thin-film photovoltaics from first-principles,. *APL Materials*, 1(4):042111, 2013.

[51] Frost, J.M.; Butler, K.T.; Brivio, F.; Hendon, C.H.; van Schilfgaarde, M.; Walsh, A. Atomistic origins of high-performance in hybrid halide perovskite solar cells,. *Nano Letters*, 14(5):2584–90, 2013.

[52] Manser, Joseph S. and Kamat, Prashant V. Band filling with free charge carriers in organometal halide perovskites. *Nature Photonics*, 8(9):737–743, 2014.

[53] Neil W. Ashcroft and N. David Mermin. *Solid State Physics.* Holt, Rinehart and Winston, 1976.

[54] Filip, M.R.; Eperon, G.E.; Snaith, H.J.; Giustino, F. Steric engineering of metal-halide perovskites with tunable optical band gaps,. *Nature communications*, 5:5757, 2014.

[55] Amat, A.; Mosconi, E.; Ronca, E.; Quarti, C.; Umari, P.; Nazeeruddin, Md K. Grätzel, M.; De Angelis, F. Cation-induced band-gap tuning in organohalide perovskites: Interplay of spin-orbit coupling and octahedra tilting,. *Nano Letters*, 14:3608–3616, 2014.

[56] Orazio Svelto. *Principles of Lasers.* Springer Science & Business Media, 2010.

[57] Giulia Grancini, Ajay Ram Srimath Kandada, Jarvist M. Frost, Alex J. Barker, Michele De Bastiani, Marina Gandini, Sergio Marras, Guglielmo Lanzani, Aron Walsh, and Annamaria Petrozza. Role of microstructure in the electron–hole interaction of hybrid lead halide perovskites. *Nature Photonics*, 2015.

[58] Kenichiro Tanaka, Takayuki Takahashi, Takuma Ban, Takashi Kondo, Kazuhito Uchida, and Noboru Miura. Comparative study on the excitons in lead-halide-based perovskite-type crystals CH3NH3PbBr3 CH3NH3PbI3. *Solid State Communications*, 127(9-10):619–623, September 2003.

[59] Jacky Even, Laurent Pedesseau, and Claudine Katan. Analysis of Multivalley and Multibandgap Absorption and Enhancement of Free Carriers Related to Exciton Screening in Hybrid Perovskites. *The Journal of Physical Chemistry C*, 118(22):11566–11572, June 2014.

[60] Valerio D'Innocenzo, Giulia Grancini, Marcelo J. P. Alcocer, Ajay Ram Srimath Kandada, Samuel D. Stranks, Michael M. Lee, Guglielmo Lanzani, Henry J. Snaith, and Annamaria Petrozza. Excitons versus free charges in organo-lead tri-halide perovskites. *Nature communications*, 5:3586, January 2014.

[61] Heinz Kalt and Michael Hetterich. *Optics of Semiconductors and Their Nanostructures*, volume 5. Springer Science & Business Media, 2004.

[62] Hartmut Haug and Stephan W. Koch. *Quantum Theory of the Optical and Electronic Properties of Semiconductors.* World Scientific, 2004.

[63] Guglielmo Lanzani. *The Photophysics behind Photovoltaics and Photonics.* Wiley, 2012.

[64] R.J. Elliott. Intensity of optical absorption by excitons. *Physical Review*, 108(6):1384–1389, 1957.

[65] Michele Saba, Michele Cadelano, Daniela Marongiu, Feipeng Chen, Valerio Sarritzu, Nicola Sestu, Cristiana Figus, Mauro Aresti, Roberto Piras, Alessandra Geddo Lehmann, Carla Cannas, Anna Musinu, Francesco Quochi, Andrea Mura, and Giovanni Bongiovanni. Correlated electron-hole plasma in organometal perovskites. *Nature communications*, 5(May):5049, January 2014.

[66] Yasuhiro Yamada, Toru Nakamura, Masaru Endo, Atsushi Wakamiya, and Yoshihiko Kanemitsu. Photocarrier recombination dynamics in perovskite CH3NH3PbI3 for solar cell applications. *Journal of the American Chemical Society*, 136(33):11610–3, August 2014.

[67] Anthony Mark Fox. *Optical Properties of Solids.* Oxford University Press, 2001.

[68] Jenny Nelson. *The Physics of Solar Cells.* Imperial College Press, 2003.

[69] Franz Urbach. The long-wavelength edge of photographic sensitivity and of the electronic Absorption of Solids [8]. *Physical Review*, 92(5):1324, 1953.

[70] Piet Van Mieghem. Theory of band tails in heavily doped semiconductors. *Reviews of Modern Physics*, 64(3):755–793, July 1992.

[71] Lihua Bai, Chunchuan Xu, P G Schunemann, K Nagashio, R S Feigelson, and N C Giles. Urbach rule used to explain the variation of the absorption edge in CdGeAs 2 crystals. *Journal of Physics: Condensed Matter*, 17(3):549–558, January 2005.

[72] Y.P. Varshni. Temperature dependence of the energy gap in semiconductors. *Physica*, 34(1):149–154, January 1967.

[73] a. Olkhovets, R.-C. Hsu, A. Lipovskii, and F. Wise. Size-Dependent Temperature Variation of the Energy Gap in Lead-Salt Quantum Dots. *Physical Review Letters*, 81(16):3539–3542, October 1998.

[74] Claudio Quarti, Edoardo Mosconi, James Michael Ball, Valerio D'Innocenzo, Chen Tao, Sandeep Pathak, Henry J. Snaith, Annamaria Petrozza, and Filippo De Angelis. Structural and optical properties of methylammonium lead iodide across the tetragonal to cubic phase transition: implications for perovskite solar cells. *Energy Environ. Sci.*, pages 2–8, 2015.

[75] Ivan Pelant and Jan Valenta. *Luminescence Spectroscopy of Semiconductors*. OUP Oxford, 2012.

[76] D. a B Miller, D. S. Chemla, D. J. Eilenberger, P. W. Smith, a. C. Gossard, and W. T. Tsang. Large room-temperature optical nonlinearity in GaAs/Ga1-x AlxAs multiple quantum well structures. *Applied Physics Letters*, 41(8):679–681, 1982.

[77] H.B. Bebb and E.H. Williams. *Semiconductors and Semimetals*, volume 8. Accademic Press, Boston, 1972.

[78] Annamraju Viswanath, Joo Lee, Dongho Kim, C. Lee, and J. Leem. Exciton-phonon interactions, exciton binding energy, and their importance in the realization of room-temperature semiconductor lasers based on GaN. *Physical Review B*, 58(24):16333–16339, 1998.

[79] R. Cingolani, L. Calcagnile, G. Colí, R. Rinaldi, M. Lomoscolo, M. DiDio, A. Franciosi, L. Vanzetti, G. C. LaRocca, and D. Campi. Radiative recombination processes in wide-band-gap II–VI quantum wells: the interplay between excitons and free carriers. *Journal of the Optical Society of America B*, 13(6):1268, June 1996.

[80] M. N. Saha. On a Physical Theory of Stellar Spectra. *Proceedings of the Royal Society A: Mathematical, Physical and Engineering Sciences*, 99(697):135–153, May 1921.

[81] Roberto Piazza. *Note di fisica statistica*. Springer, 2011.

[82] Michele De Bastiani, Valerio D'Innocenzo, Samuel D. Stranks, Henry J. Snaith, and Annamaria Petrozza. Role of the crystallization substrate on the photoluminescence properties of organo- lead mixed halides perovskites Role of the crystallization substrate on the photoluminescence properties of organo-lead mixed halides perovskites. *APL Materials*, 2(8):081509, August 2014.

[83] Valerio D'Innocenzo, Ajay Ram Srimath Kandada, Michele De Bastiani, Marina Gandini, and Annamaria Petrozza. Tuning the light emission properties by band gap engineering in hybrid lead-halide perovskite. *Journal of the American Chemical Society*, pages 1–4, 2014.

[84] Jeong-Hyeok Im, In-Hyuk Jang, Norman Pellet, Michael Grätzel, and Nam-Gyu Park. Growth of CH3NH3PbI3 cuboids with controlled size for high-efficiency perovskite solar cells. *Nature nanotechnology*, (August):1–6, August 2014.

[85] Qianqian Lin, Ardalan Armin, Ravi Chandra, Raju Nagiri, Paul L Burn, and Paul Meredith. Electro-optics of perovskite solar cells. *Nature Photonics*, (December), 2014.

[86] M. Hirasawa, T. Ishihara, T. Goto, K. Uchida, and N. Miura. Magnetoabsorption of the lowest exciton in perovskite-type compound (CH3NH3)PbI3. *Physica B: Condensed Matter*, 201:427–430, jul 1994.

[87] Atsuhiko Miyata, Anatolie Mitioglu, Paulina Plochocka, Oliver Portugall, Jacob Tse-Wei Wang, Samuel D. Stranks, Henry J. Snaith, and Robin J. Nicholas. Direct measurement of the exciton binding energy and effective masses for charge carriers in organic-inorganic tri-halide perovskites. *Nature Physics*, 11(7):582–587, 2015.

[88] Julian Burschka, Norman Pellet, Soo-Jin Moon, Robin Humphry-Baker, Peng Gao, Mohammad K Nazeeruddin, and Michael Grätzel. Sequential deposition as a route to high-performance perovskite-sensitized solar cells. *Nature*, 499(7458):316–9, July 2013.

[89] Dongqin Bi, Soo-Jin Moon, Leif Häggman, Gerrit Boschloo, Lei Yang, Erik M. J. Johansson, Mohammad K. Nazeeruddin, Michael Grätzel, and Anders Hagfeldt. Using a two-step deposition technique to prepare perovskite (CH3NH3PbI3) for thin film solar cells based on ZrO2 and TiO2 mesostructures. *RSC Advances*, 3(41):18762, 2013.

[90] Jeremy L Knutson, James D Martin, and David B Mitzi. Tuning the band gap in hybrid tin iodide perovskite semiconductors using structural templating. *Inorganic chemistry*, 44(13):4699–705, June 2005.

[91] Claudio Quarti, Giulia Grancini, Edoardo Mosconi, Paola Bruno, James M Ball, Michael M Lee, Henry J Snaith, Annamaria Petrozza, and Filippo De Angelis. The Raman Spectrum of the CH3NH3PbI3 Hybrid Perovskite: Interplay of Theory and Experiment. *The Journal of Physical Chemistry Letters*, 5(2):279–284, jan 2014.

[92] Peng Qin, Soichiro Tanaka, Seigo Ito, Nicolas Tetreault, Kyohei Manabe, Hitoshi Nishino, Mohammad Khaja Nazeeruddin, and Michael Grätzel. Inorganic hole conductor-based lead halide perovskite solar cells with 12.4% conversion efficiency. *Nature Communications*, 5(May):1–6, May 2014.

[93] Qi Chen, Huanping Zhou, Ziruo Hong, Song Luo, Hsin-Sheng Duan, Hsin-Hua Wang, Yongsheng Liu, Gang Li, and Yang Yang. Planar heterojunction perovskite solar cells via vapor-assisted solution process. *Journal of the American Chemical Society*, 136(2):622–5, January 2014.

[94] Samuel D. Stranks, Victor M. Burlakov, Tomas Leijtens, James M. Ball, Alain Goriely, and Henry J. Snaith. Recombination Kinetics in Organic-Inorganic Perovskites: Excitons, Free Charge, and Subgap States. *Physical Review Applied*, 2(3):034007, September 2014.

[95] C. Jordan, J. F. Donegan, J. Hegarty, B. J. Roycroft, S. Taniguchi, T. Hino, E. Kato, N. Noguchi, and a. Ishibashi. Carrier-density dependence of the photoluminescence lifetimes in ZnCdSe/ZnSSe quantum wells at room temperature. *Applied Physics Letters*, 74(22):3359, 1999.

[96] Hideki Yasuda and Yoshihiko Kanemitsu. Dynamics of nonlinear blue photoluminescence and Auger recombination in $SrTiO_3$. *Physical Review B*, 77(19):193202, 2008.

[97] Yasuhiro Yamada, Hideki Yasuda, Takeshi Tayagaki, and Yoshihiko Kanemitsu. Temperature dependence of photoluminescence spectra of nondoped and electron-doped $SrTiO_3$: crossover from auger recombination to single-carrier trapping. *Physical review letters*, 102(24):247401, 2009.

[98] Alessio Filippetti, Pietro Delugas, and Alessandro Mattoni. Methylammonium Lead-Iodide Perovskite: Recombination and Photoconversion of an Inorganic Semiconductor Within a Hybrid Body. *The Journal of Physical Chemistry C*, 118(43):24843–24853, October 2014.

[99] S Stagira, M Nisoli, G Cerullo, M. Zavelani–Rossi, S. De Silvestri, G. Lanzani, W. Graupner, and G. Leising. The role of amplified spontaneous emission in the ultrafast relaxation dynamics of polymer films. *Chemical Physics Letters*, 289(1-2):205–210, jun 1998.

[100] Michael McGehee, Rahul Gupta, Siegfried Veenstra, E. Miller, María Díaz-García, and Alan Heeger. Amplified spontaneous emission from photopumped films of a conjugated polymer. *Physical Review B*, 58(11):7035–7039, sep 1998.

[101] Yuxi Tian and Ivan G. Scheblykin. Artifacts in Absorption Measurements of Organometal Halide Perovskite Materials: What Are the Real Spectra? *The Journal of Physical Chemistry Letters*, 6(17):3466–3470, 2015.

[102] Marina R Filip, Carla Verdi, and Feliciano Giustino. GW Band Structures and Carrier Effective Masses of CH3NH3PbI3 and Hypothetical Perovskites of the Type APbI 3 : A = NH 4 , PH 4 , AsH 4 and SbH 4. *The Journal of Physical Chemistry C*, page 151019090846007, 2015.

[103] Eric T Hoke, Daniel J Slotcavage, Emma R Dohner, Andrea R Bowring, Hemamala I Karunadasa, and Michael D McGehee. Reversible photo-induced trap formation in mixed-halide hybrid perovskites for photovoltaics. *Chemical Science*, 6(1):613–617, 2015.

[104] Tomas Leijtens, Giulia Grancini, Giles E. Eperon, James M. Ball, Michele De Bastianni, Konrad Wojciechowski, Nicola Martino, Henry J. Snaith, and Annamaria Petrozza. Mapping Electric Field – Induced Switchable Polarization and Structural Degradation in Hybrid Lead Halide Perovskite Thin Films. *Submitted for Publication*, pages 1–11, 2015.

[105] D. Von der Linde, J. Kuhl, and E. Rosengart. Picosecond Correlation Effects in the hot luminescence of GaAs. *Journal of Luminescence*, 24/25:675–678, 1981.

[106] M. B. Johnson, T. C. McGill, and a. T. Hunter. Picosecond time-resolved photoluminescence using picosecond excitation correlation spectroscopy. *Journal of Applied Physics*, 63(6):2077–2082, 1988.

[107] M. Jørgensen. Time-resolved nonlinear luminescence spectroscopy by picosecond excitation correlation. *Applied Physics Letters*, 43(5):460, 1983.

[108] Rajesh Kumar and A. Vengurlekar. Nonlinear picosecond excitation-correlation luminescence due to free electron-hole pairs in GaAs, 1996.

[109] Michele De Bastiani, Giorgio Dell'Erba, Marina Gandini, Valerio D'Innocenzo, Stefanie Neutzner, Ajay Ram Srimath Kandada, Giulia Grancini, Maddalena Binda, Mirko Prato, James M. Ball, Mario Caironi, and Annamaria Petrozza. Ion Migration and the Role of Preconditioning Cycles in the Stabilization of the J - V Characteristics of Inverted Hybrid Perovskite Solar Cells. *Advanced Energy Materials*, 6(2), jan 2016.

[110] Artem a. Bakulin, Oleg Selig, Huib J. Bakker, Yves L.a. Rezus, Christian Müller, Tobias Glaser, Robert Lovrincic, Zhenhua Sun, Zhuoying Chen, Aron Walsh, Jarvist M. Frost, and Thomas L. C. Jansen. Real-Time Observation of Organic Cation Reorientation in Methylammonium Lead Iodide Perovskites. *The Journal of Physical Chemistry Letters*, pages 3663–3669, 2015.

[111] R D Schaller, M a Petruska, and V I Klimov. Tunable near-infrared optical gain and amplified spontaneous emission using PbSe nanocrystals. *Journal Of Physical Chemistry B*, 107(50):13765–13768, 2003.

[112] Sergei A Ivanov, Jagjit Nanda, Andrei Piryatinski, Marc Achermann, Laurent P Balet, Ilia V Bezel, Polina O Anikeeva, Sergei Tretiak, and Victor I Klimov. Light Amplification Using Inverted Core/Shell Nanocrystals: Towards Lasing in the Single-Exciton Regime. *The Journal of Physical Chemistry B*, 108(30):10625–10630, jul 2004.

[113] M. Borgwardt, P. Sippel, R. Eichberger, M. P. Semtsiv, W. T. Masselink, and K. Schwarzburg. Excitation correlation photoluminescence in the presence of Shockley-Read-Hall recombination. *Journal of Applied Physics*, 117(21):215702, 2015.

List of publications

2015a M. De Bastiani, G. Dell'Erba, M. Gandini, <u>V. D'Innocenzo</u>, S. Neutzner, A. R. Srimath Kandada, G. Grancini, M. Binda, M. Prato, J.M. Ball, M. Caironi, A. Petrozza*
"Ion Migration and the Role of Preconditioning Cycles in the Stabilization of the J−V Characteristics of Inverted Hybrid Perovskite Solar Cells",
Advanced Energy Materials, doi:10.1002/aenm.201501453

2015b Q.A. Akkerman, <u>V. D'Innocenzo</u>, S. Accornero, A. Scarpellini, A. Petrozza, M. Prato, L. Manna*
"Tuning the Optical Properties of Cesium Lead Halide Perovskite Nanocrystals by Anion Exchange Reactions",
Journal of the American Chemical Society,*137(32)10276*

2015c C. Quarti, E. Mosconi, J.M. Ball, <u>V. D'Innocenzo</u>, C. Tao, S. Pathak, H.J. Snaith, A. Petrozza, F. De Angelis**
"Structural and optical properties of methylammonium lead iodide across the tetragonal to cubic phase transition: implications for perovskite solar cells"
Energy & Environmental Science, doi: 10.1039/c5ee02925b

2015d G. Grancini*, <u>V. D'Innocenzo</u>, E.R. Dohner, N. Martino, A.R. Srimath Kandada, E. Mosconi, F. De Angelis, H.I. Karunadasa, E.T. Hoke, A. Petrozza*
"$CH_3NH_3PbI_3$ perovskite single crystals: surface photophysics and their interaction with the environment",
Chemical Science, doi: 10.1039/c5sc02542g

2014a <u>V. D'Innocenzo</u>, A.R. Srimath Kandada, M. De Bastiani, M. Gandini, A. Petrozza*
"Tuning the light emission properties by band gap engineering in hybrid lead-halide perovskite",
Journal of the American Chemical Society,*136(51)17730*

2014b <u>V. D'Innocenzo</u>, A. Luzio, A. Petrozza, D. Fazzi, M. Caironi*
"Nature of Charge Carriers in a High Electron Mobility Naphthalenediimide Based Semiconducting Copolymer",
Advanced Functional Materials, 24(35) *5584-5593*

2014c M. De Bastiani, <u>V. D'Innocenzo</u>, S.D. Stranks, H.J. Snaith, A. Petrozza*
"Role of the crystallization substrate on the photoluminescence properties of organo-lead mixed halides perovskites",
APL Materials, 2(8)*081509*

2014d <u>V. D'Innocenzo</u> G. Grancini, M.J.P. Alcocer, A.R. Srimath Kandada, S.D. Stranks, M.M. Lee, G. Lanzani, H.J. Snaith, A. Petrozza*
"Excitons versus free charges in organo-lead tri-halide perovskites",
Nature Communications,5

2013 A. Luzio, L. Criante, <u>V. D'Innocenzo</u>, M. Caironi*
"Control of charge transport in a semiconducting copolymer by solvent-induced long-range order",
Scintific Reports,3, *1–6*

2012 E.V. Canesi, M. Binda, A. Abate, S. Guarnera, L. Moretti, <u>V. D'Innocenzo</u>, R.S. Santosh Kumar, C. Bertarelli, A. Abrusci, H.J. Snaith, A. Calloni, A. Brambilla, F. Ciccacci, S. Aghion, F. Moia, R. Ferragut, C. Melis, G. Malloci, A. Mattoni, G. Lanzani, A. Petrozza*
"The effect of selective interactions at the interface of polymeroxide hybrid solar cells",
Energy & Environmental Science, 5(10), *9068–9076*

2010 M.D. Brown, T. Suteewong, R.S. Santosh Kumar, <u>V. D'Innocenzo</u>, A. Petrozza, M.M. Lee, U. Wiesner, H.J. Snaith*
"Plasmonic dye-sensitized solar cells using core shell metal insulator nanoparticles",
Nano letters, 11(2), *438–445*

ACKNOWLEDGMENTS

"I F I have seen further, it is by standing on the shoulders of giants". Despite the fact that citing Newton in a thesis acknowledgments may sound quite nerdy, I can't help thinking that there's nothing more appropriate than these words. On the one hand this obviously refers to the huge amount of science on which we are adding such a thin brick to the building of knowledge, on the other hand I intended to refer to the team-effort that is somehow one of the giants on which this thesis is standing.

First and foremost I want to thank Annamaria for being the Virgil that guided my wondering in the word of science and Guglielmo for making my research possible at the CNST. Cosimo, Giulia, Ilaria and Marcelo, you have been my colleagues and mentors furnishing me all the instruments to play around in the lab. Hoping I drew something worth out of it, thank you. I want to thank Ajay for his patience and constant help. I have to admit that without his accuracy and experience almost every measurements I did during my PhD would have ended up into a drawer with no use. Thanks for seeing the science nested into my work. I want also to thank Mario for our squash based molecular electronics meetings (I'll miss them). I'm grateful to all the PhD students (plus Ale L who's not one but he likes to pretend to be...) I worked with. The knowledge sharing and kitchen-based brainstorming gave a fundamental contribution to my scientific and personal growth. Thanks. A special mention goes to my travel companions Michele DB and Marina. Not only you are competent scientists, you also made it all a lot of fun. Thank you for that.

I'm thankful beyond what I can express through words to my family and friends. During these three years some of you passed away, it is especially to you that I offer my heartfelt thanks. I thank my parents and my sisters for supporting my choice of enrolling into a PhD course and for their constant effort of keep listening me when I talked about my research without falling asleep. I want to thank RL if only to have proven seamlessly to be my brother, the one left.

Eventually I thank SC for her patience and love. I won't even try to say more than that, here words are no use.